Dissertation
submitted to the
Combined Faculties for the Natural Sciences and for Mathematics
of the Rupertus Carola University of
Heidelberg, Germany
for the degree of
Doctor of Natural Sciences

presented by

M.S. Physicist: Amara Lynn Graps
born in: Honolulu, Hawaii, U.S.A.

Oral Examination: 18th July 2001

Io Revealed
in the
Jovian Dust Streams

Referees: Prof. Dr. Eberhard Grün

Prof. Dr. Dietrich Lemke

The dust wakes out of its slumber and I follow its passage.

From volcanoes on moons, through comet breezes,
Atop bookshelves in rooms, expelled by human sneezes,
From disks of new stars into emerald-blue planets,
The dust is a piece of me, or am I a piece of dust?

We fly from the ecliptic brightness, feel comforted by the local fluff, and drink a ceylon tea at the cosmic tea table with our friends from β Pic. They don't laugh at my jokes, but I smile anyway.

Amara Lynn Graps

Abstract

Io Revealed in the Jovian Dust Streams

The Jovian dust streams are high-rate bursts of submicron-sized particles traveling in the same direction from a source in the Jovian system. Since their discovery in 1992, the Jovian dust streams have been observed by three spacecraft: Ulysses, Galileo and Cassini. The work presented here describes an emerging electrodynamical picture of the Jovian dust streams as they appear inside and outside of the Jupiter environment. The source of the Jovian dust streams is Jupiter's moon, Io, in particular, dust from Io's volcanoes. Charged Io dust, traveling on trajectories from Io's location, is shown to have some particular signatures in real space and in frequency space.

The Jovian dust stream dynamics in the frequency-transformed Galileo spacecraft dust measurements show different signatures, varying, orbit-to-orbit during Galileo's last 29 orbits around Jupiter. The varying frequencies from orbit-to-orbit are dependent on the spacecraft and dust detector geometry, on the local plasma conditions, and on Io itself, most likely its volcanoes' activity. The presence of Io's orbital rotational frequency demonstrates that Io is a localized source of charged dust particles and a confirmation of Io's role as a localized charged dust source arises through the modulation effects. This time-frequency analysis is the first direct evidence that Io is the source of the Jovian dust streams. I provide additional frequency evidence of Io recorded by Cassini and Galileo during an August 2000 Jovian dust streams 'storm'.

Several aspects of the dust stream particles' dynamics in real space can be understood if the particle's charge is varying, via the different currents generated as the dust particle samples the plasma while traveling. One application I show is matching the travel time of a stream particle during the December 2000 joint Galileo-Cassini dust stream measurements, where the two spacecraft were located inside (Galileo) and outside (Cassini) of the Jovian magnetosphere. To match these measurements, the smallest dust particles could have the following range of parameters: radius: 6 nanometers, density: 1.35–1.75 g/cm^3, initial charge potential: 1–4 V, secondary electron emission yield: 3.0, dependent on a maximum electron energy 300 eV, and a photoelectron emission yield: 0.1–1.0, which produce dust particle speeds: 220\450 km s^{-1}(Galileo\Cassini) and charge potentials: 5.5\6.3 V (Galileo\Cassini).

Zusammenfassung

Ios "Fußabdruck" in den Staubströmen des Jupiter

Die Staubströme des Jupiter bestehen aus kollimierten Staubteilchen, die von einer Quelle im Jupitersystem ausgehen. Seit ihrer Entdeckung im Jahr 1992 wurden sie mit Staub-Instrumenten auf den drei Raumsonden Ulysses, Galileo und Cassini untersucht. Die vorgelegte Arbeit beschreibt ein elektrodynamisches Bild der Staubströme wie sie sich innerhalb und außerhalb der Jupiterumgebung zeigen. Die Quelle der Stromteilchen sind die Vulkane auf Jupiters Mond Io. Es wird gezeigt, daß elektrisch geladener Staub von Io, der sich auf bestimmten Bahnen fortbewegt, charakteristische Eigenschaften im realen und im Frquenzraum besitzt.

Die mit der Raumsonde Galileo gewonnenen und frequenz-transformierten Daten der Staubströme zeigen verschiedene Charakteristika, die deutliche Variationen von Umlauf zu Umlauf der Sonde um Jupiter während der letzten 29 Umläufe zeigen. Diese Variationen von Umlauf zu Umlauf sind von der Meßgeometrie für Staubteilchen, von den lokalen Plasmabedingungen, und von Io selbst – höchstwahrscheinlich von seiner Vulkanaktivität – abhängig. Das Vorhandensein von Ios Umlauffrequenz um Jupiter demonstriert, daß er wie eine lokalisierte Quelle für geladene Staubteilchen wirkt, wie durch Modulationseffekte bestätigt wird. Diese Zeit-Frequenzanalyse ist der erste direkte Nachweis, daß Io die Quelle der Jupiter-Staubströme ist. Zusätzliche Evidenz für Io gibt die Frquenzanalyse von Staubdaten, die mit Cassini und Galileo während eines "Staubsturmes" im August 2000 gewonnen wurden.

Einige Aspekte der Dynamik der Stromteilchen im realen Raum lassen sich durch veränderliche Teilchenladungen verstehen, die über verschiedene elektrische Ströme erzeugt werden, wenn die Teilchen sich durch das Plasma in der Jupiter-Magnetosphäre bewegen. Eine untersuchte Anwendung ist die Flugzeit der Stromteilchen während gemeinsamer Messungen von Galileo und Cassini im Dezember 2000, bei denen sich die zwei Raumfahrzeuge innerhalb (Galileo) bzw. außerhalb (Cassini) der Jupiter-Magnetosphäre befanden. Zur Erklärung dieser Messungen müssen die Staubteilchen die folgenden Eigenschaften haben: Radius 6 nm, Dichte 1.35 bis 1.75 $\mathrm{g\,cm^{-3}}$, anfängliches Potential: 1 bis 4 Volt, Sekundärelektronenausbeute: 3.0 (abhängig von der maximalen Elektronenenergie im Plasma 300 eV), Ausbeute für Photoelektronen-Emission: 0.1 bis 1.0. Am Ort von Galileo bzw. Cassini liefern diese Geschwindigkeiten der Staubteilchen von 220 bzw. 450 $\mathrm{km\,sec^{-1}}$ sowie Ladungspotentiale von 5.5 bzw. 6.3 V.

TABLE OF CONTENTS

Chapter 1: Introduction **1**

1.1 Why Dust? 1

1.2 Jovian Dust Streams History 2

1.3 Thesis Statement 6

Chapter 2: In-Situ Measurements **9**

2.1 Dust Instruments 9

2.2 Detection of Jovian Dust Streams 10

2.3 Jupiter Millennium Mission 14

Chapter 3: Jovian Dust Streams as Frequencies **17**

3.1 Why Frequency Analysis? 17

3.2 Methods of Time-frequency analysis 17

3.3 Frequency-transformed Galileo Data 20

Chapter 4: Modeling **37**

4.1 Jupiter's Magnetic Field 37

4.2 Jupiter's Plasma 45

4.3 Torus-Magnetosphere Coupling 50

4.4 Dust Particle Densities 51

4.5 Dust Particle Optical Properties 51

Chapter 5: Charging **57**

5.1 Charging Processes 57

5.2 Equilibrium Potential & Charging Times 64

5.3 Dominant Currents 67

5.4 Cassini-Galileo Joint Measurements Currents 67

Chapter 6: Dynamics **73**
6.1 Charged Particle Forces 73
6.2 Ejection from the Jovian Magnetosphere 75
6.3 Traveling SO_x Dust Particle Forces 84
6.4 Dust Velocities vs. Distance 87
6.5 Material Property Explorations 93

Chapter 7: Synopsis **99**

Chapter 8: Going Further **103**
8.1 Ulysses Time-Freq Analysis 103
8.2 Particle's Trajectory Errors 103
8.3 A More Appropriate Magnetic Field 105

Bibliography **107**

Appendix A: Periodogram Derivation **113**

Appendix B: Frequency-Transformed Galileo Data **115**

Appendix C: Corotation **123**
C.1 Derivation of the Corotation Electric Field 123
C.2 Derivation of the Magnetosphere Boundary 125

Appendix D: Field Emission and Electrostatic Disruption **127**

List of Figures **128**

List of Tables **130**

Acknowledgements **131**

Chapter 1

INTRODUCTION

In this chapter, I provide some justification for studying dust and I outline some of the past Jovian dust streams studies.

1.1 Why Dust?

Cosmic dust used to be an annoyance to astronomers because of the way that the dust obscures the object that they wish to observe. When the field of infrared astronomy began, those "nuisance" dust particles were observed to be significant constituents of the Universe and found to be vital components of astrophysical processes.

For example, the dust can drive the mass loss that occurs when a star is nearing the end of its life, those particles are an essential part of the early stages of star formation, and they form planets around other stars. In our own solar system, dust plays a major role in the zodiacal light, Saturn's B ring spokes, the outer diffuse planetary rings at Jupiter, Saturn, Uranus and Neptune, the resonant dust ring at the Earth, and the overall behavior of comets.

Dust evolves in the universe. Dust forms in dusty clouds, cycles through solar systems, through a star's late evolution and back into a nebula. During the dust's evolution, a complex interaction of gravitational and non-gravitational forces govern a dust particle's dynamical behavior. For example, when considering the electromagnetic forces on small and charged particles, one must be aware that dust particles can *respond to* forces in their plasma environment as well as *altering* their plasma environment via the process of accumulating and transferring charges. Therefore, small, charged particles are "tracers" of their astrophysical environments.

Within a solar system, dust is formed and destroyed and some dust is locked into a near-pristine state. The lifetimes of these dust particles are very short compared to the lifetime of the Sun. If one finds grains around a star that is older than 10^8 years,

then the grains *must* have been recently generated. The sources of interplanetary dust particles in our own Solar System include, at least: asteroid collisions, cometary activity and collisions in the inner solar system, Kuiper Belt collisions, and interstellar medium dust grains.

This thesis investigates another, lesser-known source of dust in our solar system: the Jovian dust streams. Dust from this source is a minor dust source compared to collisions of the main belt asteroids and comet activity, nevertheless, it adds to the variety of dust sources in the solar system. At a velocity of $\geq 200\ \mathrm{km\,s^{-1}}$ (Zook et al. 1996), the Jovian dust stream particles can also leave the solar system to slightly populate the local interstellar medium.

1.2 History of the Jovian Dust Streams

The scientific explorations of Io as a source of dust in the Jovian system and the Jovian dust streams have revealed a long and colorful 20 year history. I present a short summary next of the observational history and publication history (here, addressing the question: *What is the origin of the Jovian dust streams?*), then I describe these historical events in more detail.

- Observational History
  - **1979:** Volcanoes on Io discovered by Voyager 1.
  - **1992:** Ulysses discovers the Jovian dust streams.
  - **1993:** Baguhl, M. et al. found more Ulysses dust streams.
  - $\gtrsim$**1995:** Galileo observes the Jovian dust streams.
  - **2000:** Cassini & Galileo observe the Jovian dust streams.

- Publication History
  - **1993:** Grün et al. suggest origin in Jovian system.
  - **1993:** Horányi et al. suggest Io.
  - **1993:** Hamilton & Burns suggest gossamer ring.

- **1994:** Grün et al. consider Comet SL-9.
- **1995:** Maravilla, Flammer and Mendis suggest Io.
- **1996:** Zook et al. show streams faster/smaller than reported before.
- **1996:** Ip demonstrates tiny particle sizes ejected from Io.
- **1996-1997:** Horányi, Grün et al. detailed modeling supports Io as origin.
- **2000:** Graps et al. reveal Io via frequencies.

The Jovian dust streams story began when Io's volcanoes were discovered by the Voyager 1 spacecraft in 1979. Upon that discovery (the first time that active volcanism was seen on another body in the solar system), E. Grün, G. Morfill, and T. V. Johnson published a series of papers (Johnson et al. 1980, Morfill et al. 1980*a*, Morfill et al. 1980*b*, Morfill et al. 1980*c*, Grün et al. 1980) giving a theoretical basis for Io dust generation in the Jupiter system. Voyager 1 arrived in the Jupiter system in March 1979, and Voyager 2 arrived in July 1979. No dust detector instrument was onboard either of these spacecraft, but measurements from the other instruments confirmed that dust was in ample supply in the Jupiter system.

Thirteen years later, when Ulysses was at its closest approach to Jupiter, in March 1992, the dust detector instrument, built by E. Grün and his colleagues, recorded six periodic bursts of submicrometer dust particles with durations ranging from several hours to two days and occurring at approximately monthly intervals (28 ± 3 days) (Grün et al. 1993*a*; Grün et al. 1993*b*). The dust streams were observed in interplanetary space within 2 AU from Jupiter, and the particles arrived at Ulysses in collimated streams, radiating from close to the line of sight to Jupiter, suggesting a Jovian origin.

In 1993, more detailed work on the Jovian dust streams was published and many investigators began to suggest theories for the dust streams' origin with physical models.

Grün et al.'s (1993*b*) article established the Jupiter system as the origin of the dust streams. Horányi et al.'s (1993*b*) work suggested Io as a source for the dust streams. Their model could explain the 28 day periodicity of the data, if the dust grains were small (sizes: 0.03–0.1 μm) and they exhibited speeds in the range:

$30 < v_{exit} < 100$ km s^{-1}. Their model suggested that the periodicity arose from a resonance between the Io orbital and the Jupiter rotational periods.

Hamilton & Burns (1993) presented an alternative model for the origin of the dust streams; they suggested that the masses and velocities of the detected particles were better explained by an origin in Jupiter's gossamer ring.

Baguhl et al.'s (1993) work relaxed the rigid noise requirements of the Ulysses dust instrument and allowed better statistics. After they reanalyzed their data, a much larger number of impacts for the Jupiter dust streams were seen. One clear indication that the Jupiter system was the origin of the streams was that there was a 180° shift of stream mean impact directions before and after the Jupiter flyby.

Horányi et al.'s (1993*a*) work expanded on their model for the dynamics of charged particles in Jupiter's magnetosphere and they considered both Jupiter's rings (ring/halo and gossamer) and Io as a source for the dust streams' particles. Their work favored Io as the source.

Two important events occurred in the Jovian dust streams story in the years 1994–1995. In July 1994, comet Shoemaker-Levy-9 impacted Jupiter, and in December 1995, the Galileo spacecraft arrived in the Jupiter system.

Grün et al. (1994) considered the possibility of comet SL-9, before its time of tidal disruption in 1992, as a source of the dust streams' particles. They found that only two of the eleven Ulysses dust streams would have the right timing and speeds to be the source of Ulysses's dust stream measurements, but they concluded, after further investigation of stream characteristics and dust accelerations mechanisms, that the comet most likely *added* some dust to the Ulysses-detected dust streams, but the comet wasn't a source.

Maravilla et al. (1995) obtained analytic results characterizing grain orbits launched with different velocities and locations in the Jovian system. They conclude that Io is the most likely source of the Ulysses dust stream measurements.

Galileo's dust detector instrument, which is identical to Ulysses' dust detector instrument, observed the Jovian dust streams, both on its way to Jupiter, and in the years since 1995, while in the Jupiter system.

Work continued on the Ulysses dust stream data in 1996, with a paper: (Zook et al. 1996). In their paper, they simulated dust streams detected by Ulysses, tracing

trajectories back in time to Jupiter's location using actual solar wind plasma and magnetic field data, in order to determine the size and speed the particles would have to have in order to arrive at the Ulysses dust detector instrument. From their simulations, they determined that the particles must have been *smaller* and *faster* than previously reported. The new sizes were $\sim 10^{-18}$ g with speeds of > 200 km s^{-1}. Their results were consistent with Horányi et al.'s (1993) model, but not completely consistent with Hamilton and Burns' (1993) model (Hamilton and Burns' particle sizes were larger).

Grün et al.'s (1996*b*) paper reported Galileo's dust detections of the Jovian dust streams for the first time. The spacecraft's dust detector instrument detected the dust streams in interplanetary space on its approach to Jupiter (re-confirming that the source was within the Jovian system), the instrument detected streams within the Jovian system, and it detected dust "storms" as well. The dust streams were similar in duration and intensity to the streams observed by Ulysses, although the streams did not display the one-month periodicity that the Ulysses data of the dust streams displayed. Since Zook et al's recent (1996) work argued for very small and fast dust stream particles, Grün et al. (1996*b*) concluded that the dust streams' particles were outside of the calibrated mass and impact speed ranges. The dust storms, which were detected on the way to Jupiter, were intense (fluctuated by up to a factor 100 in a day), of a month-long duration, with impact rates up to 10 times higher than those rates detected by Ulysses. The authors discussed possible sources of the dust streams in some detail (Grün et al. 1996*b*). They list comet SL9, Jupiter's gossamer ring, or the volcanoes on Jupiter's moon Io, as a potential source of the Jovian dust streams. After ruling out comet SL9, they conclude that the dust streams' source could be either Io, or the gossamer ring.

Grün et al.'s (1997) paper described the dust streams data observed within the Jovian magnetosphere as a continuation of the dust streams observed in interplanetary space out to 2 AU from Jupiter. These data show the same kind of impact magnitude and direction with a smooth transition of the rate from interplanetary space to within the Jovian system. Since Galileo's in-orbit measurements now provide higher time resolution data than the previous dust stream measurements, Grün et al. (1997) could find more detailed frequencies. In particular, they found frequencies that correspond to values of Jupiter's rotation period as seen by Galileo, and a correlation with dust

impact rate and Galileo's position in the Jovian magnetic field.

Horányi et al.'s (1997) work and Heck's PhD thesis (Heck 1999) modeled the above Galileo dust detector data for the early Galileo orbits assuming that Io is the only source of the escaping dust grains, and they succeeded in matching the gross characteristics of the Galileo dust detector data. They described a scenario where the Jupiter dawn-dust electric field, which shaped the Io plasma torus, then ultimately shaped the trajectories of the dust ejected from the Io plasma torus. The trajectories of the particles followed a spiral, much like the motion of water from a sprinkler system. Once the grains begin traveling in the Jupiter magnetosphere, the spatial distribution becomes non-uniform and asymmetric.

The work in this thesis continues the Jovian dust streams story since approximately 1998.

1.3 Statement of the Problem and this Thesis

Indirect methods applied by previous researchers have pointed to Io being the simplest explanation for the question of the origin of the Jovian dust streams. Problem: **Can I show by direct methods that Io is, or Io is not, the source of the Jovian dust streams?** If the answer to that question is 'Yes', then: **Please explain some of the physical phenomena of the Jovian dust streams.**

This dissertation is divided to first address the issue of identifying Io directly in the Galileo dust detector data. In (Graps et al. 2000), which I describe more fully in the chapter 'Jovian Dust Streams as Frequencies', I demonstrate that Io is indeed the source of the Jovian dust streams, by applying time-frequency analysis, in particular, Fourier methods, (however, non-Fourier methods support the conclusions), to the Galileo dust data. Some additional frequency signatures to Io's signal also emerge from the time-frequency analysis, and I show a time-evolution view of the 29 orbits of Galileo dust detector data.

The second part of this dissertation shows that a particle carrying a varying charge can explain some of the features of the Jovian dust streams in real-space. To show how a Jovian dust stream particle travels in real-space, I apply a detailed Jovian particles and fields model by M. Horányi, which I adapted for this thesis, which

simulates a dust stream particle's trajectory as the particle moves from Io's orbit through Jupiter's magnetosphere and beyond. I describe the complex model in the chapter 'Modeling', and I show the results of applying that model in the chapters: 'Charging' and 'Dynamics'. Through the model, I show some charging effects which influence the particle's dynamical behavior, and I apply the model to match the travel time seen in the December 30, 2000, Galileo-Cassini joint dust stream measurements.

The last part of this dissertation gives a synopsis in the chapter: 'Synopsis of Io Revealed in the Jovian Dust Streams', and I describe some paths for future work in which to advance the Jovian dust streams research in the chapter: 'Going Further'.

Chapter 2

IN-SITU MEASUREMENTS

In this chapter, I present the measurements of the Jovian dust streams from the Ulysses, Galileo and Cassini dust instruments.

2.1 Dust Instruments: Ulysses, Galileo and Cassini

2.1.1 Ulysses and Galileo Dust Instruments

The Ulysses and Galileo dust detector instruments are identical dust impact ionization detectors, with a 0.1 m^2 sensitive area and a 140° field-of-view (FOV), which can measure the mass, impact speed, electric charge, and determine the impact direction of individual particles (Grün et al. 1992*a*; Grün et al. 1992*b*). The mass range that the detectors can measure covers 10^{-19}– 10^{-9} kg, and the velocity range covers 2–70 $km\,s^{-1}$. Figure 2.1 shows a schematic configuration of the Galileo dust detector. Up to four charge signals (entrance grid: Q_P, Ion: Q_I, Target: Q_E, Channeltron: Q_C) are used to identify dust impacts. Positively or negatively charged particles enter the sensor, where a Q_P signal is registered, and the particle then generates an impact ionization cloud on the hemispherical impact sensor. After the ions and electrons of the ionization plasma are separated by an electric field, they are each collected separately providing two nearly coincident pulses Q_I and Q_E. The rise times and heights of these pulses empirically determine the particle's impact speed and mass. The particle's impact direction (rotation angle) is determined by the spin position of the spacecraft at the time of impact. The Jovian dust stream particles are faster than the calibrated velocity range, and approach the detector in collimated streams (Krüger et al. 1999) registering an almost noise-free "class 3" dust impact, which refers to the fact that three charge signals are generated for that impact. Impact events on the dust detectors are also separated into amplitude ranges AR1 to AR6,

where AR1 contains mostly the tiny dust stream particles, and hence, AR1 was the amplitude-range data used in this thesis.

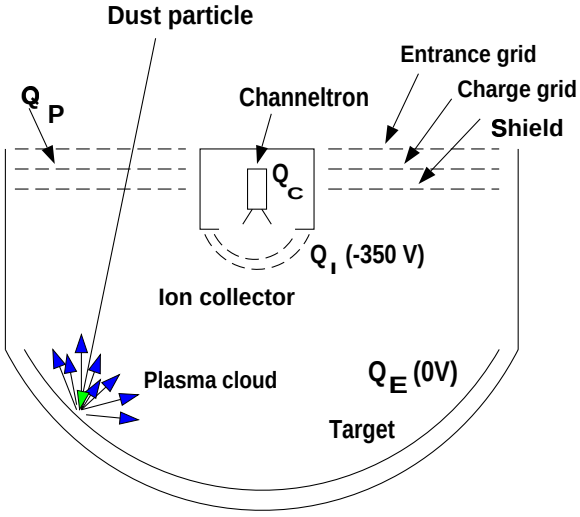

Figure 2.1 : A schematic configuration of the Galileo dust detector. See text for a more detailed description.

2.1.2 Cassini Dust Instrument: CDA

The Cassini CDA dust instrument is also an impact ionization detector, based on the the successes of the Galileo and Ulysses dust detectors. The CDA detector also has capabilities to measure the dust particle's electric charge, impact direction, impact speed, and mass (Srama & Grün 1997). In addition, this dust detector contains a time-of-flight mass spectrometer, to provide the chemical composition of impacting dust particles. The mass range that the detector can measure covers 10^{-19}–10^{-9} kg.

2.2 Galileo and Ulysses' Detection of the Jovian Dust Streams

In March 1992, while traveling by the Jovian system in interplanetary space, the Ulysses dust instrument detected the Jovian dust streams. After a careful reexamination of the data (Baguhl et al. 1993), a total of eleven streams, spaced approximately 500 R_J (where R_J=7.1339 10^9 cm is the equatorial radius of Jupiter) apart,

and occurring at approximately monthly intervals, were recorded and analyzed. Since the dust streams are smaller and faster than the calibrated ranges of the instrument, empirical methods were used by Zook et al. (1996) to find at what speed and mass the particles should be, in order to be detected at the Ulysses spacecraft. The particles' masses were calculated to be of the order of 10^{-18} g (particles' with a charge to mass ratio of 1000 C/kg), and the dust grain velocities were found to exceed 200 $\mathrm{km\,s^{-1}}$. Figure 2.2 shows the Ulysses dust stream impact rate data.

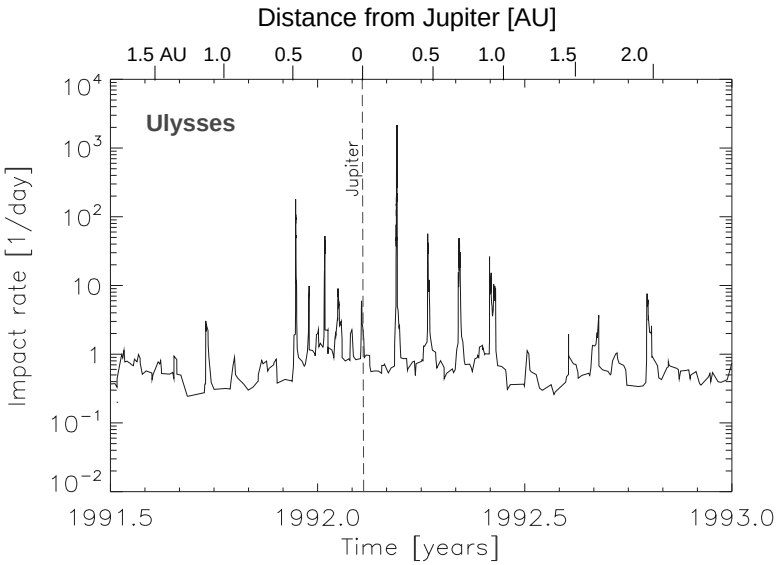

Figure 2.2 : Ulysses dust detector rate of dust impacts of the Jovian dust streams.

In 1995, while en-route to the Jovian system, the Galileo dust instrument detected the Jovian dust streams. The Galileo interplanetary Jovian dust streams were similar in duration and intensity to Ulysses' dust detections, although the Galileo detections did not display the one-month periodicity that the Ulysses dust streams displayed. The impact rate data was highly time-variable, with an intensity that varied by at least a factor of 1000 between the weakest and the strongest streams observed by Galileo and Ulysses (Grün et al. 1996*b*). Figure 2.3 shows the interplanetary Galileo dust stream data.

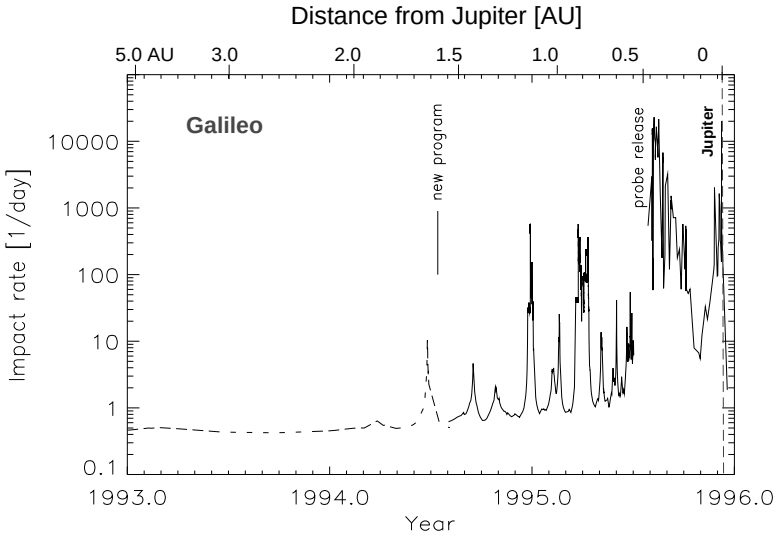

Figure 2.3 : Galileo dust detector rate of dust impacts of the Jovian dust streams in interplanetary space.

2.2.1 Galileo Impact Rates and Fluxes

The Galileo dust instrument is mounted on the spinning portion (rotation angle 0 to 360°) of the spacecraft, its centerline offset from the spacecraft spin axis by 60°, and subtending a 140° field-of-view (see sketch: Fig. 2.4). The line of apsides of the spacecraft's orbital ellipse shifts over time, and due to the detector's geometrical orientation, the Galileo dust instrument captures dust stream particles at different locations in its trajectories during the mission. The effective area of the detector changes with time because it is dependent on the impact direction of the dust particle.

In order to grasp the orientation of the dust streams and the spacecraft orbital geometry, I show a diagram (Fig. 2.4) for the physical picture in late-1997, of the dust stream particles coupled to Jupiter's magnetic field overlaid on a leg of one of Galileo's orbital trajectories. Note that on the approach leg, they can enter the dust detector, whereas on the receding leg, the dust streams approach Galileo from outside the detector field-of-view. Therefore, the Galileo instrument (in 1996-1997) captured most of the dust stream particles during the inbound leg of Galileo's orbital trajectory. Since Galileo's orbital speed is $\leq$ 20 km s^{-1} and the dust streams' speed is $\geq$ 200 km s^{-1}, Galileo, to first order, is a stationary observer with respect to the

dust streams.

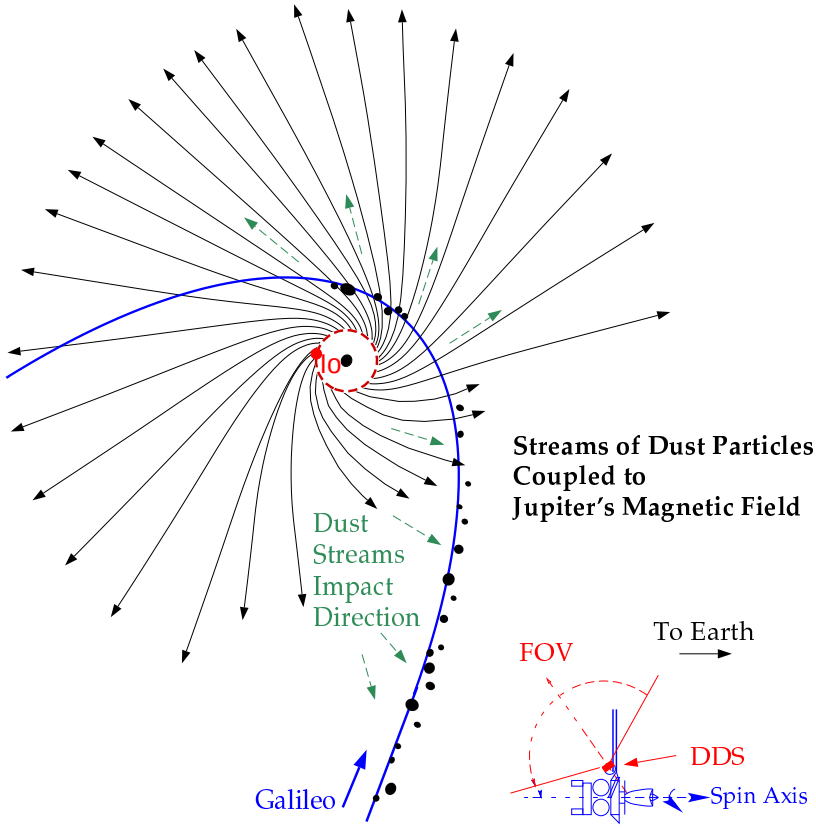

Figure 2.4 : Sketch of one of Galileo's orbital trajectories from late-1997 overlaid with trajectory results from a dust stream particles model (Horányi et al. 1993*a*). The Galileo orbital trajectory is indicated with a solid blue line and the dust streams' impact direction is indicated with the dashed green arrows.

The following figure, Fig. 2.5, displays the Galileo dust impact fluxes calculated by H. Krüger for the Galileo orbits up to the present time, through orbit G29. The fluxes shown in this figure demonstrate that when the spacecraft was in the inner Jovian system, usually on the inbound leg, the fluxes were high, and when the spacecraft was further away, the fluxes were low. The exception was the orbit G28, which is the orbit that reaches near to the top of the figure. In orbit G28, Galileo was outside of the Jovian magnetosphere and the fluxes measured were unusually high. I discuss a dust "storm" detected by Cassini and Galileo in summer 2000, during this orbit G28, in the section 3.3.2. Figure 2.5 also displays the trajectory (the solid diagonal line

that intersects near the top left corner) of Cassini's December 2000 Jupiter flyby, with Cassini's dust impact fluxes during the dual-spacecraft measurements color-coded to the same scale as Galileo's fluxes.

I show a typical Galileo dust impact rate dataset for one orbit around Jupiter in the following figure, Fig. 2.6. This particular orbit, orbit E17, displays many of the periods, which I determined via spectral analysis, in chapter 3, in this thesis.

2.3 The Jupiter Millennium Mission

On December 30, 2000, the Cassini spacecraft closely flew by Jupiter, providing a simultaneous two-spacecraft measurement (Cassini-Galileo) of particles from a collimated stream of the Jovian dust streams. Particles in a stream were detected by Galileo, as the spacecraft was orbiting inside of the Jovian magnetosphere close to Ganymede (8–12 R_J), and then particles in the stream travelled to Cassini, as Cassini flew by Jupiter at approximately 140 R_J. Figure 2.7 shows the dust impact rate data for the dual dust stream measurements, the gold line denotes the Galileo rates and the green line indicates the Cassini rates. We assumed that the same dust stream at each spacecraft began where the black horizontal line marks the midpoint of the peak rise in impact rate. The travel time between the two black-marked peaks is approximately 7 hours. Matching this travel time is one goal of this thesis work.

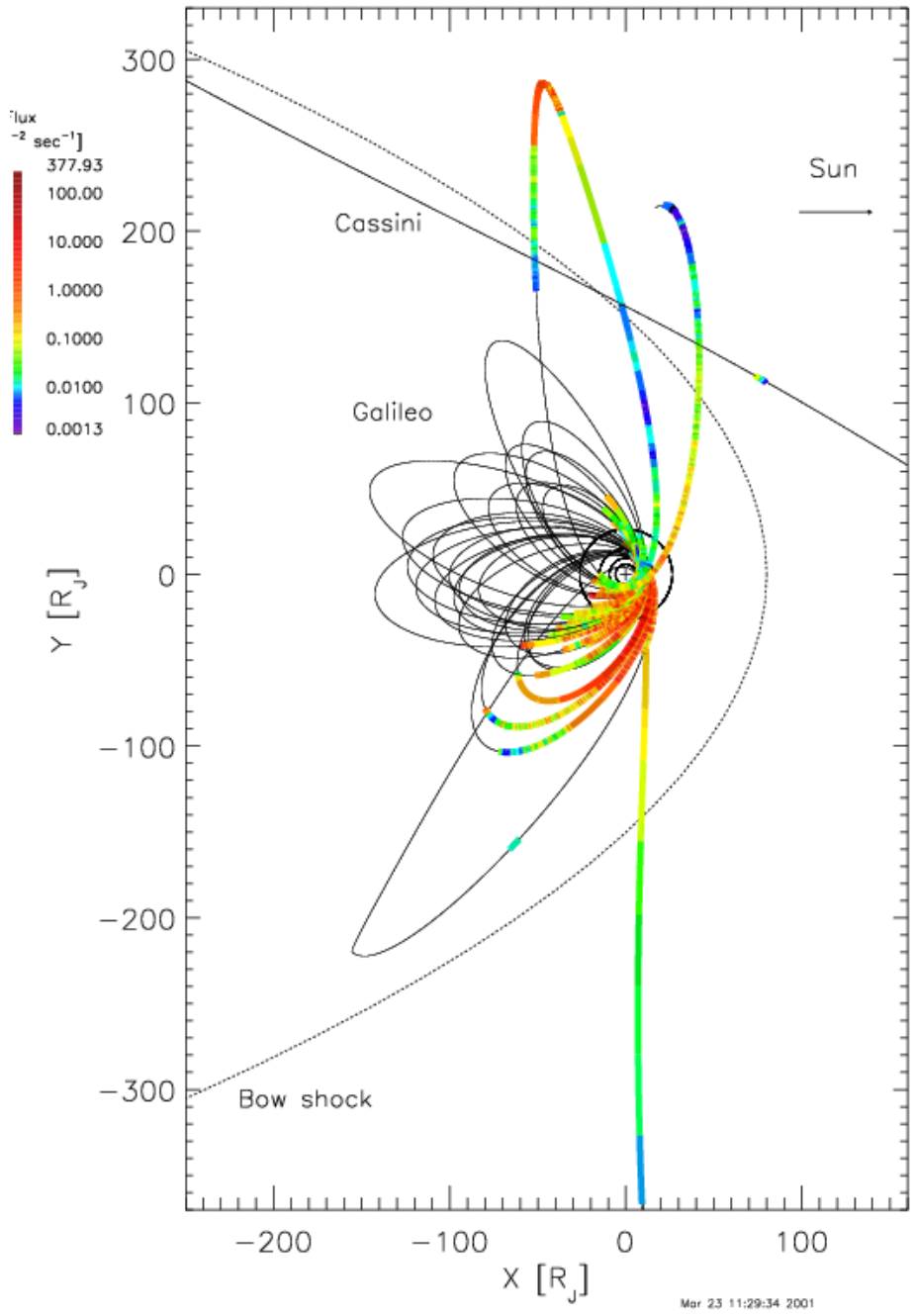

Figure 2.5 : Galileo impact fluxes for all orbits up to the present time (orbit G29). The dust impact fluxes are color-coded to the scale shown in the upper-left colorbar. Cassini's Jupiter flyby trajectory is the diagonal line which intersects near the top left corner, with the dual spacecraft measuremnts of the Jovian dust streams color-coded to the same flux scale as Galileo's measurements. Jupiter's magnetosphere bow-shock is indicated by the dotted line.

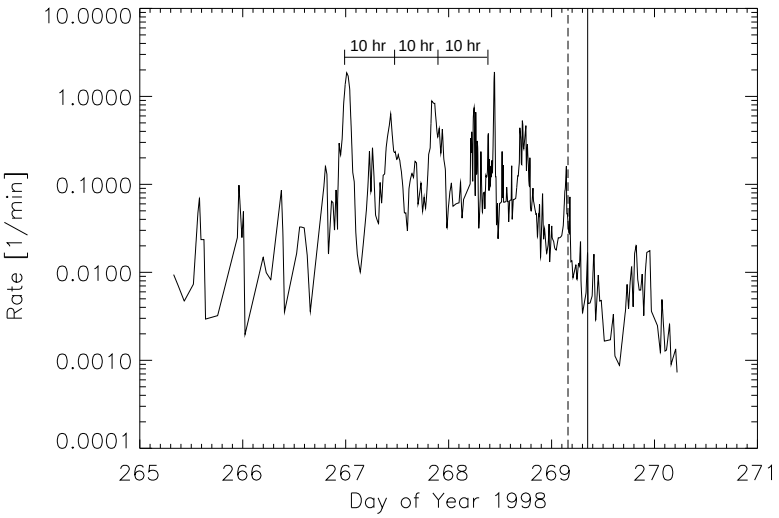

Figure 2.6 : Galileo dust stream rate measurements for the Galileo Europa 17 orbit flyby (closest approach to Jupiter: September 26, 1998). The dust data for this encounter is a good example of the small, charged dust stream particles coupling to Jupiter's magnetic field, resulting in high impact rates in roughly 5 and 10 hour periods. The 10 hour periods can be seen as the dominant peaks, and the 5 hour periods can be seen as smaller peaks within those dominant peaks. The vertical dashed line marks the closest approach to Europa, and the vertical solid line marks the perijove passage.

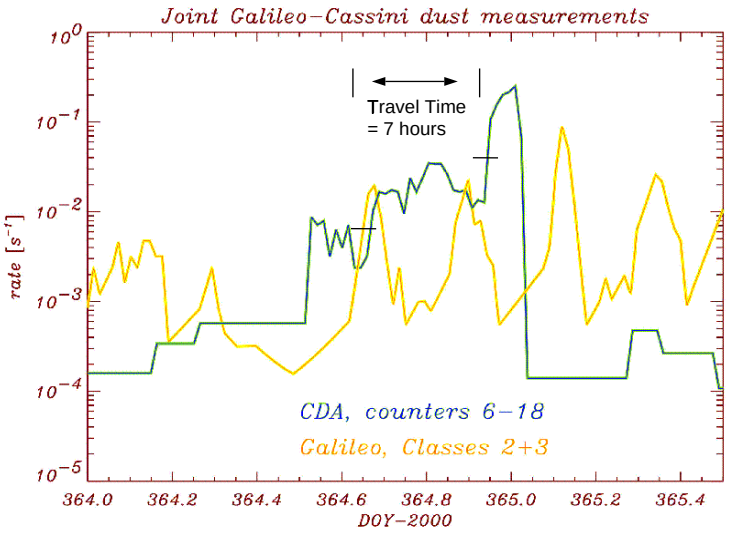

Figure 2.7 : Dust impact rates from the Cassini-Galileo dual dust stream measurements performed on December 30, 2000. The marked travel time, 7 hours, is the time for a dust particle in a collimated dust stream to travel from Galileo to Cassini.

Chapter 3

JOVIAN DUST STREAMS AS FREQUENCIES

In this chapter, I show that Io is a source of the Jovian dust streams by Fourier techniques, where one can see Io's orbital period, Jupiter's period/half-period or rotation, and Jupiter's frequency modifying Io's frequency via amplitude-modulation. I show that the frequencies from orbit-to-orbit are variable. I also show that a non-Fourier technique, the continuous wavelet transform, can confirm some of these signatures and give indications of new frequencies and frequency-interactions.

3.1 Why Frequency Analysis?

The time variation of a signal is fundamental because time is fundamental. After time, the next most important representation of a signal is frequency. Frequency analysis is important for several reasons: 1) One can learn about the signal source via breaking apart the signal into its separate frequency components (spectral analysis), 2) one can learn about the different media (dispersion) through which the waves travel, and 3) spectral decomposition often simplifies our understanding of the signal and the physical phenomena behind the signal. Time-frequency analysis enables us to classify signals with a considerably greater reflection of the physical situation than can be achieved by the spectrum alone. The following table shows a list of some frequencies and periods (1/frequency) that we might see in and around the Jovian system.

3.2 Methods of Time-frequency analysis

Nature does not break up a signal for us in terms of time, frequency, amplitude and phase. Nature only gives us the signal, which can have any functional form. Therefore,

Frequencies Related to Charged Dust		
Physical Process	**Frequency**	**Period**
Inside the Jovian System		
Jupiter's rotation w/attached mag field		
Full period	2.44 d^{-1}	9.84 hr (0.41 d)
Harmonics (1/2 period)	4.87 d^{-1}	4.92 hr (0.20 d)
Satellites (Orbit/Rotation)		
Io	0.56 d^{-1}	42.46 hrs (1.77 d)
Europa	0.28 d^{-1}	85.25 hrs (3.55 d)
Ganymede	0.14 d^{-1}	171.72 hrs (7.15 d)
Callisto	0.06 d^{-1}	400.54 hr (16.69 d)
Modulation Products (AM, FM, Beats, etc.)		
Doppler shifts		
Larmor frequency		
Resonances?		
Plasma waves?		
Outside of the Jovian System		
Jupiter's rotation w/attached mag field		
Full period	2.44 d^{-1}	9.84 hr (0.41 d)
Io (Orbit/Rotation)	0.56 d^{-1}	42.46 hrs (1.77 d)
Solar wind		24–32 d

we must depend on mathematical techniques, and on the work of Fourier, Bunsen, Kirchoff, Daubechies and other scientists to find an appropriate time-frequency representation of our signal. I utilized primarily Fourier methods, in order to look for Io's signature, however, I implemented a non-Fourier method, the continuous wavelet transform, as well. First the Fourier method.

3.2.1 Fourier Transform Methods (e.g. the periodogram)

The "classic" or Schuster periodogram (Bretthorst 1988) is conventionally defined as the modulus-squared of the discrete Fourier transform. If the input time series

contains a periodic feature, then the periodogram can be calculated for any frequency ω, and it displays the presence of a sinusoid near one frequency value as a distinct peak in the spectrum. The terms *power spectrum* and *periodogram* are often used interchangeably, but the distinction is that the power spectrum is a quantity of an integral over continuous time, and the periodogram is an estimate based on discrete data.

The Lomb-Scargle periodogram is a slightly modified version of the classic periodogram giving a simpler statistical behavior (Scargle 1982). It is a general, linear, least-squares regression of unevenly-spaced data to a sine/cosine series of different frequencies. In the Appendix, I provide a derivation of the Lomb-Scargle periodogram. Some nice features of the Lomb-Scargle periodogram are: 1) it weighs the spectral fit appropriately by the actual data points, 2) it takes advantage that some data is clustered more tightly than the average Nyquist interval (e.g. you can pick out the higher frequencies), and 3) it exhibits no aliasing.

3.2.2 Non-Fourier transform methods (e.g. the wavelet transform)

Wavelets have a mathematical dual time-scale representation that cut up data into different frequency components, and then study each component with a resolution matched to its scale (Graps 1995). Wavelets hold some advantages over traditional Fourier methods when analyzing physical situations where the signal contains discontinuities and sharp spikes. With a wavelet transform, one can see the signal simultaneously in time (on the x axis) and in frequency/period (on the y axis). One could consider the wavelet transform as a *projection* in frequency space: high coefficient wavelet values are those wavelet basis functions which approximate the dataset well, and low coefficient values as those wavelet basis functions that do not approximate the dataset well.

The continuous wavelet transform (CWT) has arbitrary scales and times and provides a "smooth" picture of the wavelet power spectrum because it *oversamples* the dataset, i.e. the wavelet basis functions overlap each other. In the continuous wavelet transforms I implemented for this thesis, I used the Morlet wavelet.

3.3 Time-frequency analysis of Galileo Dust Detector Data

3.3.1 Orbit-by-Orbit

If I transform the Galileo dust detector data, orbit-by-orbit, into frequency-space via periodograms, then we have the frequency-transformed Galileo data seen in Table 3.1, in the Appendix, and in the next three figures: Fig. 3.1, Fig. 3.2, and Fig. 3.3. The orbital dates refer to apojove-to-apojove only (future improvements to this table will show the times for which real-time data were available). The Notes column of Table 3.1 refer to features, in the individual orbit-by-orbit periodograms (see the Appendix), of which I noted 'by eye', periods at '10 hr', '5 hr', 'Io's period', or the 'modulation' signature (explained in section 3.3.4).

The Galileo dust detector periodogram data shows variabilities, orbit-to-orbit, even for some orbits which share similar orbital geometry (although the effect is more pronounced in the earlier orbits, than in the later orbits, since in the latter, the spacecraft dust detection geometry was also changing more rapidly). This orbit-to-orbit variability is a clue that, either the intervening medium or Io itself, i.e. its volcanoes, is a source of the variability.

Some early examples of this variability: In orbit E4, Io, Jupiter's full rotation frequency, and the first hint of a modulation effect with Jupiter's rotation frequency (see next section) are visible, yet in orbit E6, which shares a similar orbital geometry, Io and the modulation effect disappears. In orbit G7, Io, Jupiter's full rotation frequency, and the same modulation effect with Jupiter's rotation frequency, show clear signatures, yet in orbit G8, which shares a similar orbital geometry, Jupiter's full period of rotation and the modulation disappears. A later example of this variability is described in the next section, when both Galileo and Cassini detected a "dust storm" during the summer of 2000.

3.3.2 August-September 2000 Dust Storms

In August and September 2000, both Cassini ($\sim$1 A.U. from Jupiter), and Galileo ($\sim$250 R_J from Jupiter) detected increases in the rate of dust impacts, which were approximately 100 times their nominal impact rates. In the frequency-transformed data from both spacecraft, Io's frequency signature swamped all other frequency signatures

Table 3.1 : Time-evolution of Frequencies, Galileo Orbit-by-Orbit

Orbit, Date, Day-of-year	**Frequency Notes**
G1, 1996: 80 – 214	10 hr, 5 hr
G2, 1996: 214 – 281.6	10 hr & 5 hr equal strength, clean
C3, 1996: 281.6 – 332.9	5 hr, clean, mushy 10 hr
E4, 1996: 332.9 – 1997: 5.1	10 hr, 1^{st} modulation hint
E6, 1997: 36.0 – 73.2	10 hr
G7, 1997: 73.2 – 111.5	1^{st} clear modulation
G8, 1997: 111.5 – 153.5	5 hr (no 10 hr or modulation)
C9, 1997: 153.5 – 220.2	messy
C10, 1997:220.2 – 286.5	clear modulation
E11, 1997:286.5 – 336.0	strong 10 hr & 5 hr
E12, 1997: 336.0 – 1998: 13.0	Io, only hint 10 hr & 5 hr
E14, 1998: 65.0 – 122.0	strong 10 hr & 5 hr & 2.5 hr(?)
E15, 1998: 122.0 – 178.0	only hint 10 hr
E16, 1998: 178.0 – 236.0	many small humps, equal strength
E17, 1998: 236.0 – 299.0	hint Io, 10 hr & 5 hr, other humps
E18, 1998: 299.0 – 363.0	strong Io, strong modulation, little data(!)
E19, 1998: 363.0 – 1999: 78.0	unknown feature at 16 hr
C20, 1999: 78.0 – 155.0	strong Io, only hint 10 hr & 5 hr
C21, 1999: 155.0 – 204.0	no distinguishable features
C22, 1999: 204.0 – 242.0	strong Io ('split')
C23, 1999: 242.0 – 271.0	only Io, 10 hr & 5 hr disappeared
I24, 1999: 271.0 – 307.0	only hint Io, 10 hr & 5 hr disappeared
I25, 1999: 307.0 – 341.1	almost all Io (hints 10 hr, 5 hr, 2.5 hr)
E26, 1999: 349.1– 2000: 4.1	peak at 25 hr swamps all
I27, 2000: 28.2 – 53.5	almost all Io (no 10 hr)
G28, 2000: 97.2 – 142.2	almost all Io (10 hr, 5 hr shifted?)
G29, 2000: 363.0 – 2001: 71.6	Io, 10 hr, 5 hr, modulation, mushy, 3.5 hr(?)

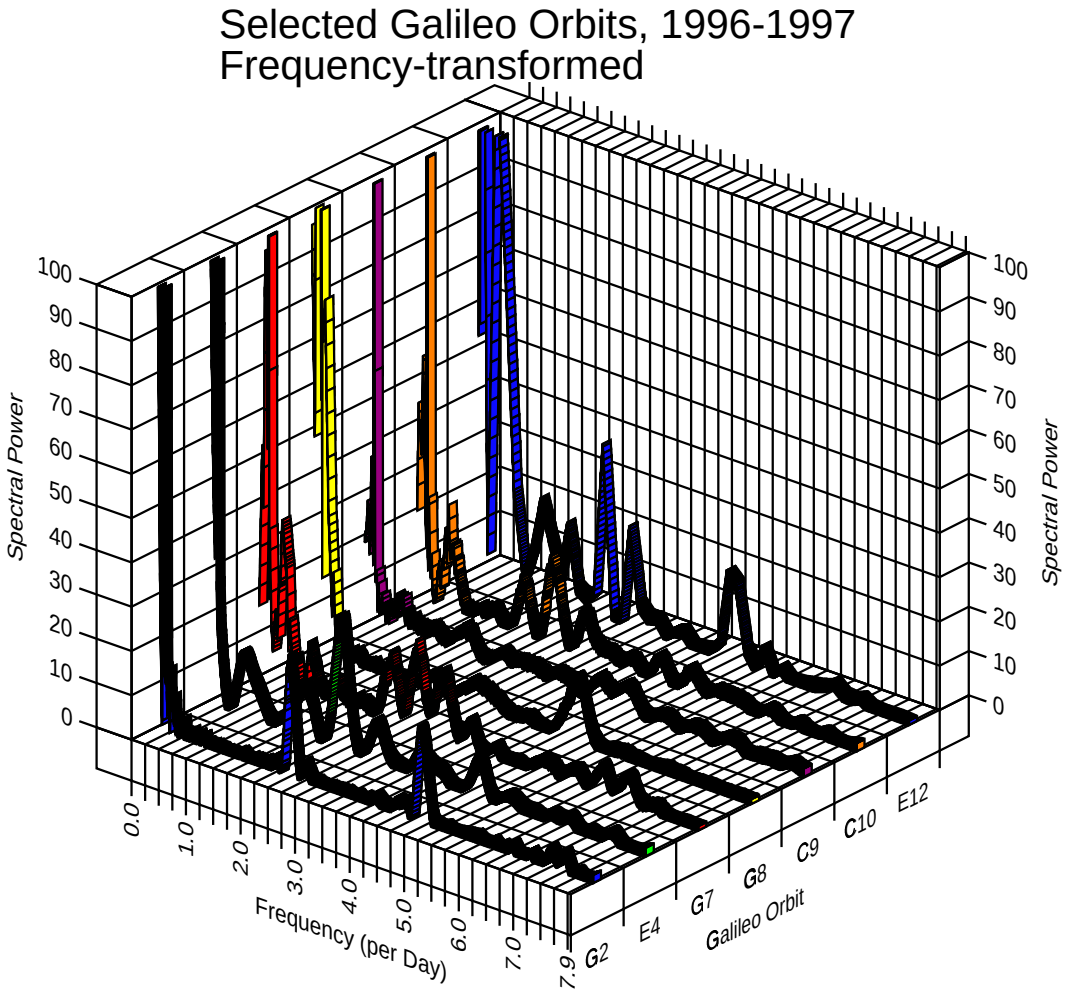

Figure 3.1 : A Lomb-Scargle periodogram of selected individual orbits for the first two years, 1996-1997, of Galileo dust impact rate data.

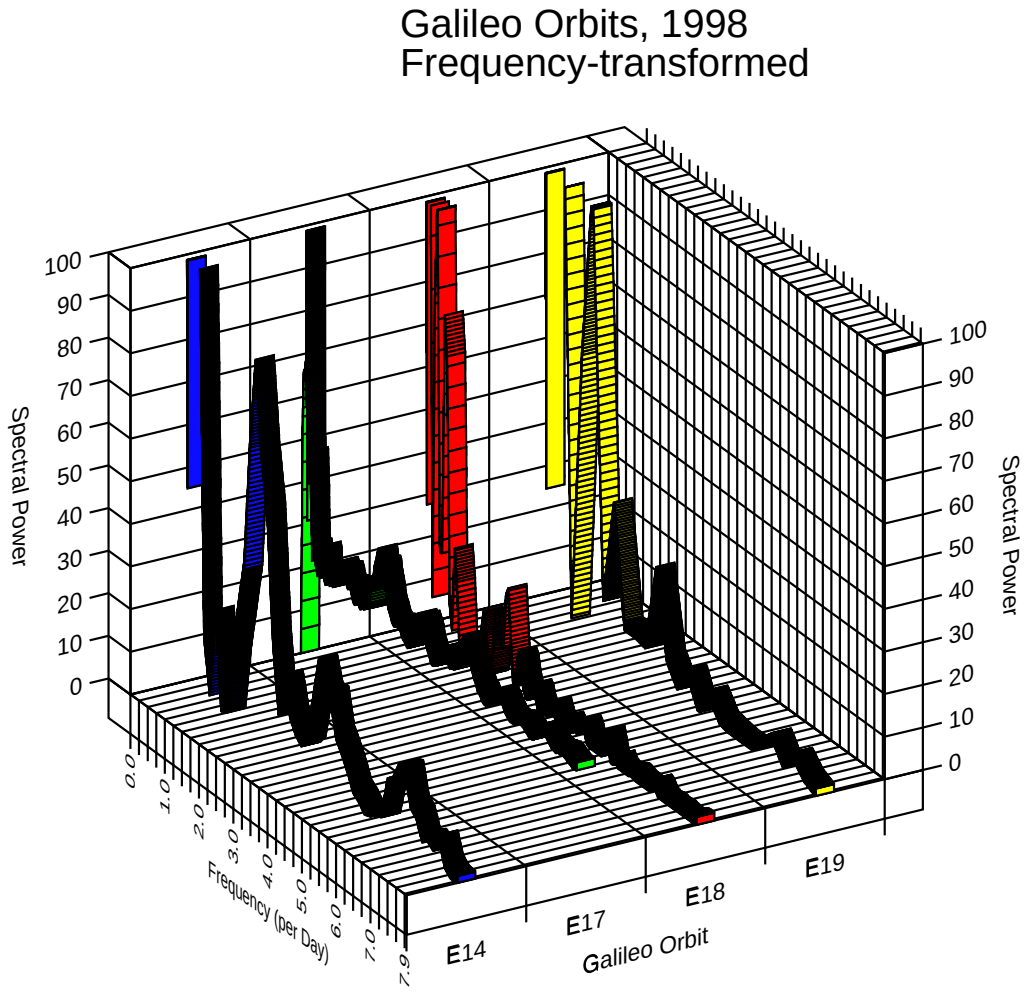

Figure 3.2 : A Lomb-Scargle periodogram of the individual orbits for the year: 1998, of Galileo dust impact rate data

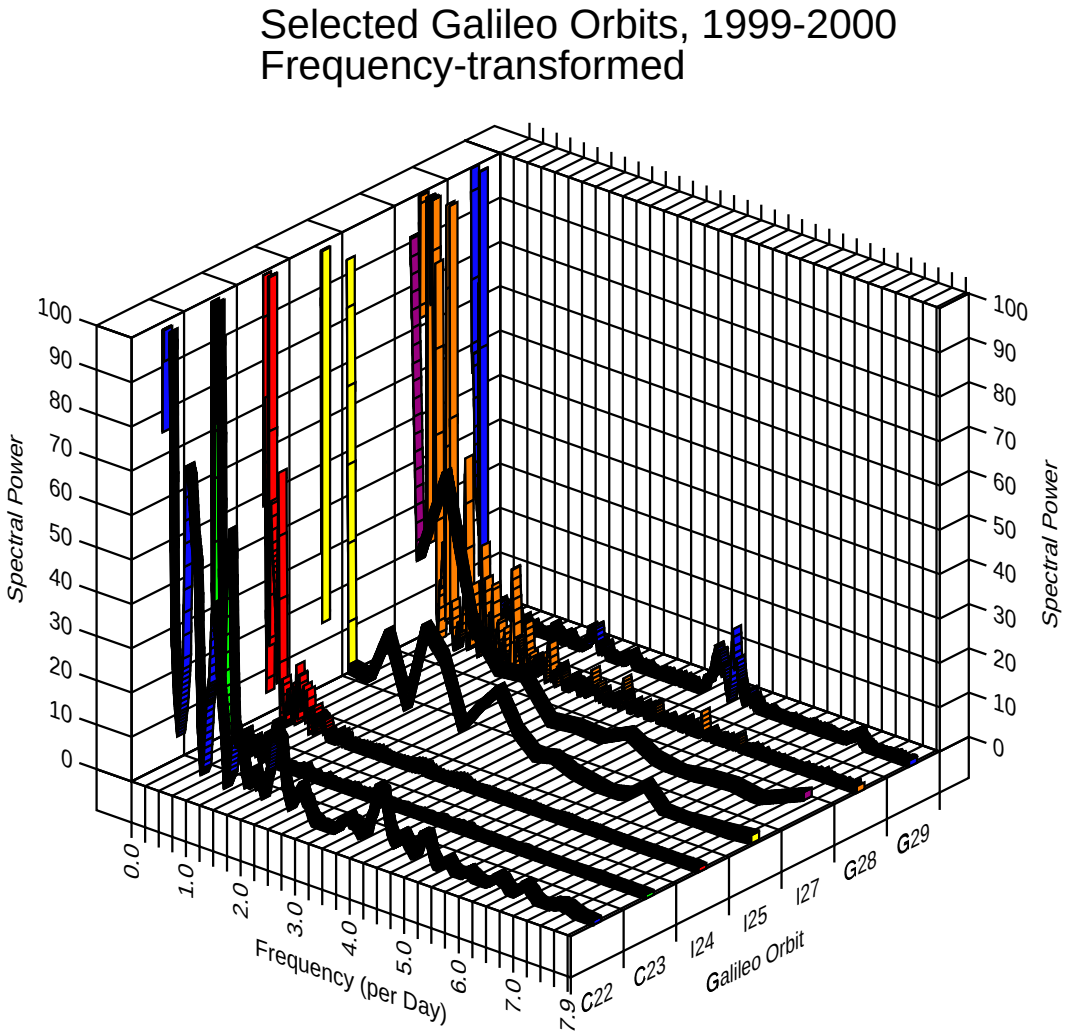

Figure 3.3 : A Lomb-Scargle periodogram of selected individual orbits for the years, 1999-2000, of Galileo dust impact rate data

in the Galileo data, which was noteworthy, because both spacecraft were located far from Jupiter, outside of Jupiter's magnetosphere. Galileo detected the 'dust storms' earlier during the perijove portion of its G28 orbit, during Days ∼218–240 (see the periodogram of the dust impact rate in Fig. 3.4). After Day 240, Galileo's impact rate decreased, however, Cassini observed high impact rates particularly on ∼Day 251 and ∼Day 266 (see the periodogram of the dust impact rate in Fig. 3.5). Cassini's dust detector's observational geometry is very different from Galileo's, however, by accident, Cassini captured the dust storm approximately 1-2 weeks after Galileo detected the dust storm.

Many of the frequency peaks that appear in the periodograms can also be seen using a non-Fourier, frequency-transform technique, the continuous wavelet transform. With a wavelet transform, one can determine *when* any strong frequencies in the signal appear, because the wavelet transform provides a two-dimensional view on one's data in frequency-space. The next figure, Fig. 3.6, displays a continuous wavelet transform of the Galileo dust 'storm' data during Days 217–247.

3.3.3 Periodogram of 1996-1997 Galileo Dust Detector Data

Not all Galileo orbital trajectories were optimal for detecting Jovian dust stream particles. The spacecraft orbital geometry of the first years of the Galileo mission favored higher fluxes of dust stream particles, therefore, if I combine two years of the early data, I gain a higher signal-to-noise dataset, in which to transform into frequency-space. In the next figure, Fig. 3.7, I show a Lomb-Scargle periodogram for the first two years, 1996-1997, of Galileo dust impact rate data. This particular periodogram is the best example from the Galileo dust detector data showing, with high confidence: Io's frequency signature, Jupiter's frequency signatures, and amplitude modulation effects (see next section.) I first give a summary of the features seen in this periodogram, then I describe the features in more detail in the subsequent sections. This particular periodogram was published in Graps et al. (2000).

Frequency Summary of Fig. 3.7:

1. A strong peak near the origin,
2. An asymmetric peak: maximum at 0.6 day^{-1}, center at 0.7 ± 0.2 day^{-1},

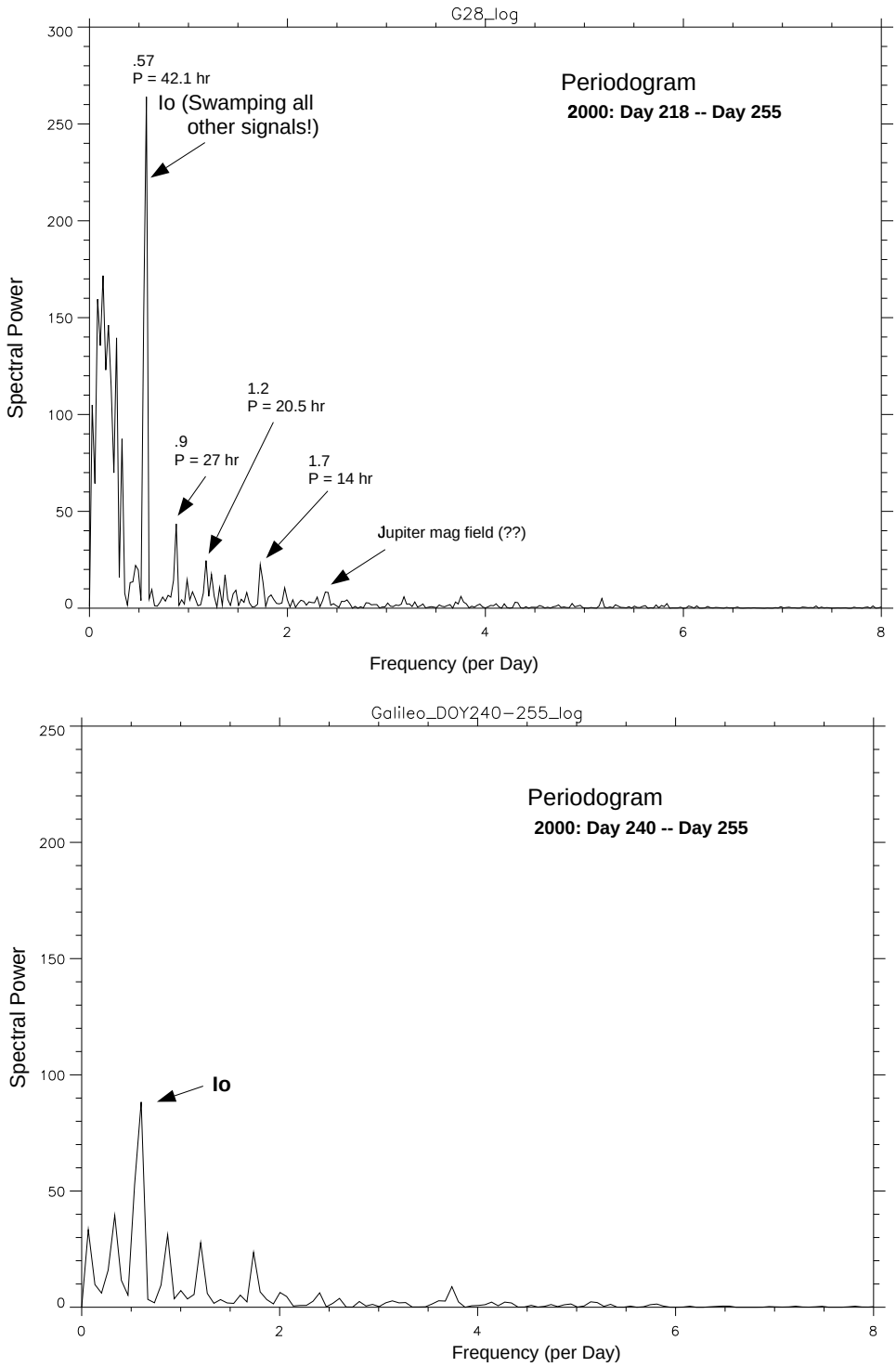

Figure 3.4 : A Lomb-Scargle periodogram of selected days of dust impact rate data from Galileo's G28 orbit, when the spacecraft was located outside of Jupiter's magnetosphere at ~250 R_J. This Io dust streams storm detected in interplanetary space was stronger in the earlier portion of this orbit close to perijove on Days 218–240 (top panel), than in the later days (bottom panel), when Cassini detected the storm.

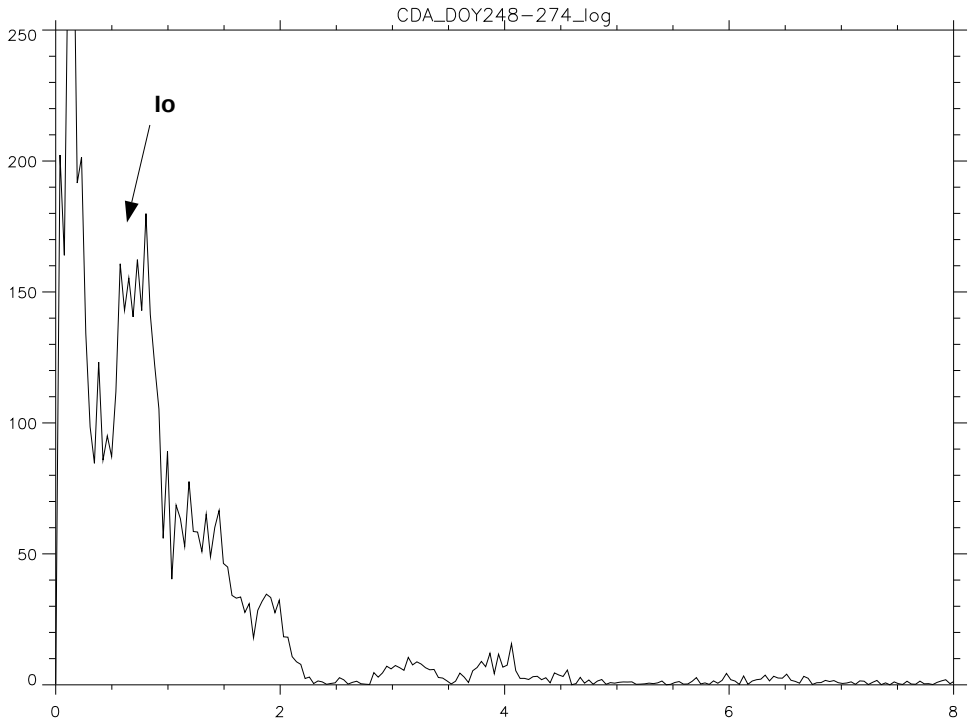

Figure 3.5 : A Lomb-Scargle periodogram of Cassini CDA impact rate data during 2000: Days 248–274. Cassini observed high impact rates particularly on ∼Day 251 and ∼Day 266, when the spacecraft was traveling far outside of Jupiter's magnetosphere at ∼1 A.U.

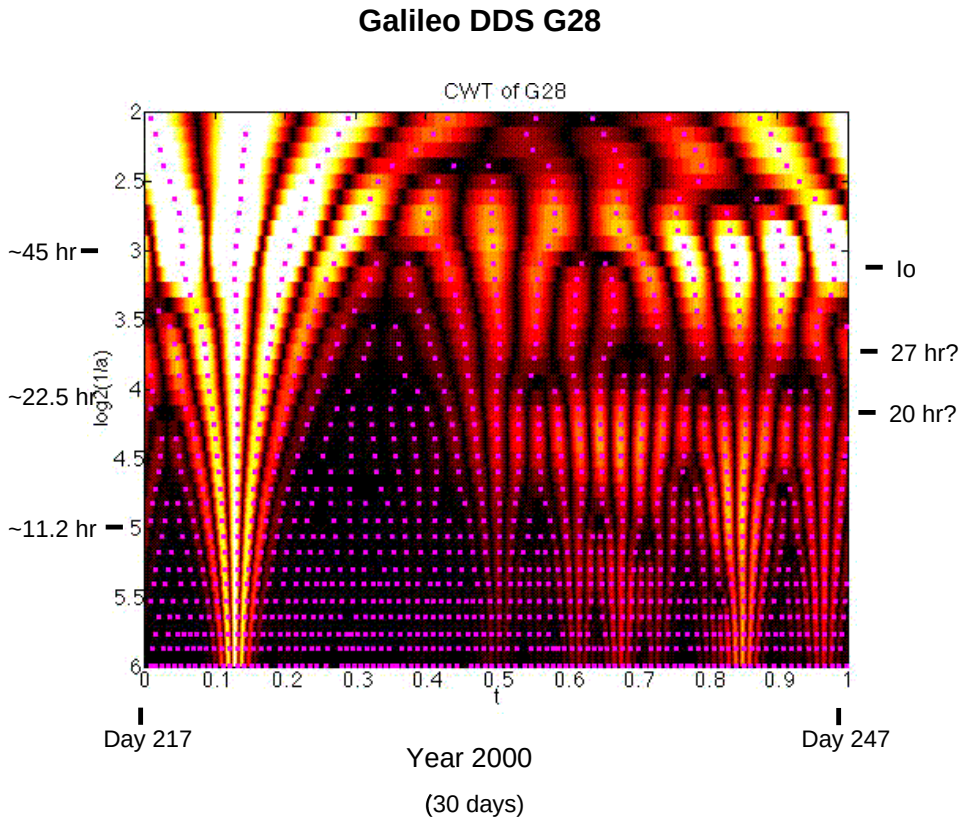

Figure 3.6 : A continuous wavelet transform (CWT) of the Galileo dust impact rate data during 2000: Days 217–247. The locations where the Morlet wavelet basis function favorably projects onto the data gives high-value wavelet coefficients, which are light-colored. Repeated patterns indicate a frequency signature. In this CWT, Io's frequency signature is strong in the early and the later portions of the time. A 27 hr and 20 hr period signature also appears, which can be seen as a repeated red pattern underneath the strong light-colored Io signature.

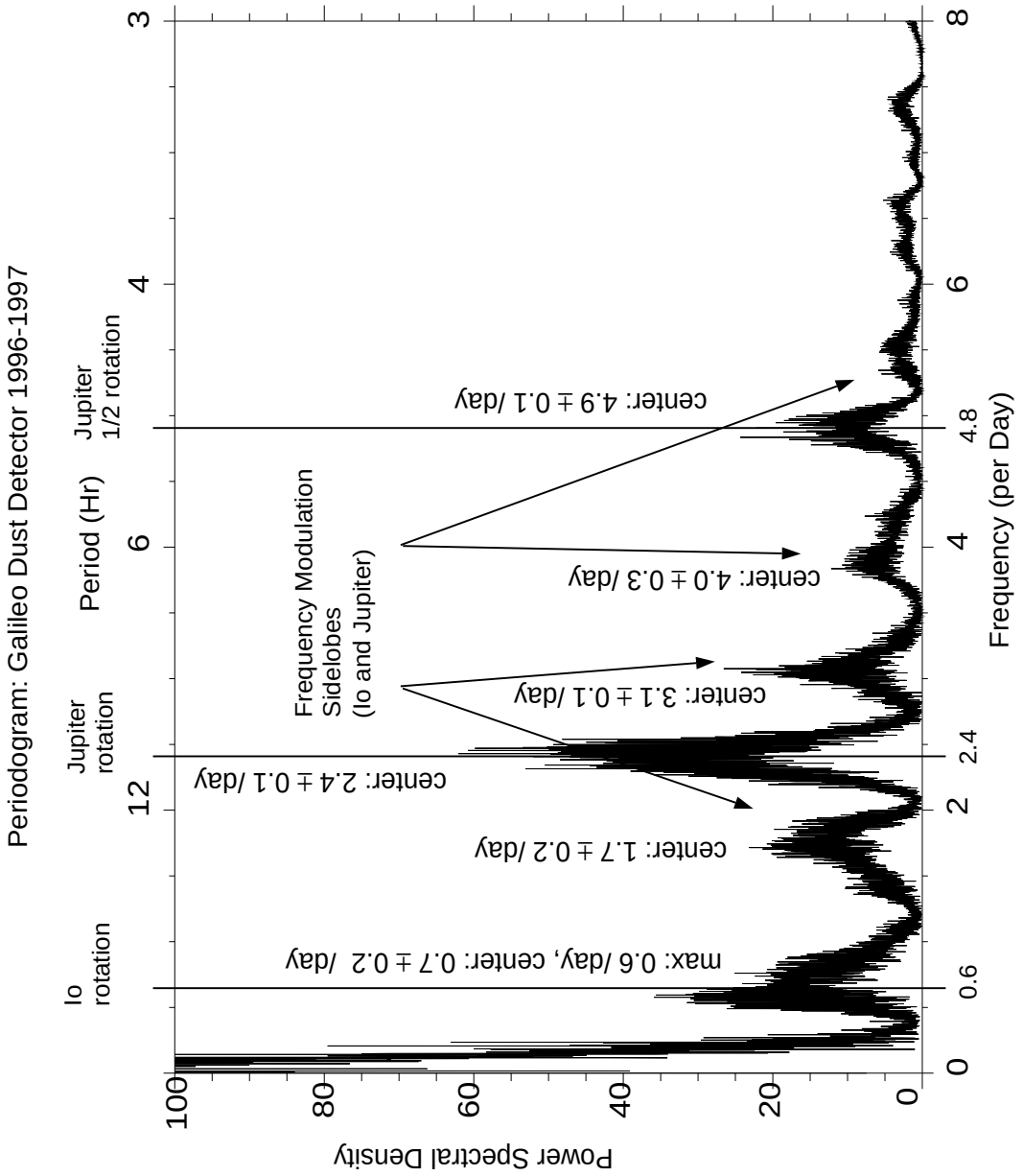

Figure 3.7 : A Lomb-Scargle periodogram for the first two years, 1996-1997, of Galileo dust impact rate data, with the specific signatures described in the text. Io's frequency of orbital rotation, in particular, can be seen here in frequency-space, which provides our first direct evidence that Io is a source of the Jovian dust streams. A confirmation of Io's role as a localized charged dust source arises through the modulation effects.

3. An asymmetric peak: center at 1.7 ± 0.2 day^{-1},
4. A tall peak: center at 2.4 ± 0.1 day^{-1},
5. A peak: center at 3.1 ± 0.1 day^{-1},
6. Harmonics of the previous three peaks, and
7. Progressively smaller and less-defined peaks.

The vertical solid lines mark Io's orbital and Jupiter's rotational periods, and the arrows point to Jupiter's modulation products with Io straddling Jupiter's frequency. The first harmonic of Jupiter's rotation frequency is visible at ($\omega_1 = 4.8$ day^{-1}) and Jupiter's modulation products with Io, which are straddling that first harmonic peak, can be seen, as well. The strong frequency peak near the origin at 1 over Galileo's orbital period is due to the Galileo spacecraft orbital geometry. Now describing this summary in more detail. I considered the following aspects of this particular periodogram:

- Noted frequency patterns. (e.g. Modulations.)
- Compared periodogram with synthetic data.
- Noted any spacecraft effects. (e.g. Doppler shifts.)
- Calculated error bars. (e.g. Gaussian curvefit to peaks.)
- What is the amount of dust from Io as a point source? (e.g. Integrated under peaks.)

3.3.4 Modulated Oscillations and the Application to Io and Jupiter Dust

Frequencies in frequency-space can interact in numerous ways. Here I discuss the *modulation* of oscillation frequencies with the following definition.

If two independent oscillations of any kind occur at frequencies ω_0 and ω_1, and they are observed simultaneously, and if one oscillation is allowed to interact with another oscillation such that the observable signal from the first oscillation (our "carrier") is modified by the second oscillation process, then our carrier signal is *modulated.* I provide, next, the mathematical formulation of amplitude modulation (Kharkevich 1960).

Assume a carrier signal x is an oscillation with constant amplitude (c_0), frequency (ω_0) and initial phase (φ_0):

$$x = c_0 \cos(\omega_0 t + \varphi_0)$$

And let the modulation be $[1 + mf(t)]$, where m is the modulation *depth* defined from 0 to 1. Let $f(t)$ be the modulating function, defined so that $|f(t) \leq 1|$. The resulting effect is a *modulation product.*

If the modulated oscillation $[1 + mf(t)]$ modulates the carrier's amplitude, then we have *amplitude modulation*, i.e. **AM**:

$$x = [1 + mf(t)]\, c_0 \cos(\omega_0 t + \varphi_0)$$

Assume the simplest amplitude modulation (AM) function: $f(t) = cos(\omega_1 t)$.

$$\begin{aligned} x &= c_0 \left[1 + m \cos \omega_1 t\right] \cos(\omega_0 t + \varphi_0) \\ x &= c_0 \cos(\omega_0 t + \varphi_0) + c_0 m \cos \omega_1 t \cos(\omega_0 t + \varphi_0) \end{aligned}$$

If we apply the trig identity: $\cos\alpha \cos\beta = \frac{1}{2}\cos(\alpha + \beta) + \frac{1}{2}\cos(\alpha - \beta)$, then:

$$\begin{aligned} x &= c_0 \cos(\omega_0 t + \varphi_0) + \frac{m}{2} c_0 \left[\cos(\omega_1 t + \omega_0 t + \varphi_0) + \cos(\omega_1 t - \omega_0 t - \varphi_0)\right] \\ x &= c_0 \cos(\omega_0 t + \varphi_0) + \frac{m}{2} c_0 \left[\cos((\omega_1 + \omega_0) t + \varphi_0) + \cos((\omega_1 - \omega_0) t - \varphi_0)\right] \end{aligned}$$

Note that the *sidelobe frequencies* are $(\omega_1 + \omega_0)$ and $(\omega_1 - \omega_0)$ and that the carrier frequency is ω_0.

The process of amplitude modulation applies to Io's orbital and Jupiter's rotational frequencies in the following way. Jupiter's rotation period is 9.84 hours corresponding to a frequency of 2.44 rotations per day. Io's orbital period (and rotation

period) is 1.77 days, corresponding to a frequency of 0.56 rotations per day. If the dust originates from Io, and the dust flux is modulated by Jupiter, then the spectrum in frequency space would appear like the spectrum in Fig. 3.7, where the sidelobes at Jupiter's frequency at full and half-rotations are due to Jupiter's frequency modulating Io's frequency of orbital rotation. The frequency difference between Jupiter's rotational frequency and each of the sidelobes is the same frequency as Io's frequency of orbital rotation. In addition, if one or both of the original signals have broad spectra, then the spectrum of the modulation products will be broadened to the same extent (since the modulation process is linear). Therefore, the spread of Io's peak is repeated in the same way for the sidelobes of Jupiter's frequency peaks (full and half-rotation).

Modulation products appeared in about 20% of the 29 frequency-transformed Galileo orbits. Galileo's orbit E4 was the first orbit for which a hint of the amplitude modulation appeared, then in orbit G8, the signature was unmistakable. Other orbits for which one can clearly see the modulation products are: C10, E18, and G29 (see Appendix).

3.3.5 Spacecraft Motion in the Periodogram data

Several Galileo spacecraft orbital characteristics can be identified in the frequency-transformed data. For each orbit, the dust instrument receives more dust impacts while in the inner Jovian system than while in the outer Jovian system. In frequency space, the result is a peak at the origin.

The Doppler effect between Galileo and Io, as the "observer" and the "source" can be seen in frequency space as an asymmetry, or "smearing" of the Io and the Jupiter frequency peaks. If Galileo (velocity $v_{\rm Gal}$) and Io (velocity $v_{\rm Io}$) are moving *towards* each other, then the frequency shift is $\nu' = \nu * [(v + v_{\rm Gal})/(v - v_{\rm Io})]$ and if Galileo and Io are moving *away* from each other: $\nu' = \nu * [(v - v_{\rm Gal})/(v + v_{\rm Io})]$, where v is the reference velocity. The velocity of the dust streams, as our reference velocity, is an unknown, however Zook et al. (1996) determined that the dust streams must be faster than 200 $\rm km\,s^{-1}$. Therefore, I calculated several reference speeds, in order to determine Doppler shift trends. The results are that both the Io and Jupiter peaks can be smeared by Doppler shifts. The Doppler shifts for Io are to shorter periods, and the Doppler shifts for Jupiter are to longer periods.

Reference speed ($km\,s^{-1}$)	Original Period (hr)	Shifted Period (hr)
Io peak		
200	40.1	35.9
240	40.1	36.6
280	40.1	37.0
Jupiter peak		
200	9.4	10.7
240	9.4	10.5
280	9.4	10.4

3.3.6 Synthesizing the Periodogram

The main physical processes behind the frequency-transformed data can become clearer when one synthesizes data and compares the synthesized data to the real data. In the work presented in this subsection, E. Grün and I synthesize a spectrum, using typical periods from Galileo's dust impact rate data: 48 days for Galileo's orbit, 9 and 17 days for smaller data blocks, a Jupiter rotation and half rotation period, and an Io orbital rotational period, which show in the real data. The synthetic impact dataset with an added 1% amplitude of Gaussian noise is seen in Fig. 3.8. After transforming the synthesized data into frequency space with an FFT, frequency peaks appear with their modulation products, which are in the same locations as those in the 1996-1997 Galileo dust detector periodogram. The frequency-transformed synthetic spectrum can be seen in Fig. 3.9.

3.3.7 Errors on the Peaks in the Frequency-transformed Galileo Dust Data

I calculated an estimate for the errors on the peaks in the periodogram of Fig. 3.7 by fitting a Gaussian in a nonlinear least-squares Marquardt algorithm to each of the peaks. In order to apply a nonlinear least-squares algorithm to data, one must have: a fitting function, partial derivatives of the fitting function with respect to each of the free parameters, a first estimate of the free parameters, and weights for the data. The fitting function to determine the periodogram peak errors is:

$$y(x) = a_0 * \exp(-z^2/2) + a_3$$

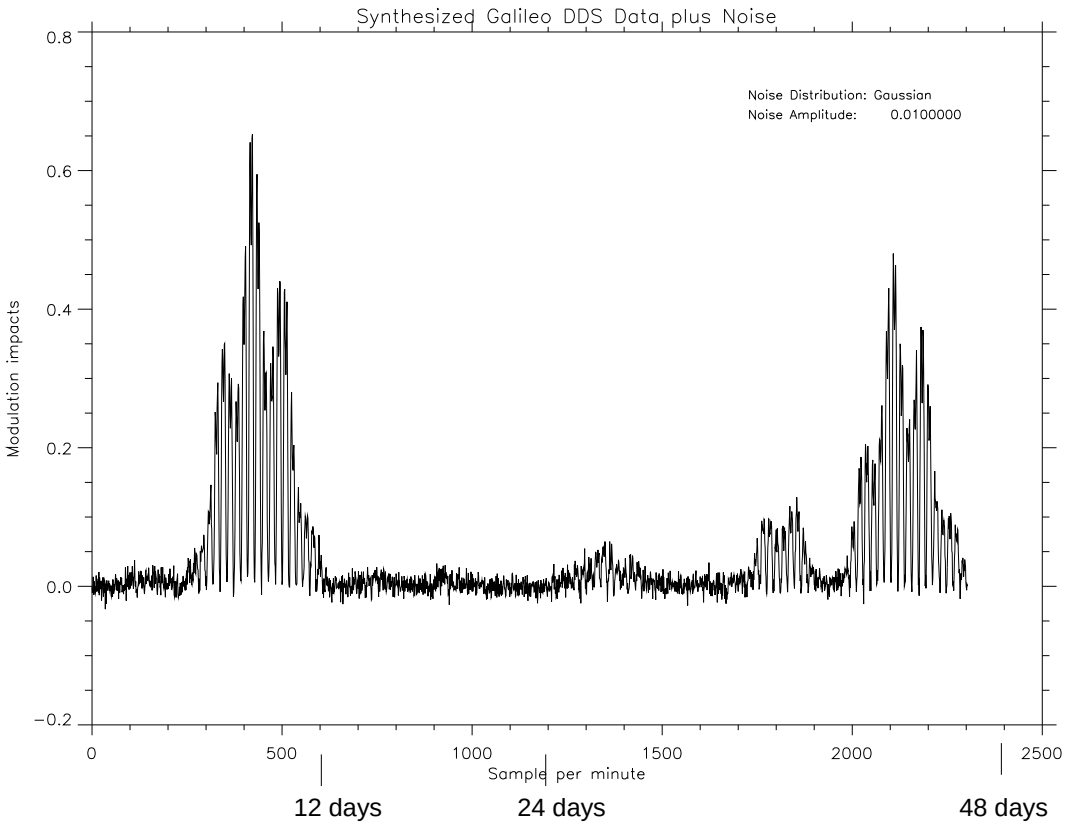

Figure 3.8 : A synthetic impact rate dataset, with added Gaussian noise, which includes the following periods: 48 days for Galileo's orbit, 9 and 17 days for smaller data blocks, a Jupiter rotation and half rotation period, and an Io rotation period.

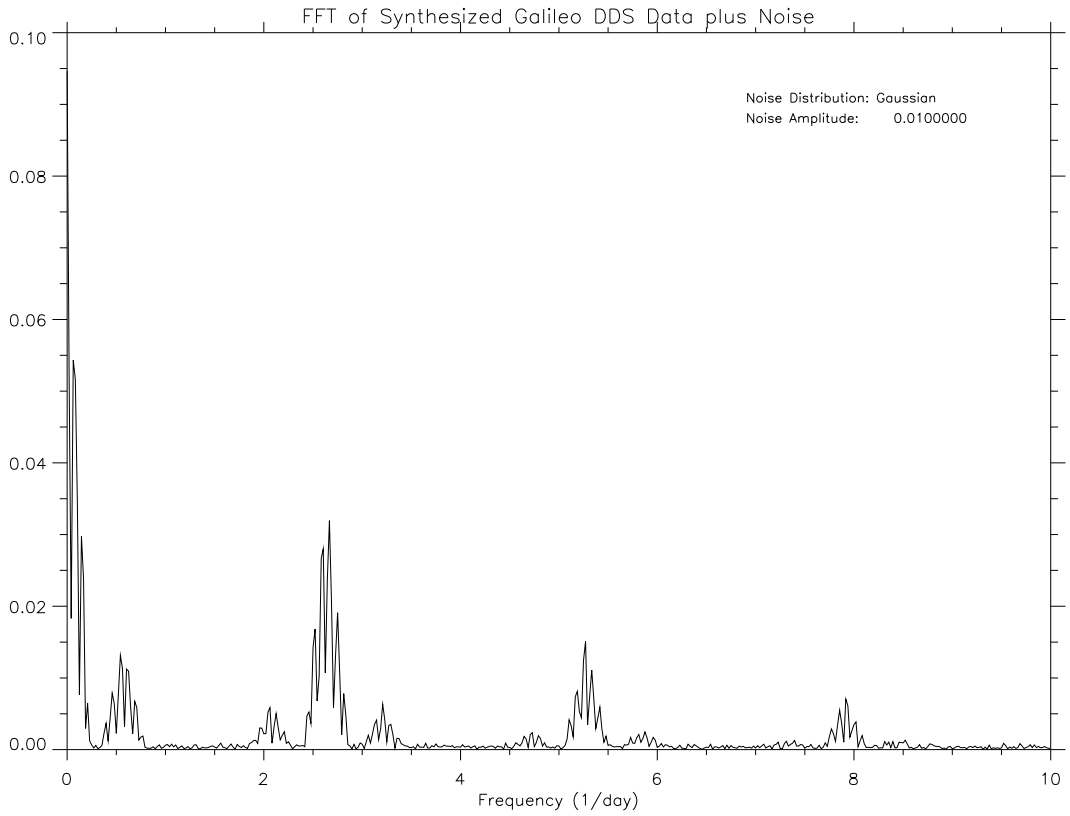

Figure 3.9 : An FFT of the synthetic rate dataset of Fig. 3.8. Galileo's motion (at the origin), Io's frequency of orbital rotation (0.56 d^{-1}), Jupiter's full frequency (2.4 d^{-1}) and half-frequency (4.8 d^{-1}) of rotation can be seen, as well as the Io-Jupiter amplitude modulation products (sidelobes around Jupiter's frequencies).

where the free parameters to be determined are: a_0, a_1, a_2, a_3, and $z = (x(i) - a_1)/a_2$, a_3 is the baseline, a_0 is the height, a_1 is the Gaussian midpoint, and a_2 is the half-width of the Gaussian distribution. The free parameter found for a_2 gives the error for the peaks in the periodogram. First estimates were determined by multiple smooths of the data and then determining a baseline, a midpoint, and a half-width of the Gaussian distribution. Weights for the data were calculated via a normalized variance. The one-sigma errors of each of the peaks is labelled on the periodogram, Fig. 3.7.

3.3.8 What is the amount of dust from Io?

The periodogram peaks in Fig. 3.7 can give us a rough lower bound of the fraction of dust from Io for the years 1996-1997, if we sum under the Io peak and the modulation sidelobes (primary and first harmonic). After applying a Newton-Cotes integration to determine the areas, I calculated that the fraction of dust from Io is 60% of the total mass rate. I determined the total mass rate using the following approximation. Assume for the Galileo dust instrument (DDS):

- a wedge-shaped emission pattern of dust stream particles detected by Galileo,
- a 2 g cm^{-3} particle density,
- a 10 nm particle radius,
- a 0.0235 m^2 detector sensitivity,
- an 11° to 45° wedge originating at Jupiter,
- a 30 R_J distance between Galileo and Jupiter,
- an average DDS rate of 0.2 to 30 particles min^{-1} from the larger 1996-1999 DDS impact rate dataset.

The 0.0235 m^2 detector sensitivity is the maximum of the total sensitive area of the DDS as a function of angle with the spacecraft spin axis averaged over one spin-revolution (Krüger et al. 1999). Then, the total mass rate is 10.0 g s^{-1} to 10.0 kg s^{-1}. Applying the 60% fraction of Io dust determined above, I find that the Io dust rate is 6.0 g s^{-1} to 6.0 kg s^{-1}. The remaining mass fraction could come from Io or elsewhere, but it has lost Io's frequency signature.

Chapter 4

MODELING

In this chapter, I provide descriptions of Jupiter's observed magnetosphere environment (magnetic field, plasma) and approximations to Jupiter's magnetosphere necessary for modeling the dust particle's charges and dynamics (subsequent chapters). I also provide model approximations for the dust particle's density and optical properties.

4.1 Jupiter's Magnetic Field

4.1.1 Observations of Jupiter's Magnetic Field

Jupiter has the largest magnetosphere in the solar system, a size large enough to encompass the Sun and its corona (Russell & Luhmann 1997). Jupiter's intrinsic magnetic field is generated from a dynamo in its electrically conducting, metallic hydrogen interior. The dipole moment is 1.55 10^{20} T m^3, which is almost 20 000 times that of the Earth's magnetic dipole moment. While Jupiter's "Earth-like" interaction with the solar wind is as a magnetized body carving out a cavity, nevertheless, large differences exist between Earth and Jupiter in their internal magnetospheric dynamics. The "Earth-like" interactions are: a giant magnetospheric cavity created from standing off the solar wind, a detached *bow shock* wave at the boundary of the cavity which is generated by the super-Alfvénic flow of the solar wind past Jupiter's magnetic field, a *magnetosheath* layer, a *magnetopause* surface at which the internal magnetospheric pressure balances that associated with the impinging solar wind, and a long cylindrical *magnetotail* extending far downstream behind the planet, stretching at least to Saturn's orbit. Jupiter's magnetospheric differences from Earth are: 1) a lower density (decreases $\propto 1/r^2$) of the solar wind at 5.2 AU (which is 4% of the solar wind's density at the Earth), 2) a rapid rotation of the planet and, 3) large amounts ($\sim 10^{28}$–10^{29} ions/sec^{-1} of S heavy ions) of plasma into Jupiter's magnetosphere supplied by Io (Cravens 1997, pg. 441). Figure 4.1 shows a schematic of

Jupiter's magnetosphere from Bagenal (1992), and Table 4.1 from Bagenal (1992) and Beatty et al. (1999) lists the current basic characteristics of Jupiter's magnetic field.

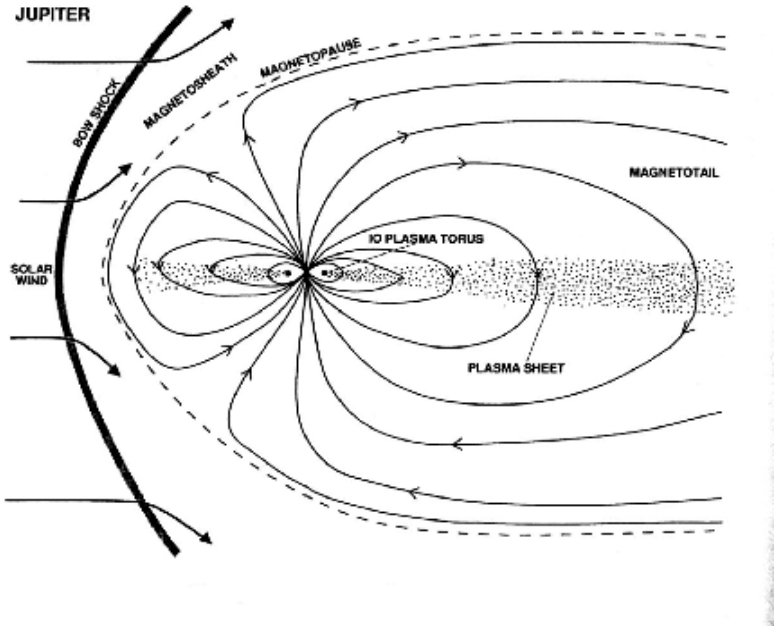

Figure 4.1 : A sketch of Jupiter's magnetosphere (Bagenal 1992).

Some secular variations exist in Jupiter's magnetic field. While the longitude 220° in System III, has scarcely changed in the last 25 years, the tilt angle has changed. The tilt angle has increased from about 9.3° to 9.8° (Russell et al. submitted). I use a dipole tilt of 9.6° for the modeling in this thesis. In addition, the magnitude of the dipole moment has increased about 1.5% during the years 1975 to 2000.

In this dissertation, I follow the notation of Dessler (1983, pg. 2), who divides the Jovian magnetosphere in terms of three principal regions. The *inner magnetosphere* is the region where sources internal to the planet dominate and this region is located approximately from the planet's surface to about 6 R_J, which is the orbital location of Io. I don't consider the inner magnetosphere here. The *middle magnetosphere* is the region where the effects of an azimuthal current sheet in the equatorial plane produce a significant perturbation of Jupiter's magnetic field, leading to a stretching of the magnetic field lines in the radial direction; this region is from about 6 R_J

Table 4.1 : Jupiter's Magnetic Field

Radius (km) R_J	71 398
Spin Period (h)	9.9
Magnetic Moment/M_{Earth}[a]	20 000
Surface Magnetic Field (Gauss)	
Dipole Equator (B_0)	4.28
Minimum	3.2
Maximum	14.3
Dipole Tilt & Sense[b]	-9.6°
Heliocentric Distance (AU)	5.2
Solar Wind Density (cm^{-3})	0.4
R_{CF}[c]	30 R_J
Size of Magnetosphere	50 – 100 R_J

[a] $M_{Earth} = 7.906 \times 10^{25}$ Gauss $cm^3 = 7.906 \times 10^{15}$ T m^3
[b] Earth has a magnetic field of opposite polarity to Jupiter.
[c] Magnetopause location using theory fromChapman & Ferraro. (1931).

to about 30 R_J. The *outer magnetosphere* is the region where tail current systems become important; here, the field exhibits large temporal and/or spatial variations in magnitude and direction in response to changes in the solar wind pressure. This region extends from about 30–50 R_J to the magnetopause boundary.

The Magnetodisk and Io

Pioneer and Voyager magnetic field data revealed a marked distortion in Jupiter's magnetic field at low latitude in Jupiter's equatorial regions that became known as the "magnetodisk". The magnetodisk's equatorial cross section is very different from that in the noon-midnight meridian. In addition, the magnetodisk wobbles with the planet's rotation period, due to the 9.6° offset between the spin and magnetic dipole axes (Dessler 1983).

Jupiter's distant magnetic field in magnitude and configuration is dominated by the current sheet (Dessler 1983, pg. 27). The magnetic field of the Jovian magne-

todisk is comparable in magnitude to the magnetic field of an internal origin at a radial distance of ~15 R_J. At 30 R_J, the field magnitude is approximately twice that of a 4.2 Gauss R_J^3 dipole, and is due almost entirely to the radial component of the sheet field.

The following observations offer some partial explanations. Io, with its ~42 hour rotation period, provides material from its volcanic plumes (up to ~460 km in height; (McEwen et al. 1998)). Material escapes Io at an approximate rate of 1 ton sec^{-1} (Spencer & Schneider 1996) via a multi-step process involving Io's atmosphere and the local plasma environment (Russell & Luhmann 1997, McGrath 1997). A combination of charge exchange, impact ionization and photoionization ionize the volcanic by-products, which are accelerated by Lorentz forces if they are charged high enough. That material, because it interacts with the field, is then swept up by Jupiter's magnetic field, which orbits with Jupiter's interior with a 9^h56^m rotation period. Physically, the planet's angular momentum is tapped electrodynamically by the newly ionized plasma (Bagenal 1992, pg. 312). You can see a schematic of this complex torus-plasma-magnetosphere system in Fig. 4.5.

The corotating plasma has a large effect on Jupiter's magnetosphere (Van Allen & Bagenal 1999, pg. 49). As the plasma corotates, the centrifugal forces enable the plasma to diffuse slowly outward against the confining forces of Jupiter's magnetic field. The 'iogenic' plasma in the middle magnetosphere is warm (tens of eV), extends to at least 40 R_J (<5 R_J thick), and is dominated by sulfur and oxygen ions (Bagenal 1992, pg. 312–313). This region, the magnetodisk, is where the centrifugal forces on the corotating plasma stretch out the magnetic field at the equator. In tens of days, the plasma is accelerated (instead of cooled) and heated, thereby inflating the middle and outer regions of the magnetosphere. The heating mechanism remains unknown. This 'hot' component of the plasma ($\sim$ 30 keV) beyond 10 R_J makes Jupiter's magnetosphere flatter at the poles. The particles then diffuse inward and gain additional energy from the magnetic field as they are recycled back towards the inner magnetosphere. Figure 4.5 illustrates these concepts.

4.1.2 Model of Jupiter's Magnetic Field

Data from the Pioneer spacecraft revealed Jupiter's magnetic field to be rich in multiple harmonics, therefore, a dipole approximation of Jupiter's magnetic field, while

the dust particle is traveling inside of Jupiter's magnetosphere, is inadequate for the field's significant complexities. I provide the background equations here for the harmonic expansion of a planet's internally-generated magnetic field, then I show tables of the coefficients derived by the Jupiter's magnetic field modelers. These coefficients, which approximate Jupiter's internal magnetic field, are used in the dust particle trajectory simulations in this thesis.

In Fig. 4.2, I illustrate the middle and outer magnetosphere and the locations where the multipole field and current sheet have their effect.

If one assumes, as Gauss did 150 years ago, that there are no significant sources ($\vec{J} = \vec{\nabla} \times \vec{B} = 0$), then the planetary magnetic field can be described as an expansion in spherical harmonics of the gradient of a scalar potential ((Dessler 1983, pg. 3–4); (Kivelson & Russell 1995, pg. 164–165)),

$$\vec{B} = -\vec{\nabla}\vec{V} = -\vec{\nabla}\left(\vec{V}^i + \vec{V}^e\right),$$

where $\vec{V}^i$ is the magnetic scalar potential due to sources inside Jupiter, and $\vec{V}^e$ is the scalar potential due to external sources. The expansion contains internal and external contributions to the field using associated Legendre polynomials. Connerney's O_4 and O_6 models (Connerney 1981, Connerney 1993) used in this thesis concatenate the internal and external contributions, and contain only the internal component, with the intent to emphasize the magnetosphere (< 20 R_J), and then augment it, in an engineering approach, with an explicit external model fit to observations.

Mathematically, the internal component of the magnetic field is expressed from the scalar potential, V, whose gradients are the three vector components of the magnetic field:

$$V(r,\theta,\phi) = a\sum_{n=0}^{\infty}\sum_{m=0}^{n}\left(\frac{a}{r}\right)^{n+1}\left(g_n^{m+1}\cos m\phi + h_n^{m+1}\sin m\phi\right)P_n^m(\cos\theta)$$

where θ and ϕ are Jupiter's co-latitude and east-longitude, a is the radius of Jupiter, and r is the distance from the center of Jupiter (Kivelson & Russell 1995, pg. 167). The index n is the degree of the Legendre expansion term and the index m is the order. The function $P_n^m(\cos\theta)$ is the associated Legendre function with Schmidt normalization:

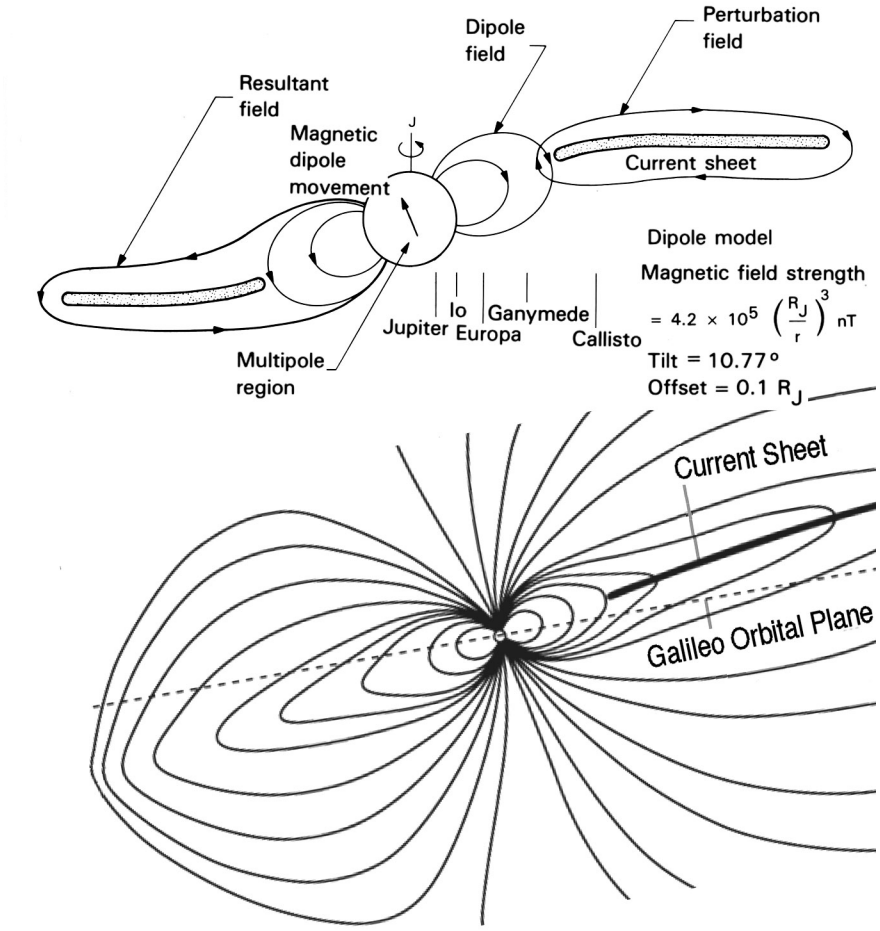

Figure 4.2 : A sketch of the middle and outer Jovian magnetosphere, showing where the multipole field dominates, and where the current sheet dominates. The upper figure from (Yeates et al. 1985, Fig 37) illustrates the different field components, and the lower figure from C. Russell's work (Russell et al. 1998) illustrates the total magnetic field, which is the sum of the multipole and current sheet components.

$$P_n^m(\cos\theta) = N_{nm}\left(1-\cos^2\theta\right)^{\frac{m}{2}}\frac{d^m P_n(\cos\theta)}{d(\cos\theta)^m}$$

so that $N_{nm} = 1$ when $m = 0$ and $N_{nm} = \left[\frac{2(n-m)!}{(n+m)!}\right]^{\frac{1}{2}}$, otherwise (Kivelson & Russell 1995). The coefficients g_n^m and h_n^m are called the *Gauss coefficients*, and are calculated to minimize the difference between the model field and observations. Tables 4.2 and 4.3 give the Gauss coefficients for Jupiter's magnetic field to degree and order 3, for Connerney's O_4 and O_6 models, respectively (Connerney 1981, Connerney 1993).

Table 4.2 : Jupiter O_4 Magnetic Field Model Gauss Coefficients

Coefficient	Degree (m)	Parameter (n)		
		1	2	3
	3			-0.231
g_n^m	2		0.513	0.168
	1	-0.664	-0.735	-0.0760
(g_n^0)	0	4.218	-0.203	0.233
	1	0.264	-0.469	-0.580
h_n^m	2		0.0880	0.487
	3			-0.294

In his O_6 model (Connerney 1993), Connerney constrains the harmonic expansion to the inner/middle magnetosphere by including two more sets of spacecraft observations than that used in his O_4 model, and by weighting the coefficients, so that the coefficient magnitudes decrease with increasing degree. The result are smaller quadrupole and octupole moments than his O_4 model.

The dipole term g_1^0 is the dominant term of the spherical harmonic expansion. This coefficient gives the size of the effective dipole moment along Jupiter's axis. We can combine the three degree-one terms to create a tilted dipole moment, $\vec{M}$, where the magnetic moment is given by (Kivelson & Russell 1995, pg. 168):

$$\vec{M} = a^3\sqrt{\left(g_1^{0\,2} + g_1^{1\,2} + h_1^{1\,2}\right)}$$

Table 4.3 : Jupiter O_6 Magnetic Field Model Gauss Coefficients

Coefficient	Degree (m)	Parameter (n)		
		1	2	3
	3			-0.180
g_n^m	2		0.487	0.198
	1	-0.659	-0.711	-0.155
(g_n^0)	0	4.242	-0.0218	0.0757
	1	0.241	-0.403	-0.388
h_n^m	2		0.0718	0.342
	3			-0.224

This expression can be visualized by understanding that g_1^1 is a dipole oriented along the x-axis, h_1^1 is a dipole oriented along the y-axis, and g_1^0 is a dipole oriented along the z-axis (Hamilton 2000). When $g_1^1 = h_1^1$, the dipole tilt angle can be calculated by summing the dipole moments oriented along the x and y axes with respect to the dipole moment oriented along the z-axis. This moment would have a pole at a latitude:

$$\lambda = \tan^{-1}\left[\frac{{g_1^0}^2}{\sqrt{\left({g_1^1}^2 + {h_1^1}^2\right)}}\right]$$

and at a longitude given by:

$$\Phi = \tan^{-1}\left(\frac{h_1^1}{g_1^1}\right)$$

The longitude is the azimuthal angle of the tilt of the dipole.

Model of Jupiter's Middle Magnetosphere and Magnetodisk

Jupiter's magnetic field is distorted at the equator ("magnetodisk") in the middle magnetosphere, as described previously, and seen in the sketch of Fig. 4.2, therefore this static magnetic field model should include a component to approximate the magnetodisk. I use Connerney et al.'s (1981) implementation.

A mathematical technique to approximate a planet's complex magnetic field configuration is to "hinge" a current sheet to a harmonic expansion (dipole, quadrupole, etc.) of the planet's internal field (Stern 1976, pg. 202). Connerney implements this approach for the octupole approximating Jupiter's internal field (Connerney 1981, Connerney 1993), with a current sheet to approximate the magnetodisk (Connerney et al. 1981).

Connerney's sheet implementation considers the magnetodisk as a perturbation to Jupiter's internal field. The perturbation field possesses a solenoidal geometry which can be modeled as a system of azimuthal equatorial currents (Dessler 1983, pg. 20). These currents can be directly compared to spacecraft measurements (Voyager 1). For example, if one applies Ampere's Law: $\int \vec{B} \bullet d\vec{L} = \mu_0 I_{enc}$ to a narrow circuit centered about the plane of symmetry of Jupiter's current sheet, the vertical components don't contribute to the integral (the vertical field components of the spacecraft measurements are negligible), however, the radial components *do* contribute, providing a useful field geometry with which to compare with Voyager 1 measurements. The radial component of the field is a local measure of the azimuthal current density.

Connerney computes the perturbation field using an annular current sheet of dimensions: inner radius a=5 R_J, outer radius a=50 R_J, half-thickness 2.5 R_J and current density $\mu_0 I/2 = 225$ A/km^2. At a radius of r=10 R_J, the radial magnetic field component above the sheet is about 50 nT.

4.2 Jupiter's Plasma

4.2.1 Observations of Jupiter's Plasma

As I described previously in section 4.1.1, a complex interaction exists between magnetospheric plasma "streaming" with Io, and Jupiter's ionosphere/magnetospheric coupling (Fig. 4.5). Io is the main source of plasma in the Jovian system.

From Voyager and pre-Voyager observations, the maximum densities of thermal ions in the Jovian magnetosphere are located near Io's orbit, where the densities are 3000 cm^{-3}(Yeates et al. 1985). The densities decrease rapidly with increasing radial distances to values of 1–10 cm^{-3} at radial distances of 10–20 R_J. Beyond these radial

distances, and in the plasma sheet, the ion densities range from 10^{-3}–1 cm^{-3}. Above or below the plasma sheet, the densities drop as low as 10^{-5}–10^{-4} cm^{-3}.

The Voyager instruments provide the following plasma temperatures (Yeates et al. 1985). The ion temperature have a rapid increase from about 1 eV at 5 R_J to 40 eV at 6 R_J. In the plasma torus at 6–8 R_J, the ion temperatures are 40–100 eV. At larger radial distances in the plasma sheet, the ion temperatures increase to 20–40 keV at 30–100 R_J. Electron temperatures for the plasma in Jupiter's magnetosphere could be best described in terms of a two-component plasma: "hot" and "cold" (Yeates et al. 1985). The cold electron temperatures are 10–100 eV in the radial distance range of 6–40 R_J. At the inner edge of the torus, the cold electron temperatures decrease sharply to about 0.5 eV, coincident with the ion temperatures. The characteristic temperature of the hot electrons is 1 eV, but it is generally less dense than the cold component, for example, it is 1 percent of the total number density at 8 R_J, increasing to 50 percent at 40 R_J.

4.2.2 Model of Jupiter's Plasma

To characterize Jupiter's plasma, I applied M. Horányi's plasma model, which is a fit to the Voyager 1 and 2 cold plasma measurements described in the previous section and by (Bagenal 1989). Horányi assumed a constant mixing ratio of 50% between single ionized oxygen and sulfur ions.

Figures 4.3 and 4.4 show the energy: electron temperatures and ion temperatures, and the density of the model Jupiter plasma data.

The Debye screening length is the distance that the Coulomb field of an arbitrary charge of the plasma is shielded:

$$\lambda_D = \sqrt{\frac{kT_e}{4\pi q_e^2 n_e}} = 7.4\sqrt{\frac{kT_e(eV)}{n_e(\mathrm{cm}^{-3})}} \quad \text{(m)}$$

The value of the Debye length indicates whether collective processes are important (Cravens 1997, pg. 35). If the mean separation between the dust particles in the plasma $d = L^{-\frac{1}{3}}$ (where L is the spatial density of the particles) is smaller than the Debye length, then neighboring charged dust particles are not shielded and isolated

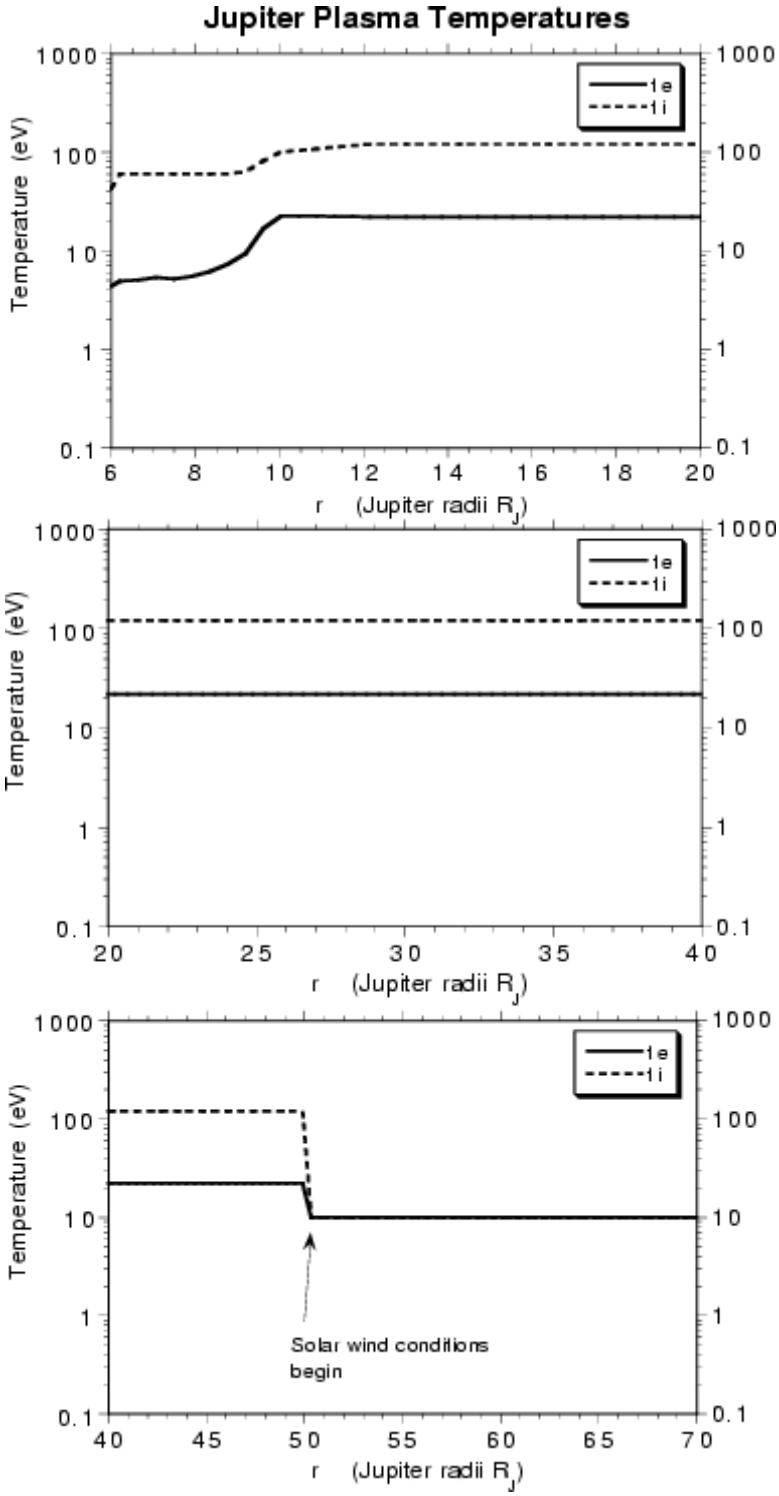

Figure 4.3 : Model plasma electron and ion temperatures as a function of distance from Jupiter.

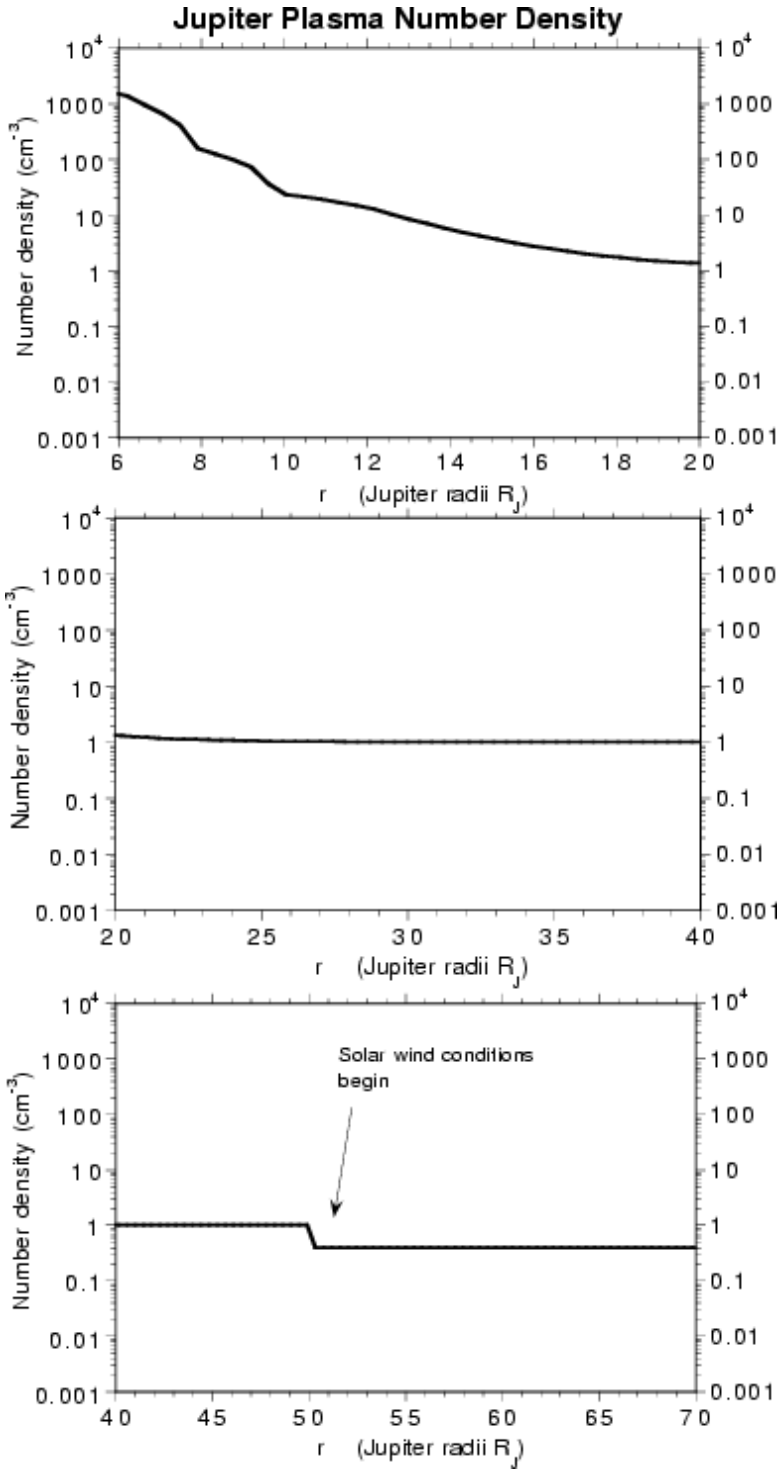

Figure 4.4 : Model plasma densities as a function of distance from Jupiter.

from each other, and they begin to act like a solid dielectric. To check that the inter-particle distances are larger than the Debye shielding length, I calculate some Debye lengths for this model plasma, and I show, in Table 4.4, some plasma representative numbers.

Table 4.4 : Jupiter Plasma Representative Numbers

Location (R_J)	T_e (eV)	T_i (eV)	Density (cm^{-3})	Debye Length (cm)
6.2	4.9	60	1300	60
8	5.4	60	156	200
10	22.5	100	23.2	1000
15	22.0	120	3.6	2400
20	22.0	120	1.3	4000
30	22.0	120	1.0	4500

Model of Jupiter's Plasma Density Distribution and Scale Height

Jupiter plasma observations showed that the strong centrifugal forces tended to confine the plasma to the centrifugal equator (Bagenal 1992, pg. 311). Modeling the plasma density distribution and scale height for this thesis work proceeded in the following way. To first approximation, the plasma density decreases exponentially with distance from the centrifugal equator: $n(z) = n_0 \exp(-(z/H)^2)$, where the scale height H is given by $H = (2kT_i/3m_i\Omega^2)^{1/2}$ for a Jupiter spin rate of Ω, ions of mass m_i, and temperature T_i ((Bagenal 1992, pg. 311); (Cravens 1997, pg. 448, Eqn. 8.125). Therefore, the warmer ions in the outer region of the torus have a large scale height and are more spread out along the field than the cold ions inside of Io's orbit.

Plasma β

The *plasma* β, defined by (Cravens 1997, pg. 110):

$$\begin{aligned} &\text{(gas pressure) / (plasma pressure)} \\ &(n_e k_B (T_e + T_i)) \;/\; (B^2/2\mu_0) \\ &= \beta \end{aligned}$$

gives the relative importance of the gas pressure to the magnetic field as the restoring force to any disturbance (Scott 1994, pg. 20), i.e., plasma β can describe how strongly the plasma is magnetized.

In Horányi's plasma model, the plasma β scales the plasma velocity to match boundary conditions for the electric field in the magnetosphere, inside and outside of the magnetosphere. In the magnetosphere, the electric field is determined by corotation. Outside of the magnetosphere, the electric field is determined by the convection from the solar wind. Therefore, the β is used to reduce the plasma flow velocity inside of the magnetosphere, decreasing the velocity as the radius increases. So then, at the magnetosphere boundary, r=50 R_J, the plasma flow velocity is zero. See the section titled: "Derivation of the Magnetosphere Boundary" in the Appendix for more information. The flow velocity is calculated using this β, the radius distance r, and Jupiter's rotation Ω: $v_{\text{plasma}} = (\Omega \times r)\,\beta$.

In general, a plasma is termed "cold" if $\beta << 1$, and termed "warm" if $\beta \geq 1$ (Kivelson & Russell 1995, pg. 50). If $\beta >> 1$, then the magnetic force has a negligible effect on the dynamics, but the magnetic field is still advected by the flow (this situation is called: "MHD kinematics"). In the Jupiter environment, the plasma β can be implemented in other ways to aid in characterizing the magnetosphere, which would useful if one wants to add a magnetopause to the magnetospheric model. Cravens (1997) demonstrates examples of this.

4.3 Torus-Magnetosphere Coupling

The elements of the torus-magnetosphere coupling is often studied separately, however, the charging and dynamics model in this thesis implements several elements from magnetohydrodynamics, such as a magnetosphere boundary and convection and corotation electric fields (see section 6.1 and the Appendices), therefore, I place a sketch here (Bagenal 1989, pg. 197), which illustrates some of the coupled interactions in the Jovian magnetosphere. The model of this thesis implements the magnetosphere boundary and convection and corotation electric fields, however, the more complex couplings shown in the schematic are not implemented and these could be directions for future work to improve the model.

The figure schematic shows that Jupiter's magnetosphere is coupled to Jupiter via currents that close the loop in the ionosphere. Some particles are accelerated to high energies to the outer magnetosphere. Corotation in the figure is implied by the Ω term, the magnetic force (or stress) is implied by $\vec{J} \times \vec{B}$, which is balanced by pressure gradient forces ∇P from the hot plasma and centrifugal stresses, exerted by the warm plasma.

4.4 Model of Dust Particle Densities

Divine et al. (1986) published a thorough analysis and model of comet Halley's dust and gas environment. The parameters listed in that work are still used today in the dust charging and dynamics research by M. Horányi and his colleagues during the last decade. Divine et al.'s (1986) work surveyed the diverse evidence of particle densities from lunar microcraters, meteor stream studies, and collected stratospheric particles, and they proposed an equation of the form:

$$\rho = \rho_0 - \sigma_0 \left(\frac{a}{a + a_2} \right)$$

with the parameter values: $\rho_0 = 3$ g/cm^3, $\sigma_0 = 2.2$ g/cm^3, and $a_2 = 2$ μm. The resulting densities range from 3.0 to 0.8 g/cm^3, as the particle size varies from the smallest to the largest in the distributions. Some sizes and densities calculated using the above equation can be seen in the following table (Table 4.5).

In my simulations, I started with these Divine's 'cometary' densities, however, for our small particle-sizes (0.002 μm–0.01 μm), the densities are too high. Lide (1998, pg. 4-144) lists the density of solid sulfur at 2 g/cm^3. Therefore, in my simulations, I used density values 1.35–2.0 g/cm^3.

4.5 Model of Dust Particle Optical Properties

An approximation of the dust particle's optical properties is necessary in order to apply the radiation pressure force for the dust particle's dynamics. Here I describe the main parameter: Q_{pr}. The cross-sectional area for the interaction of a small grain with electromagnetic radiation is $Q\pi a^2$, where the efficiency factor, Q, depends on

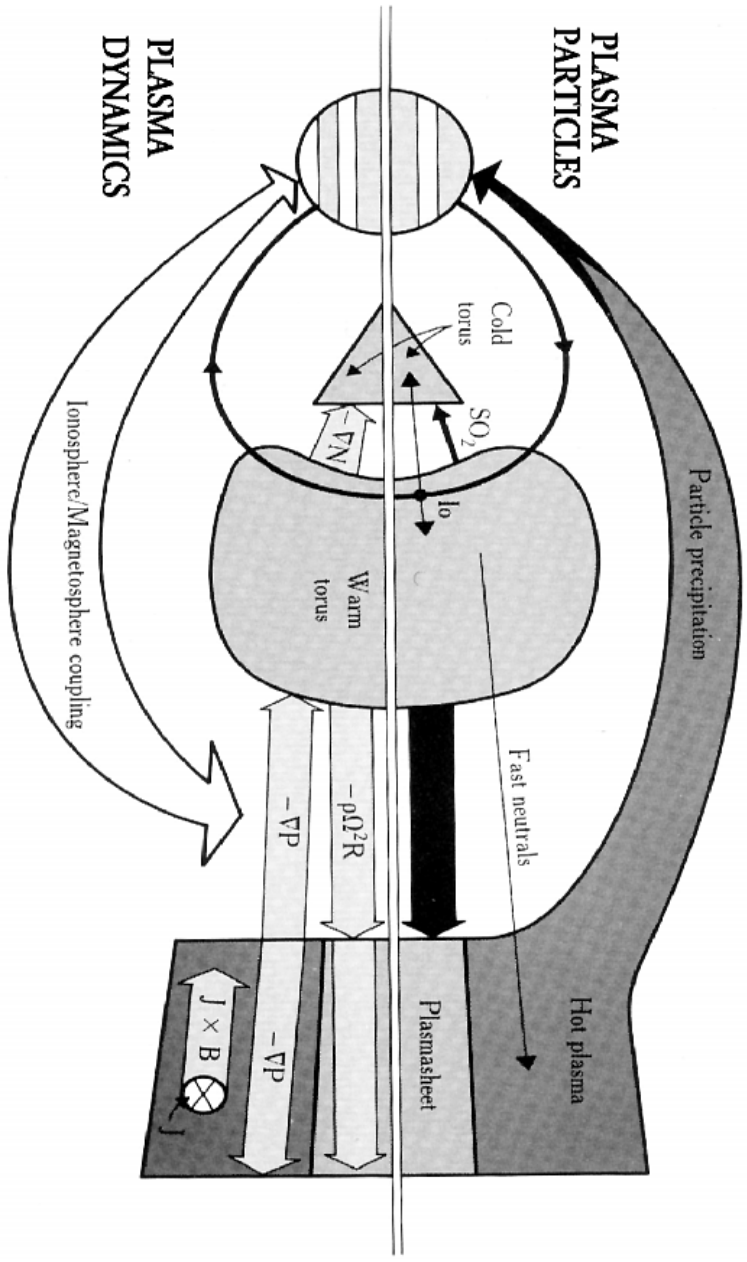

Figure 4.5 : A sketch of the coupling between the torus, magnetosphere and ionosphere from (Bagenal 1989). See text.

Table 4.5 : Dust Particle Sizes and Densities from Divine et al., 1986

Radius (cm)	Density (g/cm^3)
0.	3.
2.0e-7 (0.002 μm)	2.998
5.0e-7 (0.005 μm)	2.995
9.0e-7 (0.009 μm)	2.991
1.1e-6 (0.011 μm)	2.989
2.0e-6 (0.02 μm)	2.98
5.0e-6 (0.05 μm)	2.95
1.0e-5	2.9
1.44e-5	2.85
1.77e-5	2.82
2.04e-5	2.8
2.98e-5	2.72
4.51e-5	2.59
6.63e-5	2.45
1.02e-4	2.26
2.36e-4	1.8
5.57e-4	1.38
1.30e-3	1.09
2.94e-3	0.94
6.51e-3	0.86
1.42e-2	0.83
3.08e-2	0.81
6.66e-2	0.8
1.44e-1	0.8
3.1e-1	0.8
6.68e-1	0.8
1.0	0.8

the nature of the grain (its refractive index, size, etc.), and the wavelength of the radiation involved in the interaction (Evans 1994). Furthermore, we have to specify whether the process is extinction, scattering, or absorption. For momentum effects from an electromagnetic wave, the absorption cross-section plays no role, however the extinction and scattering cross-sections do play a role (Evans 1994). The dust particle's optical properties are manifested via Q_{pr}, which affects the particle's dynamics through the radiation pressure force.

The efficiency factor Q_{pr} is defined as: $Q_{pr} = Q_{ext} - Q_{sca} \langle \cos\theta \rangle$.

Many investigators characterize the particle's optical properties via the parameter β, which is the ratio of the radiation pressure force to the gravitational force:

$$\beta = \frac{F_r}{F_g} = \left(\frac{3L}{16\pi GMc}\right)\left(\frac{Q_{pr}}{\rho a}\right) = 5.7 \times 10^{-5}\left(\frac{Q_{pr}}{\rho a}\right)$$

where Q_{pr} is averaged over the solar spectrum, a is a spherical particle's radius, and ρ is the particle's density, in cgs units. For this work, a Q_{pr} value for the dust particle is calculated based on the particle's size and following the curve in Burns et al.'s classic paper (Burns et al. 1979). Figure 4.6 from that paper shows the relative radiation pressure force β as a function of particle size for several materials that are relevant to dust studies.

The Sun radiates nearly all of its energy in a narrow wave band around 0.6 μm so that the transition from geometric optics to Rayleigh scattering takes place in the micrometer size range (Gustafson 1993). The linear slope in Fig 4.6 demonstrates that for any particle material greater than a few μms in size, geometrical optics holds, thus Q_{pr} is roughly constant, independent of particle size (Burns et al. 1979). The important interactions are for sizes comparable to the characteristic radiation wavelength divided by 2π. The metals suffer a large radiation pressure because they backscatter radiation, whereas the dielectrics are strong forward-scatterers. Graphite feels a relatively large radiation force because it absorbs radiation over a wide wavelength range, very much like a metal (Burns et al. 1979).

The particle's charging and dynamics modeling and results are described in the next chapters.

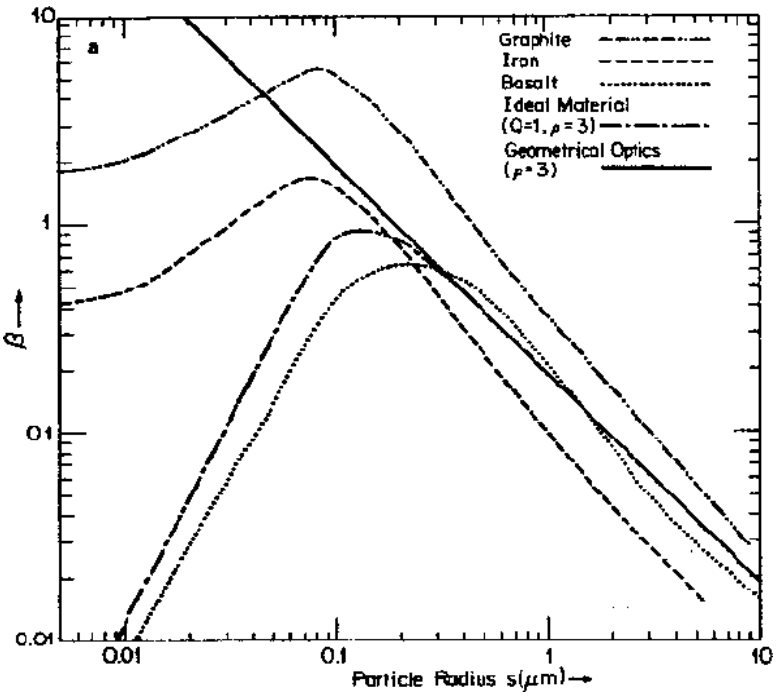

Figure 4.6 : A log-log plot of the ratio β as a function of particle size for some cosmically significant materials and two comparison standards from (Burns et al. 1979).

Chapter 5

CHARGING

In this chapter, I provide details of the charging processes model and charging results. I show that the charging time to reach equilibrium potential is usually a significant fraction of the dust particle's traveling time in Jupiter's magnetosphere, and I show the values of the equilibrium potential in selected regions inside and outside of Jupiter's magnetosphere. The dominant charging currents in Jupiter's magnetosphere are also illustrated in this chapter, and I demonstrate that the secondary electron emission current has a large role in the region of the solar wind.

5.1 Charging Processes

Now I describe the model of the charging mechanisms implemented for the dust stream particles as they travel in their trajectories.

5.1.1 Early Work

In early work, Spitzer (1962) considered the interaction between a spherical grain and a plasma as a simple problem of particle collection in a Coulomb potential. He neglected the photoelectron effect, and he derived the relationship between potential φ and temperature of the plasma T (K):

$$\varphi = -2.15 \times 10^{-4} \times T(\mathrm{K})$$

In a Maxwellian plasma with electron and ion energy distributions at the same temperature, the velocity and therefore, the charging current of electrons, is higher, so that grains are charged negatively. As a result, ions are attracted and electrons are repelled. When the electrons are repelled, the ion current is increased. The two currents become equal when φ is equal to the above expression.

If the surface potential of the grain is positive, then the situation is reversed. Because the ion flux is a factor:

$$\sqrt{\frac{m_e}{m_i}} = 0.023\sqrt{M\ (\text{a.m.u.})}$$

smaller than the electron flux, where M is the atomic mass number of the ion species, then, in most cases, the electron flux dominates the ion flux and the dust grain is charged up negatively to roughly the potential:

$$\varphi = \frac{kT_e}{q_e} = kT_e\,(\text{eV}) \quad (\text{V}).$$

Horányi (1996*a*) expresses the above as: $\varphi = -\beta k_B T/q_e$ with the appropriate plasma β for different plasmas : β = 2.5 (H^+), 3.6 (O^+), and 3.9 (S^+).

For an isolated dust grain, the surface potential $\varphi = Q/a$, which is the net charge. The number of missing electrons is then:

$$Q \approx 700 \quad \varphi(V) \quad \text{a}(\mu m).$$

For this case, φ is the surface potential in volts, and a is the radius of the grain in microns. For example, in a 1 eV hydrogen plasma, φ = -2.5V, independent of a, therefore, a 1 μm-radius particle will collect approximately 1800 extra electrons.

5.1.2 Charging Equation

The following description is M. Horányi's currents considered for the charging of the Jovian dust stream particles.

The charge of a particle varies with time according to

$$\frac{dQ}{dt} = \sum_k I_k = I_{\text{e,i,moving}} + I_{\text{sec}} + I_\nu$$

where k ranges over the different charging processes, and the current of the kth charging process is denoted as I_k (Kimura & Mann 1998). The other variables on the right side: $I_{\text{e,i,moving}}$ = electron and ion currents to a moving or stationary grain, I_{sec} = secondary electron currents, and I_ν = photoelectron currents.

5.1.3 Electron and Ion Capture

The electron and ion capture currents are (Goertz 1989):

$$I_{e,i} = 4\pi a^2 n_{e,i} \sqrt{\left(\frac{kT_{e,i}}{2\pi m_{e,i}}\right)} \begin{cases} \exp\left(-\psi_{i,e}\right) & \psi_{i,e} > 0 \\ 1 - \psi_{i,e} & \psi_{i,e} < 0 \end{cases}$$

where,

$$\psi_{i,e} = \mp \frac{q_e \varphi}{kT_{e,i}} \quad ,$$

and the $\mp$ the signs correspond to electrons and ions: the e, i indices indicate electrons and ions, respectively.

Ion currents generated due to a moving grain is a more general scenario for the ion capture, which reduces to the above expression under special circumstances. Therefore, I cover the more general expression next.

5.1.4 Ion Currents to a Moving Grain

If the dust particles are not at rest in the plasma, and the dust-to-plasma relative velocities are comparable to, or exceed, the ion thermal velocities (a situation which often arises when the grain is in the solar wind), then the ion currents to the moving grain ("modified proton currents") must be added to the other currents. The I_{moving} current has two different expressions, each depending whether the grain potential is positive or negative.

For a negative grain potential, the modified proton current is:

$$I_{\text{moving}} = \frac{4\pi a^2 n_i \sqrt{\left(\frac{kT_i}{2\pi m_i}\right)}}{2} \left[\left(M^2 + \frac{1}{2} - \psi_i\right)\sqrt{\frac{\pi}{M}}\text{erf}\left(M\right) + M^2\right]$$

where M = the ratio of the dust-to-plasma relative velocity w over the ion thermal speed (M = "Mach" number, (Horányi et al. 1988)), and $\text{erf}(x)$ is the *error function*:

$$M = \frac{w}{\sqrt{\frac{2kT_i}{m_i}}} \quad \text{erf}(x) = \frac{2}{\pi}\int_0^x \exp\left(-y^2\right) dy$$

For a positive grain potential, the modified proton current is:

$$I_{moving} = \frac{4\pi a^2 n_i \sqrt{\left(\frac{kT_i}{2\pi m_i}\right)}}{2} \left\{ \begin{array}{l} \left(M^2 + \frac{1}{2} - \psi_i\right) \sqrt{\frac{\pi}{M}} \left[\mathrm{erf}\left(\mathrm{M} + \sqrt{\psi_\mathrm{i}}\right) + \mathrm{erf}\left(\mathrm{M} - \sqrt{\psi_\mathrm{i}}\right)\right] \\ + \left(\sqrt{\frac{\psi_i}{M}} + 1\right) \exp\left[-\left(M - \sqrt{\psi_i}\right)^2\right] \\ - \left(\sqrt{\frac{\psi_i}{M}} - 1\right) \exp\left[-\left(M + \sqrt{\psi_i}\right)^2\right] \end{array} \right\}$$

In the limit of $M \rightarrow 0$, the above expressions are identical to the ion capture expression.

5.1.5 Photoelectron emission

The absorption of solar UV radiation releases photoelectrons, and hence, constitutes a positive charging current (Horányi et al. 1988). Its magnitude depends on the material properties of the grain, i.e. its photoemission efficiency, and on the grain's surface potential, which may, if positive, recapture a fraction of the photoelectrons. The spectrum of the photoelectrons released is often assumed to be a Maxwellian distribution with a temperature $\mathrm{T_{photo}}$, which corresponds to an energy $kT \sim 2$ eV. The photoelectric current is (Horányi et al. 1988, Eqn. 10):

$$I_\nu = \left\{ \begin{array}{ll} \pi a q_e f_1 & U < 0 \\ \pi a q_e f_1 \exp\left(-\frac{q_e U}{kT}\right) & U > 0 \end{array} \right.$$

Here, a is the particle radius, q_e is the charge on the electron, kT is the average energy of the photoelectrons and, $f_1 \approx 2.5 \times 10^{10} \chi s^{-1}$, is the flux of photoelectron emission at 1 AU with the "photoelectron efficiency factor" χ spanning the range: $\chi \approx 1.0$ for conducting magnetite (metals) grains, and $\chi \approx 0.1$ for dielectric olivine particles.

The photoelectric current described here follows from Horányi et al. (1988), which, in turn, refers to: Feuerbacher et al. (1973). They carried out calculations for grains of high (material: Al_2O_3) and low (material: C) photoelectric yields, taking into account the material's full frequency dependence and the energy distribution of the emitted photoelectrons.

The photoelectric threshold theoretically and observationally increases with decreasing particle radii (Kimura & Mann 1998). The smallest dust grains can be characterized by the physical properties of *solid spherical* particles, which is the particle geometry I used for this modeling work.

5.1.6 Secondary Electron Emission

The effect of electrons or ions with high energies bombarding the dust grain can lead to an ionization of the grain material and ejection of electrons from the grain. This process is called *secondary electron emission.* This current has the largest effect on the charging of the dust particles, and is, in turn, highly sensitive to the dust particle's material properties. No systematic approach exists yet to determine the dust particle's secondary electron material properties, therefore, one must be aware of the previous researcher's results and use those values as starting points. Because this current has a large effect on the dust grain's potential, I spend some time summarizing previous laboratory results in this section. The charging results, described later, will refer often to the dust particle's material properties used in the charging calculations, especially that by the secondary electron emission current calculations.

The three processes that can occur during secondary electron emission: 1) reflection, 2) backscattering and 3) true secondary emission are usually treated as distinct secondary electron yield processes by both *electron* impacts from solid particles as well as by *ion* impacts (Whipple 1981).

The flux of secondary electrons depends on the energy of the plasma electrons/ions E and on the grain's surface potential. The number of secondary electrons – the *yield* – depends, also, on the material properties of the charged grains, which is characterized by the secondary electron emission yield parameter δ. If the secondary electron yield is greater than 1, then positive dust charging occurs. For some materials, the yield is greater than 1 for $kT_e = 50$ eV, and for other materials, the yield is greater than 1 at $kT_e = 1000$ eV and higher. The yield also increases with decreasing grain size. For example, the maximum secondary electron emission yield from ions/electrons impacting onto 0.01 μm-sized particles, for both conductors and insulators, is about 3.5 times higher than onto 1 μm–sized particles (Chow et al. 1993).

Secondary Electron Emission - Electron impact

Sternglass published an expression for the secondary current by electron impact using the yield function (Sternglass 1954):

$$\delta(E) = 7.4\delta_m \left(\frac{E}{E_m}\right) \exp\left[-2\sqrt{\left(\frac{E}{E_m}\right)}\right]$$

where E_m is a characteristic energy, at which the release of a secondary electron reaches a maximum (Goertz 1989).

This extensively-used formula for the secondary emission yield, which uses semi-infinite slabs of material, approximates the theoretical derivations of Bruining and Jonker from the 1950s. For small spherical grains (not a planar slab), secondary electrons are not limited to the point of incidence of the primary electron. Instead, it is possible for secondary electrons to exit from all points of the dust grain surface, thus increasing the yield over that determined by the Sternglass formula (Chow et al. 1993). Sometimes this effect is referred to as the *small-particle approximation.* For this reason, I double the secondary electron emission yield when the dust particle is $\leq 0.1\mu$m.

Meyer-Vernet (1982) showed that the charge on a grain is not always unique: the equilibrium potential may have multiple roots, which is important to note, especially for plasma environment with high plasma temperatures or densities. Secondary-electron yield of electron impact onto other grain materials, such as onto ice grains, can influence that type of grain's charging, also.

In Table 5.1, I combine secondary electron emission values from several researchers. I show representative secondary electron emission values for maximum yield δ_m and energy at maximum yield E_m from Draine & Salpeter's (1979, Table 5) work, from Suszcynsky et al.'s (1993, Table 1) work, from Whipple's (1981, Table 2) work, and from M. Horányi and A. Heck's work (Horányi et al. 1997, Heck 1999).

Good laboratory data exists for secondary electron emission yields by *electron impact.* In Chow et al.'s (1993) work, they showed laboratory data for the number of emitted electrons per incident electron for different-sized conducting and insulating grains as a function of primary electron energy, in addition to the "Jonker yield" for semi-infinite slabs. At low primary energies, the smaller grains have higher yields for both insulators and conductors because, within these smaller grains, excited secondary electrons have shorter distances to travel to reach the surface. However, as the primary energy increases, the yield curves for different size grains may cross and larger grains may have higher yields than the smaller grains (for example, in their graph, compare 0.01 and 0.05 μm-sized conducting grains in the range 1750 to 4000 eV). Note that these cross-overs occur at high energies ($\sim$1000 eV for the smallest grains). Smaller grains, both conductors and insulators, have higher yields, generally,

Table 5.1 : Grain Material Secondary Electron Emission Parameters

Material	**density (g/cm^3)**	δ_m	E_m **(eV)**
Draine et al. (Draine & Salpeter 1979)			
Graphite	2.26	1.0	250
SiO_x	2.65	2.9	420
Mica	2.8	2.4	340
Fe	7.86	1.3	400
Al	2.70	0.95	300
MgO	3.58	23.0	1200
Lunar dust	3.2	∼1.5	500
Suszcynsky et al. (Suszcynsky et al. 1993)			
H_2O		3.2	406
CO_2		1.2	467
NH_3		2.2	362
CH_3OH		1.6	235
Whipple (Whipple 1981)			
Al		0.97	300
Al_2O_3		1.5–1.9	350–1300
MgO		4.0	400
SiO_2		2.4	400
Teflon		3.0	300
Kapton		2.1	150
Mg		.92	250
Horányi, Heck (Horányi et al. 1997, Heck 1999)			
SO_x		3.0	300

because the excited secondary electrons have shorter distances to travel to reach the grain's surface.

Recently, Horányi et al. (1998) published laboratory data for secondary electron emission yields for impacting electrons onto Apollo 17 lunar dust. This data is particularly valuable for being among the few data available of secondary electron emission of low-energy electron impacts.

Secondary Electron Emission - Ion impact

Horányi et al. (1988) published expressions for the secondary current by ion impact, using the yield function:

$$\delta(E) = 2\delta_m \left(\frac{E}{E_m}\right) \frac{\sqrt{\left(\frac{E}{E_m}\right)}}{\left(\frac{1+E}{E_m}\right)}$$

Due to lack of laboratory data, Horányi, Juhász and and their co-workers (Horányi et al. 1988, Horányi 1990, Horányi 1996*a*, Juhász & Horányi 1997, Juhász & Horányi 1999) use $\delta_m = 4.3$ and $E_m = 40$ keV in their simulations for the relevant material-dependent parameters.

5.2 Equilibrium Potential and Charging Times

Dust equilibrium potential is reached when the sum of all of the charging currents is zero. The dominant electron capture from the plasma leads to negative charges, and the other charging processes: ion capture, secondary electron emission and photoelectron emission, facilitate positive currents. Secondary electron and photoelectron emission charging processes are highly material dependent. If the charged dust particle is located in a high-energy or high density region of a planetary magnetosphere, such as near Io's orbit in the Jovian magnetosphere, or in Earth geosynchronous orbit or in a planetary magnetosphere's plasma sheet, then plasma particles may be charged positively or negatively.

The time to acquire the equilibrium charge may be longer than the flight trajectory time of the particle, therefore, it's worthwhile to investigate equilibrium charging

times. First, I describe the method, then I give my results for equilibrium charging in Jupiter's magnetosphere.

The theoretical charging time to reach equilibrium potential is:

$$\tau_{eq} = \left|\frac{Q}{I}\right| = \left|\frac{4\pi\varepsilon_0 a\phi}{I}\right|$$

where ε_0 is the permittivity of free space, φ is the particle's charge potential, and a is the particle's radius. The denominator is the thermal electron and ion flux bombarding the particle. Generally the charging time increases with decreasing particle radii a, approximately inversely proportional: $\tau_{eq} \propto a^{-1}$.

In my equilibrium potential calculations, I calculate an empirical charging time

$$\tau = \frac{(-t_{\text{eps}}\ \Delta t)}{\ln(\epsilon)} \quad \text{(sec)}$$

where t_{eps} is the time for a particle's potential to reach an equilibrium, i.e., the present potential does not change from the previous value by more than a minuscule amount, ϵ, which is the accuracy reached for unchanging potentials. A typical ϵ=10^{-6}. The variable Δt is the time increment for each potential calculation.

If I plot the potential values, then they eventually reach a unchanging value, seen as a flat plateau. The next figure, Fig. 5.1, shows an example of a potential reaching equilibrium.

I calculated the charging time τ for different regions in Jupiter's magnetosphere, defined by the plasma parameters described in the previous chapter, by fixing a particle in one location, and then noting the time to reach equilibrium during a 10-hour time duration. If the particle didn't reach equilibrium in that time, then I stopped the test. In this study, I used the following set of particle material properties and secondary electron and photoemission parameters for a 10 nm-sized particle.

δ_m=3.0, E_m=300 eV, χ=1,
a=0.01μm, ρ=2.0g/cm^3,
T_{photo}=2.0 eV

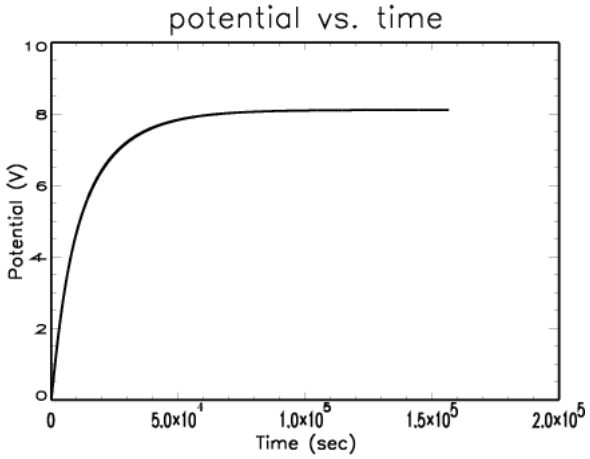

Figure 5.1 : The empirical method of calculating charging times: A particle has reached equilibrium potential when the charge reaches a plateau and no longer changes within an ϵ accuracy.

Dust Charging Time in Jupiter's Magnetosphere

Location (R_J)	**τ (hr)**	**Notes**
3–6	> 10	Far from equilibrium
6–10	1–2 hr (τ increasing linearly w/radius from Jupiter)	In equilibrium
10–12	1/2–1 hr (τ increasing linearly w/radius from Jupiter)	In equilibrium
12–20	1–2 hr (τ increasing linearly w/radius from Jupiter)	Nearly equilibrium
20–30	2–3 hr (τ increasing linearly w/radius from Jupiter)	In equilibrium
30–40	3–4 hr (τ increasing linearly)	Nearly equilibrium
40–50	4–5 hr (τ increasing linearly w/radius from Jupiter)	In equilibrium
>50	$\geq$10	Doesn't reach equilibrium

In summary, the dust particle within Jupiter's magnetosphere needed 1–5 hours to reach equilibrium potential. In the plasma conditions of the solar wind, the dust

particle never reached equilibrium in the 10-hour time span. Using these same set of particle material properties and secondary electron and photoemission parameters for a 10 nm-sized particle, I show the dust particle's equilibrium potential in Fig. 5.2. Except for the region inside of 8 R_J, the particle has a potential of about +6 V everywhere. In the figure, 5.2, I show two equilibrium potentials: 1) the theoretical equilibrium potential from the charging equation when $dQ/dt = 0$ and, 2) the potential at the end of the empirical charging time.

5.3 Dominant Currents in Jupiter's Magnetosphere

Using the charging parameters listed in section 5.2, and given the charging equations in this chapter, I calculated the currents inside of Jupiter's magnetosphere and outside of Jupiter's magnetosphere. I display these currents in Figs. 5.3 and 5.4. Note that these currents are valid for the *equilibrium* potentials seen in Fig. 5.2. The dominant currents inside of the Jovian magnetosphere are the electron collection current and the secondary electron emission current.

5.4 Currents at Locations of the Cassini-Galileo Joint Measurements

On December 30, 2000, the Cassini and Galileo spacecraft were located *outside* (approximately 150 R_J) and *inside* (approximately 8–12 R_J) Jupiter's magnetosphere, making a coordinated set of measurements of the Jovian dust streams. I looked into the charging conditions for dust particles at each spacecraft's location during this set of measurements.

5.4.1 For a Traveling Particle at 8.8 R_J

Here, a dust particle is located at approximately Galileo's position during the December 30 measurements. The velocity shown here is my initial estimate during the flyby, which I later revised in the dynamics results portion of this thesis work. My initial potential was 0 V, which I let reach equilibrium potential. I considered the two extremes of photoelectron emission: χ=1 (conductive particle) and χ=0.1 (dielectric particle). My charging parameters were the following:

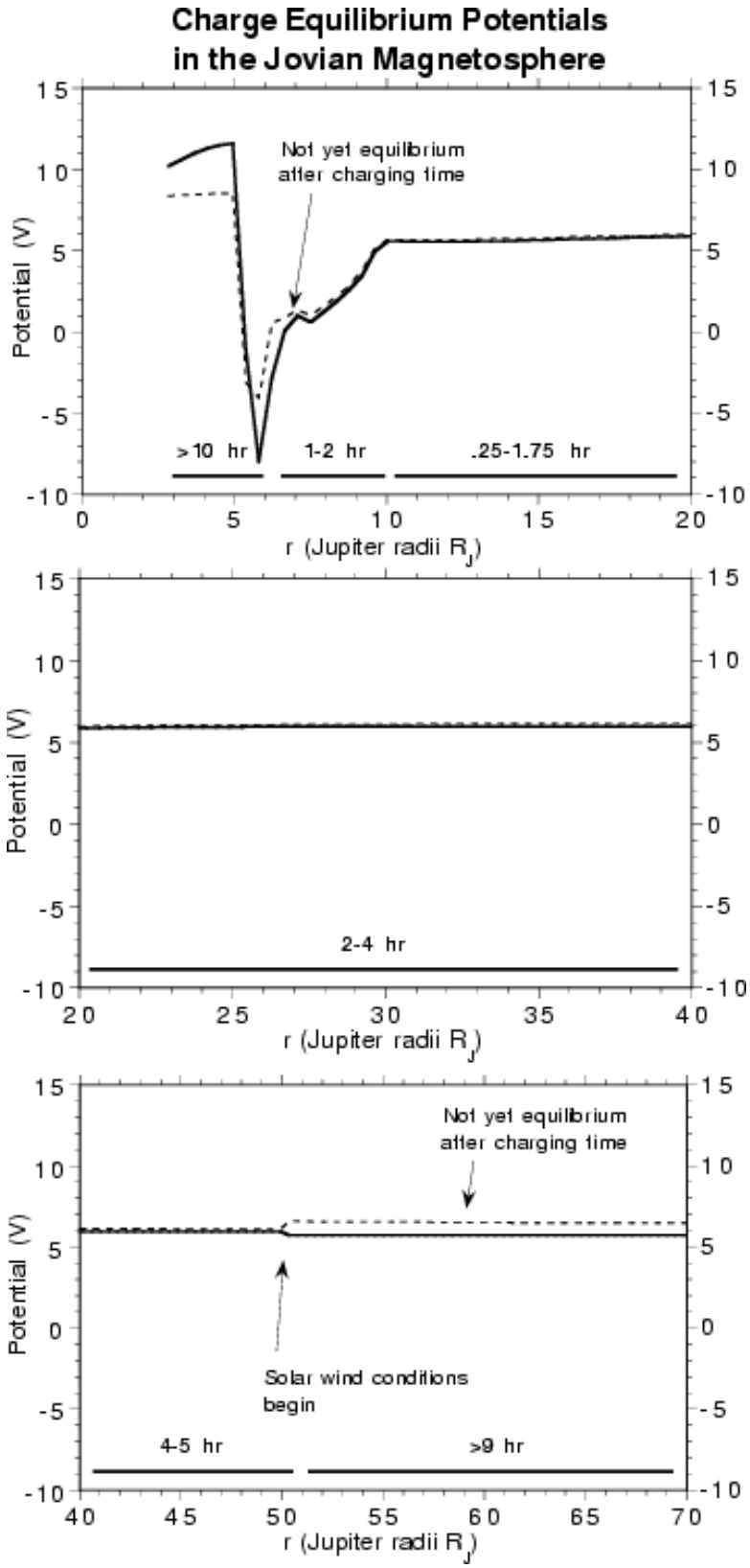

Figure 5.2 : Equilibrium potentials calculated for a 10 nm-sized dust particle in Jupiter's magnetosphere, using the material properties and secondary electron and photoemission parameters described in this section. The solid line is the theoretical equilibrium potential, and the dotted line is the potential calculated at the end of the empirical charging time.

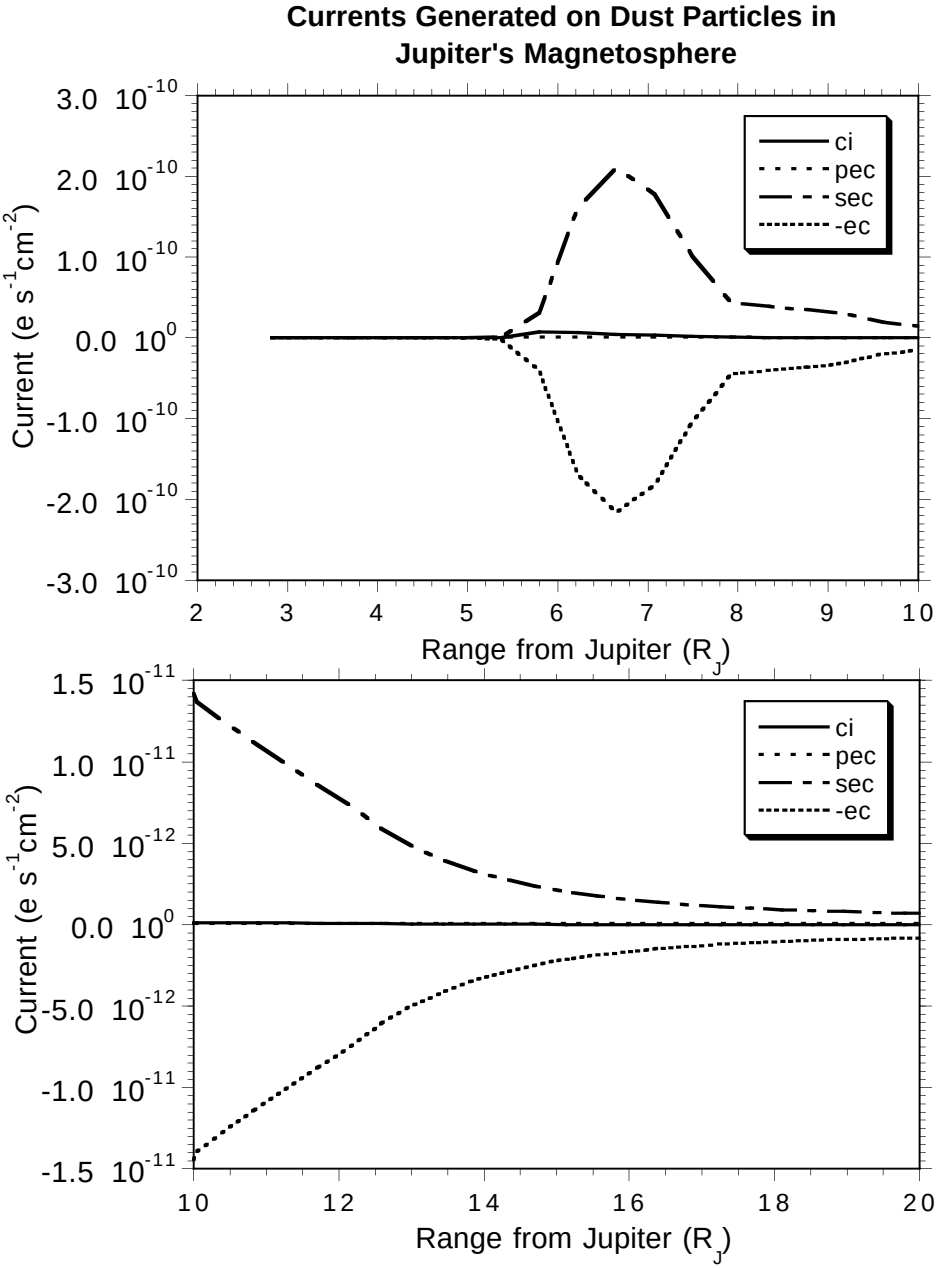

Figure 5.3 : Charging currents calculated for a 0.01 μm-sized dust particle that has reached equilibrium potential in a region of Jupiter's magnetosphere from 2 to 20 R_J, using the material properties and secondary electron and photoemission parameters described in in section 5.2.

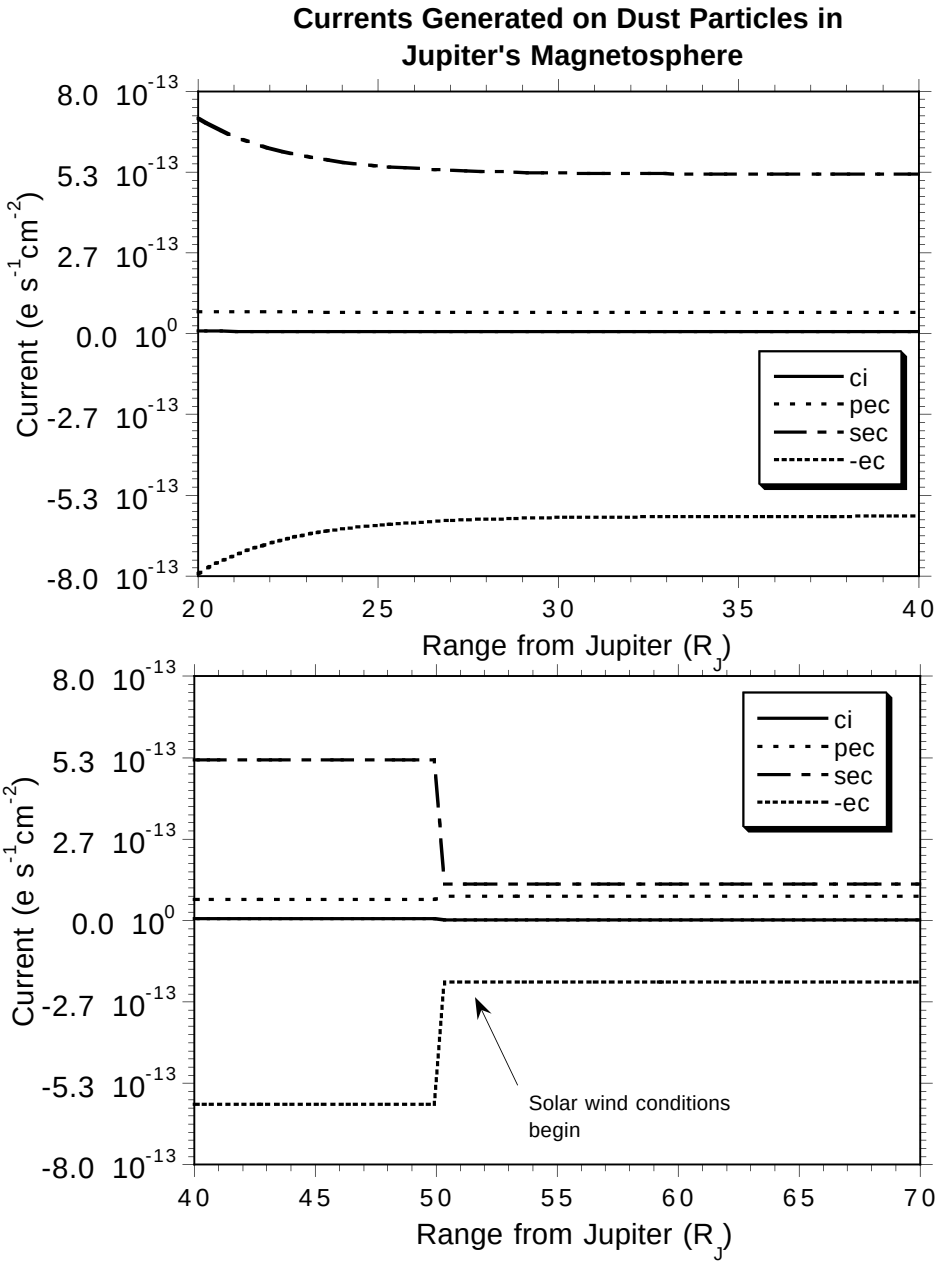

Figure 5.4 : Charging currents calculated for a 0.01 μm-sized dust particle that has reached equilibrium potential in a region of Jupiter's magnetosphere from 20 to 70 R_J, using the material properties and secondary electron and photoemission parameters described in in section 5.2.

δ_m=3.0,	E_m=300eV,	a=0.01μm,
ρ=2.0 g/cm^3,	T_{photo}=2.0 eV,	v=75 km s^{-1}

Table 5.2 : Equilibrium Potential and Currents at Galileo's December 30, 2000 Location

Eq. Pot. (V)	χ	ec	ci	pec	sec
2.7	1.0	$-3.7\,10^{-9}$	$1.1\,10^{-10}$	$3.6\,10^{-11}$	$3.5\,10^{-9}$
2.6	0.1	$-3.6\,10^{-9}$	$1.1\,10^{-10}$	$3.7\,10^{-11}$	$3.5\,10^{-9}$

Units for currents: $e - \text{sec}^{-1} - \text{cm}^{-2}$

Currents abbreviations:

ec=electron collection, ci=ion collection, pec=photoelectron emission, sec=secondary electron emission

The values in Table 5.2 show that the dominant charging currents are the electron collection current and the secondary electron emission current. The secondary electron emission current is indeed important in this region of Jupiter's magnetosphere. When I turned off the current, the equilibrium potential surged to -21.9 V for a conducting particle (χ=1) and to -17.1 V for a dielectric (χ=0.1) particle.

5.4.2 For a Traveling Particle at 150 R_J

Here, a dust particle is located at approximately Cassini's position during the December 30 measurements. The velocity shown here is my initial estimate during the flyby, which I later revised in the dynamics results portion of this thesis work. My initial potential was 0 V, which I let reach equilibrium potential. I considered the two extremes of photoelectron emission: χ=1 (conductive particle) and χ=0.1 (dielectric particle). My charging parameters were the following:

δ_m=3.0,	E_m=300eV,	a=0.01μm,
ρ=2.0g/cm^3,	T_{photo}=2.0eV,	v=275 km s^{-1}

Table 5.3 : Equilibrium Potential and Currents at Cassini's December 30, 2000 Location

Eq. Pot. (V)	χ	ec	ci	pec	sec
5.9	1.0	$-2.0\,10^{-11}$	$1.7\,10^{-12}$	$7.1\,10^{-12}$	$1.1\,10^{-11}$
4.4	0.1	$-1.8\,10^{-11}$	$1.7\,10^{-12}$	$1.5\,10^{-12}$	$1.5\,10^{-11}$

Units for currents: $e - \mathrm{sec}^{-1} - \mathrm{cm}^{-2}$

Currents abbreviations:

ec=electron collection, ci=ion collection, pec=photoelectron emission, sec=secondary electron emission

The values in Table 5.3 show that the dominant charging currents are (again) the electron collection current and the secondary electron emission current. The secondary electron emission current plays a role in the solar wind, especially for a particle that has "dielectric" properties (χ=0.1). For this type of particle, the photoelectron emission current is already low. The particle's equilibrium potential is only 0.4 V when the secondary electron emission current is not considered, so therefore, this current contributes about +4 V to the dust particle's equilibrium potential. For a conducting particle (χ=1), the secondary electron emission current contributes about +1 V to the equilibrium potential: when the secondary electron emission current is "turned off", the particle's potential is 4.25 V.

In order to check the secondary electron emission's role for the charging of a dust particle in the solar wind, I ran a test for a dust particle charging in the solar wind outside of the Earth's magnetosphere. I calculated very similar results to the above case for a dust particle outside of Jupiter's magnetosphere. For a dielectric particle, the secondary electron emission current contributes +3.5 V to the dust particle's equilibrium potential (secondary electron emission current off: 0.9 V, secondary electron emission current on: 4.5 V). For a conducting particle, the secondary electron emission current contributes +1.5 V to the dust particle's equilibrium potential (secondary electron emission current off: 4.8 V, secondary electron emission current on: 6.3 V).

Chapter 6

DYNAMICS

In this chapter, I show results of dynamical simulations, starting with details of the dynamics equations and then I give the simulation results. I show that the dynamics of a particle with a fixed and a varying charge is usually very different: for variable charges, smaller particles can be ejected from the magnetosphere, they are much more sensitive to the magnetic field, and their velocities increase over a much longer distance. I also show here that changing the material properties can change the smallest size of the dust particle ejected from the Jovian environment. Finally I state one plausible set of particle material properties that matches the December 30, 2000 Cassini-Galileo joint dust stream measurements.

6.1 Forces on the Charged Particle

In an Jupiter-centered inertial frame, the motion of a charged dust grain of mass m, is governed by the equation:

$$m\frac{d^2\vec{R}}{dt^2} = \vec{F}_{\rm G} + \vec{F}_{\rm LP} + \vec{F}_{\rm L} + \vec{F}_{\rm SG}$$

where $\vec{F}_{\rm G}$ is Jupiter's gravitational force, $\vec{F}_{\rm LP}$ is the light pressure force, $\vec{F}_{\rm L}$ is the Lorentz force, and $\vec{F}_{\rm SG}$ is the solar gravitational force (Horányi et al. 1997). We may neglect the neutral gas and plasma (Coulomb) drag forces on the dust particle because the time scales used in these runs are short (hours to a day), compared to the time scales over which those forces have an effect.

The gravitational acceleration due to Jupiter is:

$$\left[\begin{array}{c}(-GM_J/r^2)\left(1-\frac{3}{2}J_2\left(\frac{R_J}{r}\right)^2\left(3\sin^2\theta-1\right)-\frac{5}{8}J_4\left(\frac{R_J}{r}\right)^4\left(35\cos^4\theta-30\cos^2\theta+3\right)\right)\hat{r}\\ (-GM_J/r^2)\ \cos\theta\sin\theta\left(3J_2\left(\frac{R_J}{r}\right)^2+\frac{5}{2}J_4\left(\frac{R_J}{r}\right)^4\left(7\cos^2\theta-3\right)\right)\hat{\theta}\end{array}\right]$$

$$=\frac{\vec{F}_G}{m}$$

where G is the gravitational constant, M_J is Jupiter's mass, R_J is Jupiter's radius, r is the dust particle's position vector, θ is the grain's latitude as measured from the equatorial plane, $\hat{r}$ and $\hat{\theta}$ are the unit vectors, and J_2 and J_4 denote the second and fourth zonal harmonic coefficients, which refer to Jupiter's oblateness.

The acceleration due to light-pressure force is:

$$\frac{3\vec{J}_0 Q_{pr}}{4\rho c d^2 a}\hat{r}=\frac{\vec{F}_{\rm LP}}{m}$$

where J_0 is the solar radiation energy flux at 1 AU ($= 1.36 \times 10^6 \mathrm{erg-cm^{-2}-s^{-1}}$, pointing outward from the Sun), Q_{pr} is the radiation pressure coefficient described in section 4.5, ρ is the dust particle's density, d is the planet's distance in AU from the Sun, c is the speed of light, and a is the radius of the charged spherical particle.

The Lorentz acceleration is given by:

$$\frac{Q\,(t)}{m}\left(\vec{E}+\frac{\vec{v}}{c}\times\vec{B}\right)=\frac{\vec{F}_L}{m}$$

Here $\vec{B}$ is the local magnetic field, and the electric field $\vec{E}$ is the corotational electric field: $\left(\vec{r}\times\vec{\Omega}\right)\times(\vec{B}/c)$, if the dust particle is located inside the magnetosphere, where the boundary is located at r=50 $\mathrm{R_J}$. If the particle is located outside of the magnetosphere, then the electric field is driven by the convective motions of the solar wind. See the Appendix for a discussion and the derivation of the corotation electric field and the electric field outside of corotation.

The gravitational acceleration due to the Sun is:

$$GM_S\left(\frac{(\vec{R}-\vec{r})}{\left|\vec{R}-\vec{r}\right|^3}-\frac{\vec{R}}{R^3}\right)=\frac{\vec{F}_{\rm SG}}{m}$$

where M_S is the mass of the Sun.

6.2 Ejection from the Jovian Magnetosphere

6.2.1 Ejection Sizes and Directions: Fixed vs. Variable Charge

In this section I show the ejection of Jovian dust stream particles as a function of particle size. I compare the dynamics for a particle of fixed charge to the dynamics of a particle with a variable charge. I illustrate a range of particle sizes; the travel duration times calculated for each particle size are not uniform: the larger-sized particles required more time duration to cover the same travel distance. Each of the different-sized dust particles are started from a position at Io's orbit, initially traveling at a circular Keplerian velocity, started at a potential of φ =3 V.

For the fixed charge case, the particle's parameters are the following:

$$\boxed{\varphi = 3 \text{ V}, \chi = 1, \rho = 1.5 \text{ g/cm}^3}$$

The material properties and currents for the variable charge case are the following:

$$\boxed{\begin{array}{l}\delta_m = 3.0 \;\; E_m = 300 \text{ eV}, \;\; \chi = 1, \\ \rho = 1.5 \text{g/cm}^3, \; \text{T}_{\text{photo}} = 2.0 \text{ eV}\end{array}}$$

In Fig. 6.1, I illustrate the trajectories for the fixed charge case, and in Fig. 6.2, I illustrate the trajectories for the variable charge case. Two facts emerge from this comparison:

- Variable charging allows *smaller* dust particles to be ejected from Io's vicinity than those particles with a fixed charge.
- Dust particles of the same size, but one traveling with varying charge and the other traveling with fixed charge, can be ejected from the Jovian environment towards the other z direction (e.g., if ejection in the positive z direction for the fixed charge case, then ejection in the negative z direction, for the variable charge case, and vice-versa).

If you look carefully at the the two figures, you can see examples of these effects. For the particle 'size-selection' effect: in the fixed charge case, a particle of size (radius) 5 nm is bound and a particle of size 7 nm is ejected. For particles of variable charge: a particle of size 4 nm is bound, and size 5 nm is ejected.

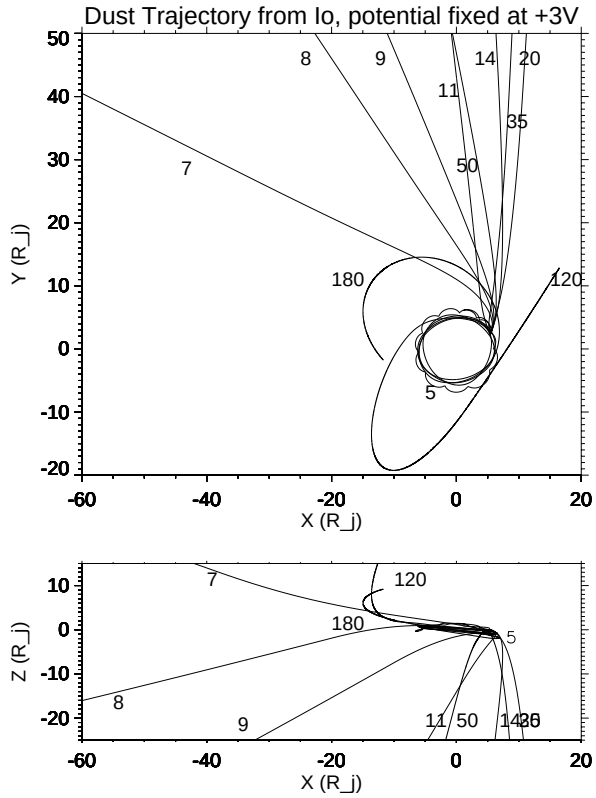

Figure 6.1 : Trajectories for Jovian dust stream particles of different sizes, carrying a fixed potential of +3 V. The small numbers in the figures indicate the particle's radius in nanometer.

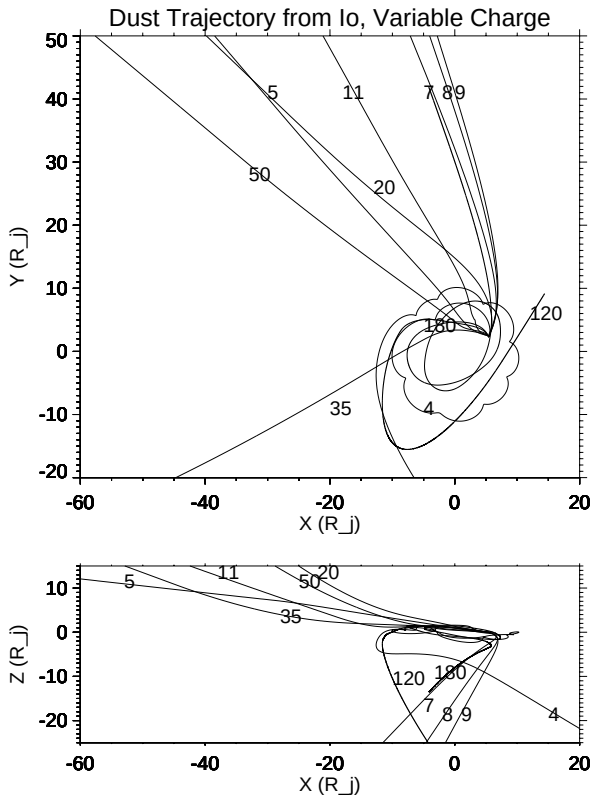

Figure 6.2 : Trajectories for Jovian dust stream particles of different sizes, with a variable charge.

To see the 'z-direction effect': notice that a particle of size 7 nm and fixed charge is ejected in the +z direction and a particle of the same size, but with variable charge, is ejected in the -z direction. Slightly larger particles: 11 nm, 20 nm, 35 nm, 50 nm are ejected in the negative +z directions for the fixed charge cases, and in the positive +z directions in the variable charge cases. Particles of sizes 120 nm and 180 nm are ejected in the +z direction for fixed-charge-particles, and ejected in the -z direction for variable charge particles.

6.2.2 Ejection Sizes for Particles with Different Material Properties

In this section, I demonstrate a dynamics effect when a particle's material properties are changed. I was interested in comparing the ejection dynamics for particles with material properties of SO_x, which is known as a volcanic by-product, and the ejection dynamics of particles with material properties of a silicate: SiO_2, which is a common compound in interstellar dust particles. In this study, I looked for the sizes at which a particle was ejected from the Jovian environment and at the sizes for which a particle was bound to the field, dependent on the particle's material properties. I use the term 'material properties' to denote secondary electron emission parameters, some of which I collected and displayed in Table 5.1. Silicate materials have a high energy E_m and a middle-range δ_m emission yield, therefore, I chose the silicate parameters in order to explore a higher-end energy range for secondary electron emission currents. The parameters I used for this comparison are the following. First, the SiO_2 parameters, from (Whipple 1981), and taking into account the *small-particle effect*, which doubles the emission yield:

$$\boxed{\begin{array}{l}\delta_m{=}4.8,\ E_m{=}400\ \text{eV},\ \chi{=}1,\\ \rho{=}2.0\text{g/cm}^3,\ \text{T}_{\text{photo}}{=}2.0\ \text{eV}\end{array}}$$

Next, the SO_x, parameters, from (Horányi et al. 1997, Heck 1999), which are the same as in the previous section, with the exception of the density.

$$\boxed{\begin{array}{l}\delta_m{=}3.0,\ E_m{=}300\ \text{eV},\ \chi{=}1,\\ \rho{=}2.0\text{g/cm}^3,\ \text{T}_{\text{photo}}{=}2.0\ \text{eV}\end{array}}$$

Each of the different sized dust particles was started from a position of Io's orbit, traveling in a circle with an initial Keplerian velocity, and each particle's initial charge potential was +1 V. I show the resulting trajectories of the particles with these two material properties in Figures 6.3 and 6.4. Each trajectory from top to bottom shows a particle of a different radius, which, in turn, illustrates a particle in a bound orbit, a particle that is on the verge of being ejected, and a particle that is immediately ejected. Several conclusions can be made from this numerical study:

- The dynamics for bound orbits and ejection from Io's vicinity are roughly the same for both material types of particles.

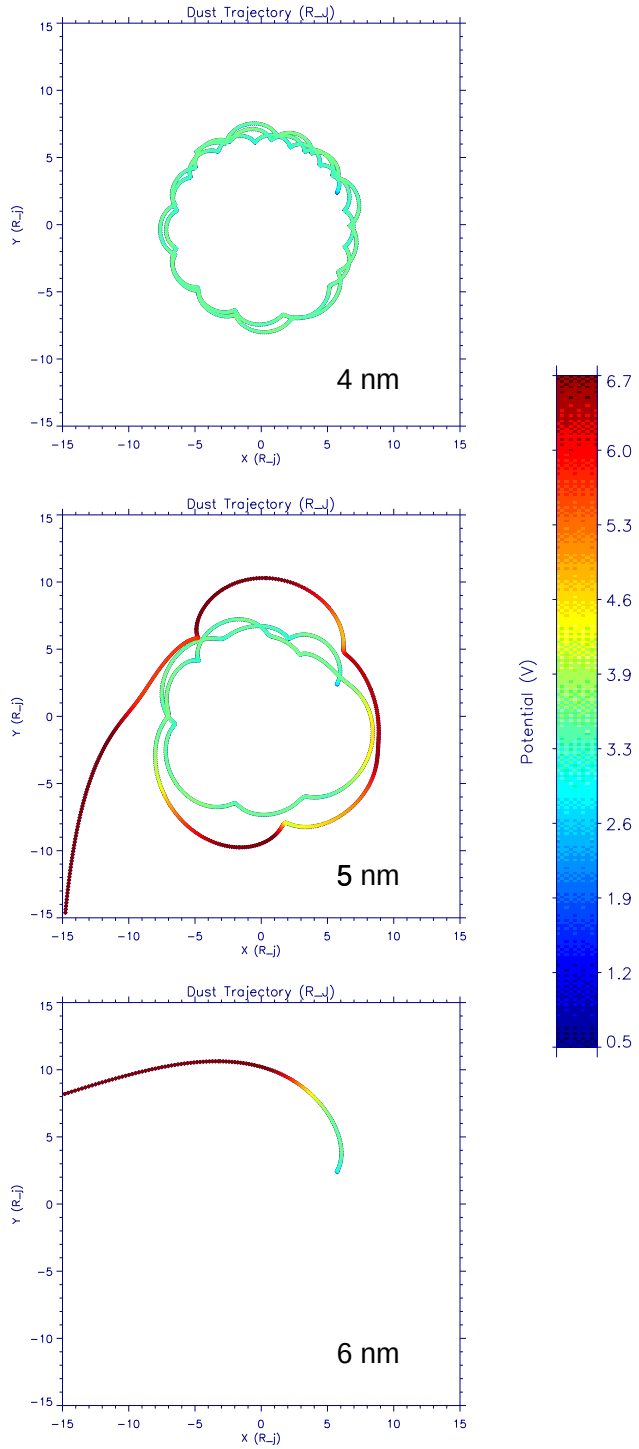

Figure 6.3 : Trajectories for Jovian dust stream particles of different sizes (radius) for a particle with secondary electron emission parameters of SiO_2.

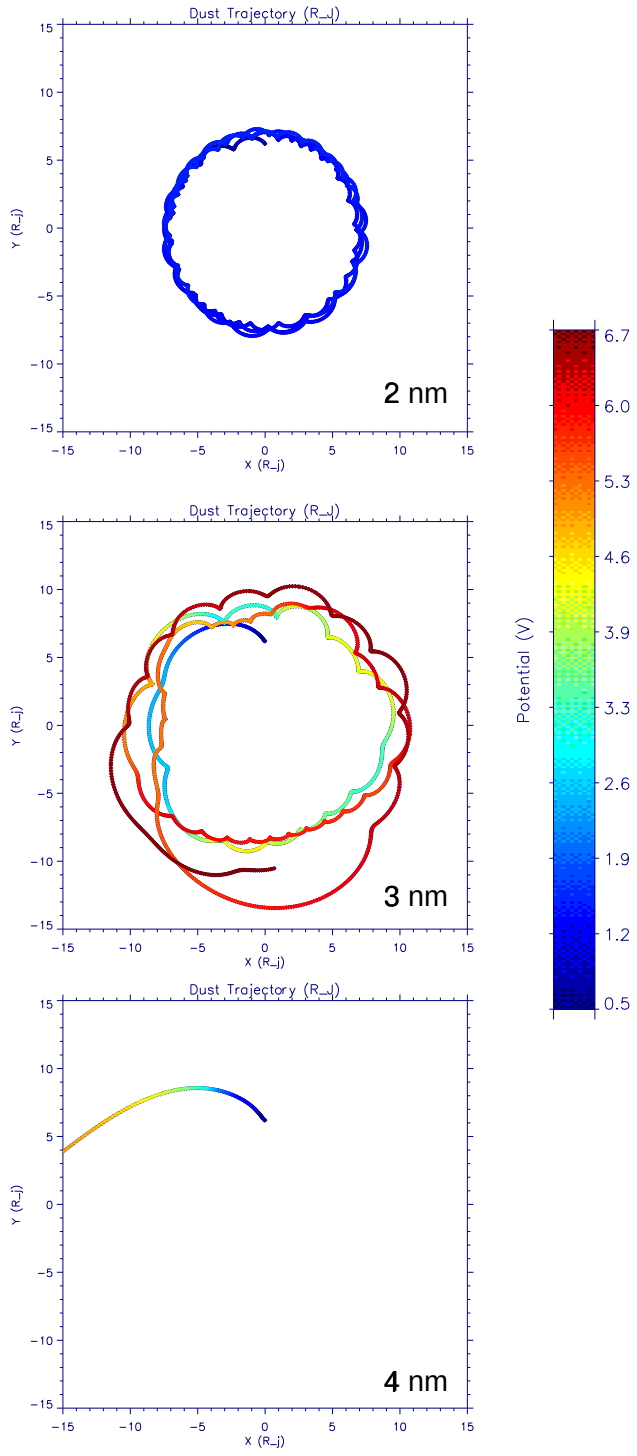

Figure 6.4 : Trajectories for Jovian dust stream particles of different sizes (radius) for a particle with secondary electron emission parameters of SO_x.

- The charge potential carried by the SO_x particle is much lower ($\sim$1 V) than the charge potential carried by the SiO_2 particle ($\sim$3 V).
- Smaller dust particles can be ejected from Io's vicinity, if the material property is SO_x (that is, a particle with a lower energy range for secondary electron emission parameters).

Why are *smaller* SO_x (lower electron/ion impact energy, lower secondary electron yield) particles ejected from the Jovian environment than SiO_2 particles? To answer that question, I looked at the window of particle sizes for which dust particles would escape from traveling in Keplerian orbits in Jupiter's magnetosphere. A useful parameter is the ratio L of the Lorentz force to the planetary gravity force (Krivov et al. 2001, Burns et al. 2001).

$$L \equiv \frac{F_L}{F_G} = \frac{QB_0R_J^3\Omega}{GM_Jcm}$$

where $B_0 = 4.2$ G is Jupiter's field strength at the equator assuming an aligned, centered magnetic dipole, R_J=7.134 10^9 cm is the equatorial radius of Jupiter, Q is the grain charge in ESU units, Ω=1.772 10^{-4} s^{-1} is the rotational frequency of Jupiter, GM_J=1.266 10^{23} cm^3-s^{-2}, and $m = \rho\,(4/3)\,\pi\,(r_*^{\max})^3$ is the mass of a spherical dust particle with radius $r_*^{\max}$. This expression assumes a motionless grain in the equatorial plane ($\vec{v} = 0$, $\theta = 90°$), and L is independent of distance from Jupiter. The ratio is valid in Jupiter's magnetosphere, where an aligned centered magnetic dipole approximation is valid.

For $L \ll 1$, the Lorentz force is a perturbation to the gravitational force, therefore dust particles follow Keplerian orbits. For $L \gg 1$, the gravitational force is a perturbation to the Lorentz force, therefore, the dust particles act as plasma ion and electron particles, which gyrate about the planet's magnetic field lines. Between these two regimes lies a window $r_*^{\min} < r_* < r_*^{\max}$ of particle sizes r_* for which positively charged dust particles can escape. The particles with the smallest grain sizes in this window $r_*^{\min}$ experience a weaker Lorentz force and a larger gyroradii than those even smaller particles which are inescapeably bound to the magnetic field lines, and the particles with the largest grain sizes in this window $r_*^{\max}$ barely have enough energy to escape from being bound gravitationally to Jupiter (Hamilton & Burns 1993, Horányi 1996*b*, Burns et al. 2001).

In Figures 6.5 and 6.6, I show the ratio of the Lorentz force to the gravitational force for these two particles of different material properties. The top, middle and bottom panels correspond to the same sizes as the previous two figures (Fig. 6.3 and Fig. 6.4). We see the excursions of the ratios between the Lorentz and gravitational forces, with the bottom panel illustrating the situation when a particle escapes the magnetic field. The sharp rise and peak in the two bottome panels is dependent upon the location of the magnetosphere boundary- the rise occurs between 40 and 50 R_J, at which point, the particle is suddenly no longer in the Jovian magnetosphere (a boundary I impose in the dynamical simulation). The particle with SiO_2 material properties is carrying a higher charge potential (and a smaller Q/m), when it escapes, than the particle with SO_x material properties. Now examining the window of particle sizes, for which charged dust particles can escape.

Smallest Grain Size for Ejection

To find the *smallest* grain size for grain ejection, start with the gyration of a tiny grain along Jupiter's magnetic field lines (Horányi 1996*b*):

$$r_{gyr} = \left| \frac{\omega m c}{Q B} \right|$$

where $B = B_0 \left(R_J / r\right)^3$ is the magnetic field for an aligned centered magnetic dipole, and ω, for a particle in a Kepler orbit is (Horányi 1996*b*):

$$\omega = r\Omega - \sqrt{\left(G M_J\right) / r}$$

For example, at Io's location (r=5.9R_J), ω=5.724 10^6 cm s^{-1}. Morfill et al. (1980*b*) describe the motion of tiny grains bound to the magnetic field line with a *guiding center approximation*, which is valid if:

$$r_{gyr} \left| \frac{\nabla B}{B} \right| < 0.1$$

Since $|\nabla B / B| = 3/r$ in the equatorial plane of an aligned centered dipole, then $r_{gyr}\left(3/r\right) < 0.1$. Therefore, we can solve for the grain radius, r_{gr}, from this expression, substituting the grain's density ρ for m, and substituting the grain's surface potential φ for the grain's charge: $Q = \left(\varphi/300\right) r_{gr}$:

$$\begin{aligned}
\left|\frac{\omega m c r^3}{Q B_0 R_J^3}\right| (3/r) &< 0.1 \\
\frac{r_{gr}^3 \omega \rho 4\pi c r^2}{Q B_0 R_J^3} &< 0.1 \\
\frac{300 r_{gr}^2 \omega \rho 4\pi c r^2}{\varphi B_0 R_J^3} &< 0.1 \\
r_{gr} &= \left[\frac{0.1 \varphi B_0 R_J^3}{300 \omega \rho 4\pi c r^2}\right]^{\frac{1}{2}}
\end{aligned}$$

The smallest grain size for ejection using this expression for the SiO_2 particle is 9 nm and for the SO_x particle is 7.4 nm. Because this expression makes simplified assumptions for Jupiter's magnetic field, one would not expect a close match to the numerical results. Nevertheless, this comparison shows that particles with (lower electron/ion impact energy, lower secondary electron yield) material properties give rise to smaller particles being ejected from the Jovian environment.

It's useful to know the charge-to-mass ratio of the two particles. For the SiO_2 particle at the point where the L-ratio is the highest (in the 6 nm diagram, it is marked by a peak at L=3300), the charge-to-mass ratio is 1295 C kg^{-1}. For the SO_x particle at the point where the L ratio is the highest (in the 4 nm diagram, it is marked by a peak at L=4850), the charge-to-mass ratio is 4482 C kg^{-1}.

Largest Grain Size for Ejection

To derive the *largest* grain size for grain ejection, I begin with Krivov et al. (2001), and solve for r_{gr}:

$$\begin{aligned}
L &= \frac{Q B_0 R_J^3 \Omega}{G M_J c m} \\
r_{gr} &= \left[\frac{\varphi B_0 R_J^3 \Omega}{L 300 G M_J c \rho\, (4/3)\, \pi}\right]^{\frac{1}{2}} \\
r_{gr} &\approx \sqrt{\frac{0.0057 \varphi}{\rho L}}
\end{aligned}$$

The last expression gives a convenient relationship for the grain size as a function of potential, density and ratio L, where the unit of φ is in Volts, and the unit of density is g cm^{-3}. If $L \geq (1/2)$, the grain will be ejected from the circumjovian space

into interplanetary space in a parabolic or hyperbolic orbit (Hamilton & Burns 1993, Krivov et al. 2001), therefore, the above expression gives the largest grain size for ejection.

The largest grain size for ejection using this expression for the SiO_2 particle is 210 nm and for the SO_x particle is 175 nm.

6.2.3 Ejection: Sensitivity to the Magnetic Field Expansion

To continue exploring and comparing the dynamical effects of particles carrying a variable and a fixed charge, I demonstrate, in this section, the particle's sensitivity to the magnetic field model used in the dynamics calculations. The conclusion here is that a particle with a fixed charge is relatively insensitive to the expansion order of the model magnetic field, whereas a particle carrying a variable charge can be very responsive to the expansion of the magnetic field.

In previous chapters, I described the complexities of Jupiter's magnetic field. The magnetic field I assumed, which is Connerney's approximation (Connerney 1981, Connerney 1993), implements a third-order (*octupole*) magnetic field expansion, which has its largest effect in the inner to middle portion of the Jovian magnetosphere. In this small study, I utilized a first-order expansion (dipole), a second-order expansion (quadrupole), and a third-order expansion (octupole), and noted the particle's final z position after 30 hours of travel time. Both fixed and varying charge particles were started at 6.2 R_J, and the potential on the fixed charge particle was +5 V. The parameters for the varying charge particle were the SO_x properties shown in the box of the previous section. I assumed Connerney's O_4 magnetic model. Table 6.1 shows the results.

6.3 Forces on a Traveling SO_x Dust Particle

The dominant force governing the dynamics of tiny charged dust particles is not necessarily the gravitational force with which astronomers are most familiar. The dynamics of submicron-sized particles is governed by non-gravitational forces, in particular, the Lorentz force. In order to grasp the significance of the forces on the Jovian dust stream particles, in this section, I illustrate the strengths of the forces on

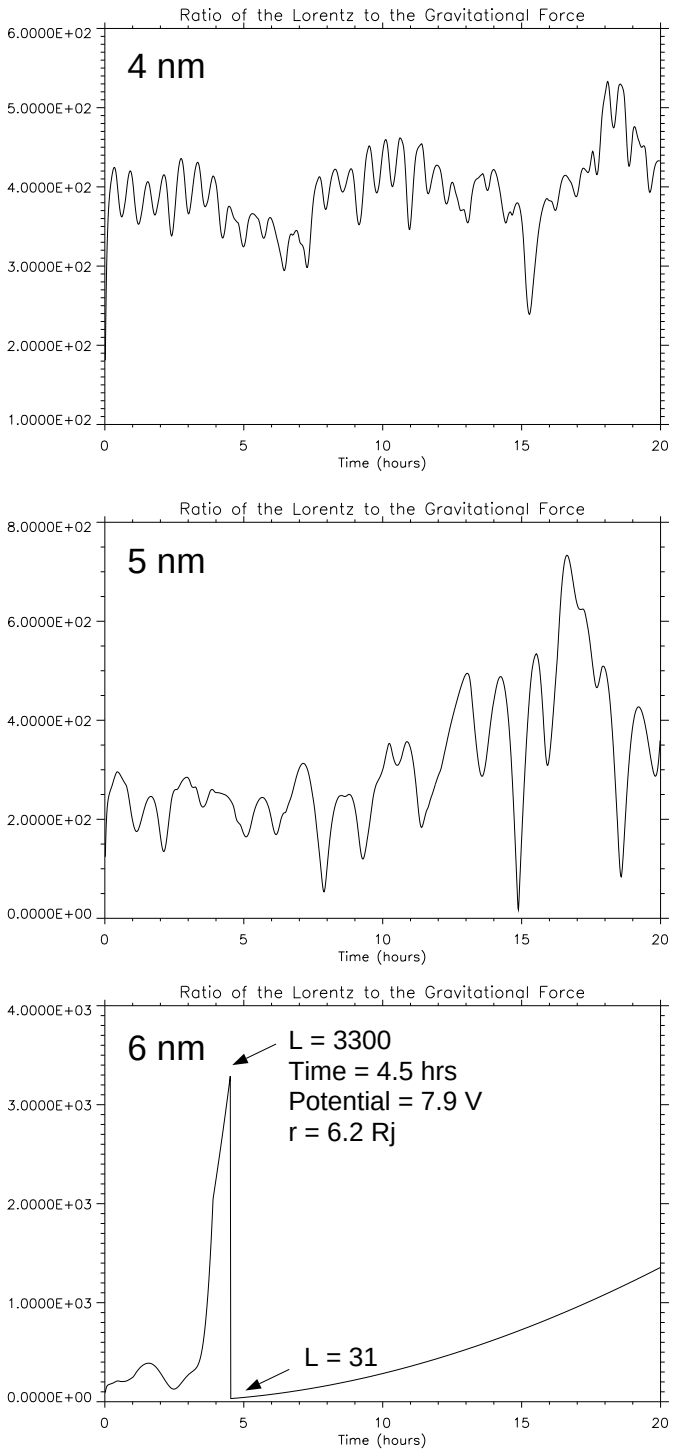

Figure 6.5 : Ratio of the Lorentz force to the gravitational force for Jovian dust stream particles of different sizes for a particle with secondary electron emission parameters of SiO_2.

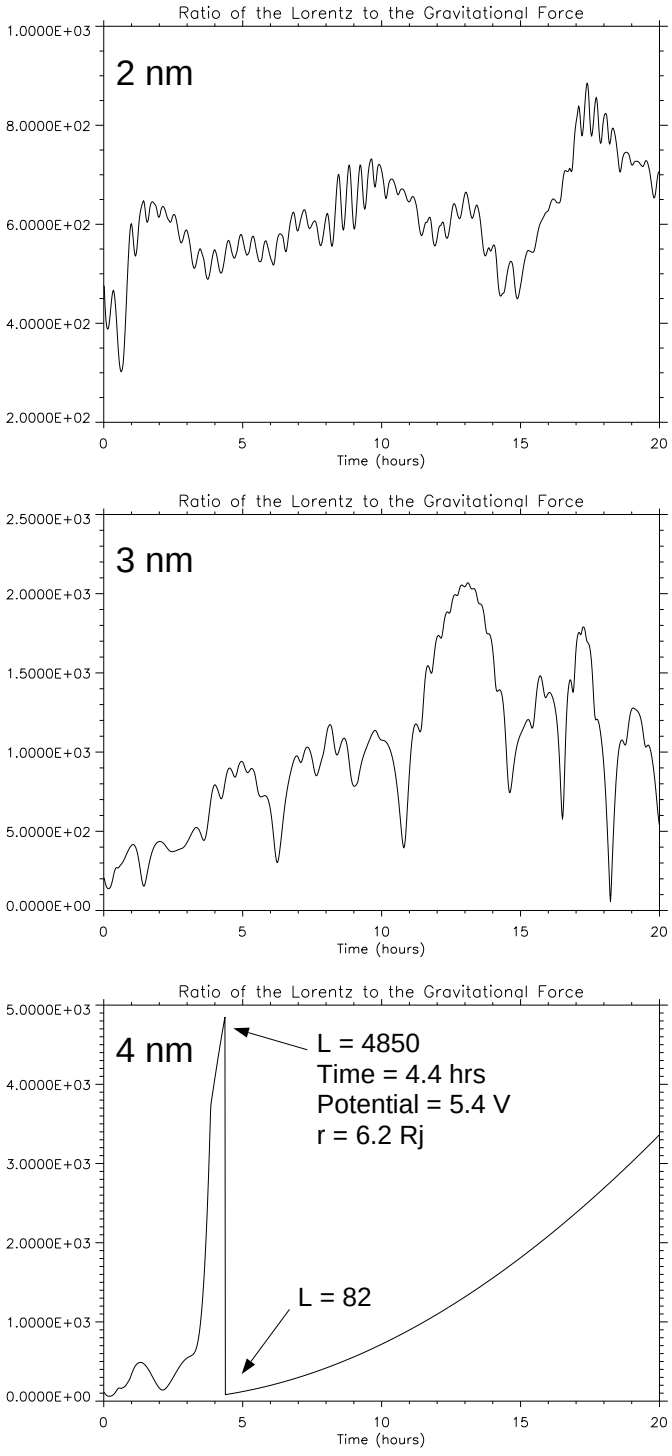

Figure 6.6 : Ratio of the Lorentz force to the gravitational force for Jovian dust stream particles of different sizes for a particle with secondary electron emission parameters of SO_x.

Table 6.1 : Sensitivity to Magnetic Field Expansion

Charge	Mag Field Order	Final z (R_J)
Fixed	3^{rd}-order (octupole)	205
	2^{nd}-order (quadrupole)	205
	1^{st}-order (dipole)	200
Varying	3^{rd}-order (octupole)	-112
	2^{nd}-order (quadrupole)	-131
	1^{st}-order (dipole)	-5

a typical dust stream particle ejected from Io as a function of distance from Jupiter. I chose the 4 nm-sized particle, of which the trajectory can be seen in Fig. 6.4. Using the charging parameters for a SO_x particle listed in section 6.2.2, and given an initial +1 V potential, I calculated the forces using the equations in section 6.1. I display these forces in Figs. 6.7 and 6.8. For example, the ratio of the Lorentz force to the gravitational force at 6.2 R_J, 10 R_J, 20 R_J, 30 R_J, 40 R_J, and 50 R_J is: ~100, 400, 200, 500, 2300, and 4800, respectively.

6.4 Velocities vs. Distance for Particles of Fixed and Varying Charges

The speeds of submicron-sized charged dust particles can be underestimated if the charge carried by the particle is assumed to be fixed. In this section, I demonstrate a velocity effect of the dynamics of a Jovian dust stream particle, when the particle's charge is fixed versus when the particle's charge is variable. For variable charge dust dynamics, the velocities of the smallest sized dust particles continue to increase to about 30 R_J. However, the velocities for the particles with fixed charges reach a near-plateau, where the particles reach a distance of about 10 R_J, and they remain at that velocity for the remainder of the distance through the Jovian magnetosphere. Since the velocities of the variable charge (smallest) particles continue to increase while the particles are traveling through a substantial portion of the magnetosphere, then the variable charge (smallest) particles have shorter travel times than the fixed charge particles of the same size. This difference explains why the tiny particles traveled faster

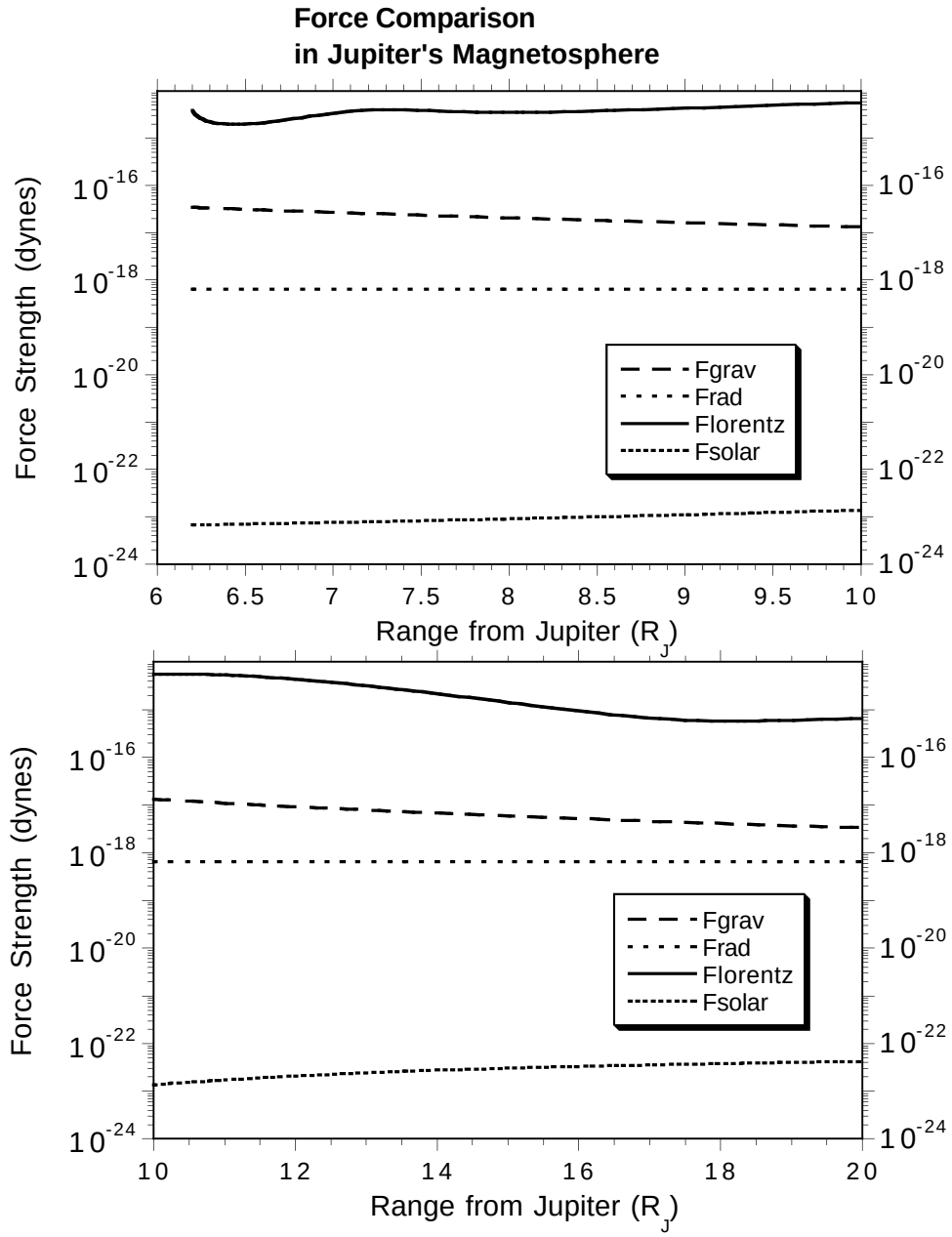

Figure 6.7 : Forces calculated for a 4 nm-sized dust particle in a region of Jupiter's magnetosphere from 5 to 20 R_J, using the material properties and secondary electron and photoemission parameters described in section 6.2.2 and the forces described in section 6.1.

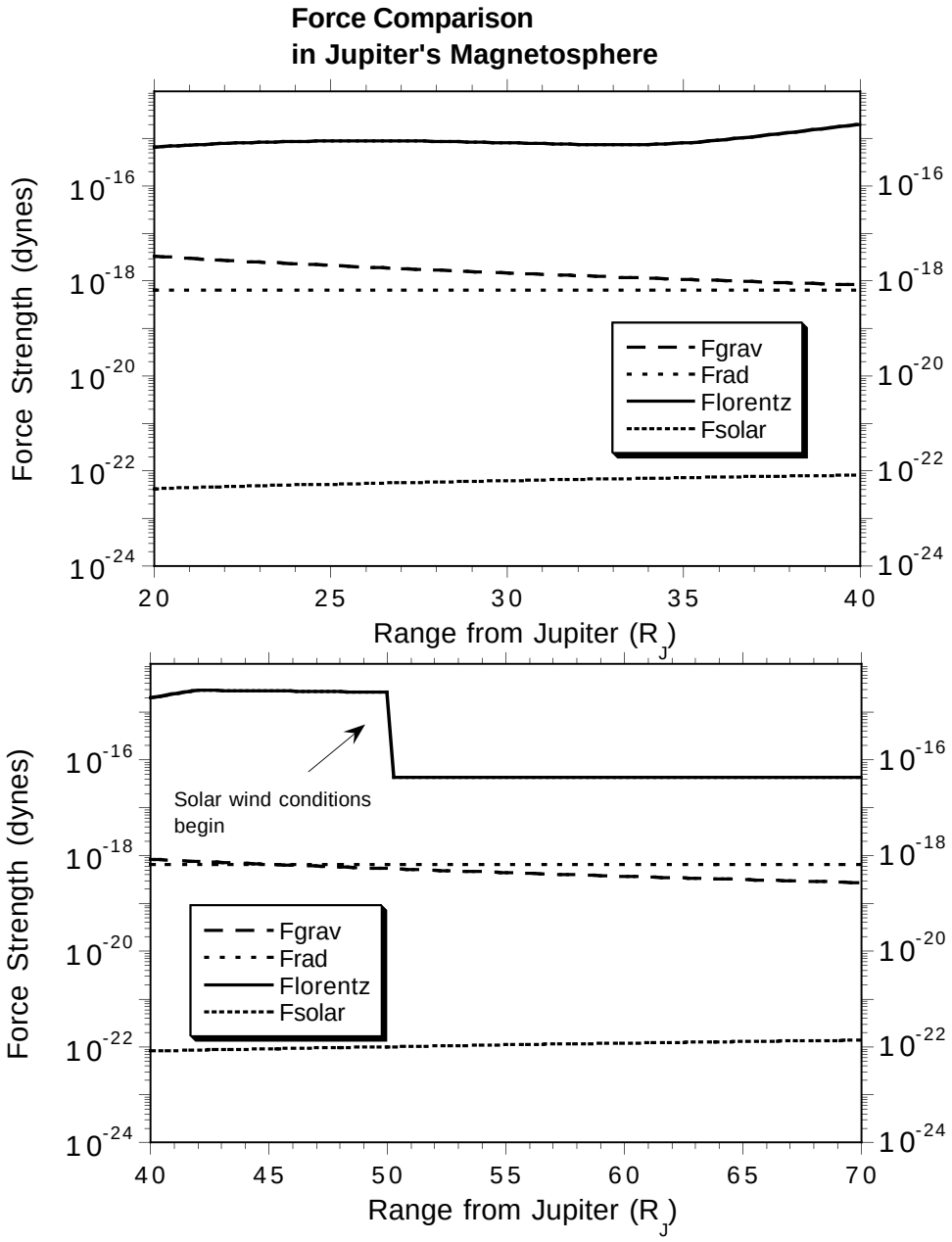

Figure 6.8 : Forces calculated for a 4 nm-sized dust particle in a region of Jupiter's magnetosphere from 20 to 70 R_J, using the material properties and secondary electron and photoemission parameters described in section 6.2.2 and the forces described in section 6.1.

than originally predicted (the predictions assumed a fixed charge for the particles) between the two spacecraft: Galileo and Cassini during the joint December 3, 2000 dust stream measurements.

In the next pair of figures, Fig. 6.9 and Fig. 6.10, I show the velocities for the fixed charge case and the variable charge case, using the same set of parameters for SO_x as in the section 6.2.1. Since the charge potential, which the particle carries

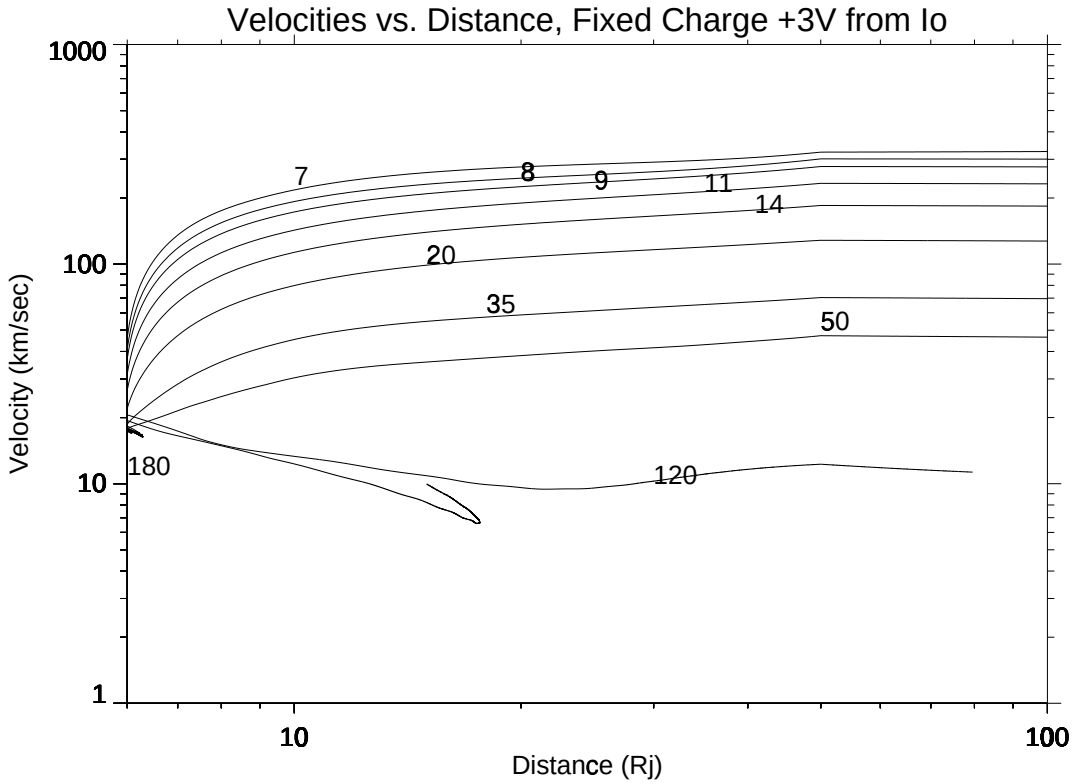

Figure 6.9 : Velocities vs. distance from Jupiter for Jovian dust stream particles of different sizes, carrying a fixed potential of +3 V. The numbers denote particle radius in nanometers.

while it's traveling, is *not* an equilibrium potential, it's worthwhile to see how the particle's charge potential in velocity-space is changing, as the particle travels through the Jovian magnetosphere. In order to compare to the two previous figures, I use the same charging parameters and initial conditions as in the section 6.2.1. In the next figure, Fig. 6.11, I show a plot of velocities versus distance of particles of sizes: 5 nm and 8 nm, color-coded with the particles' charge potentials.

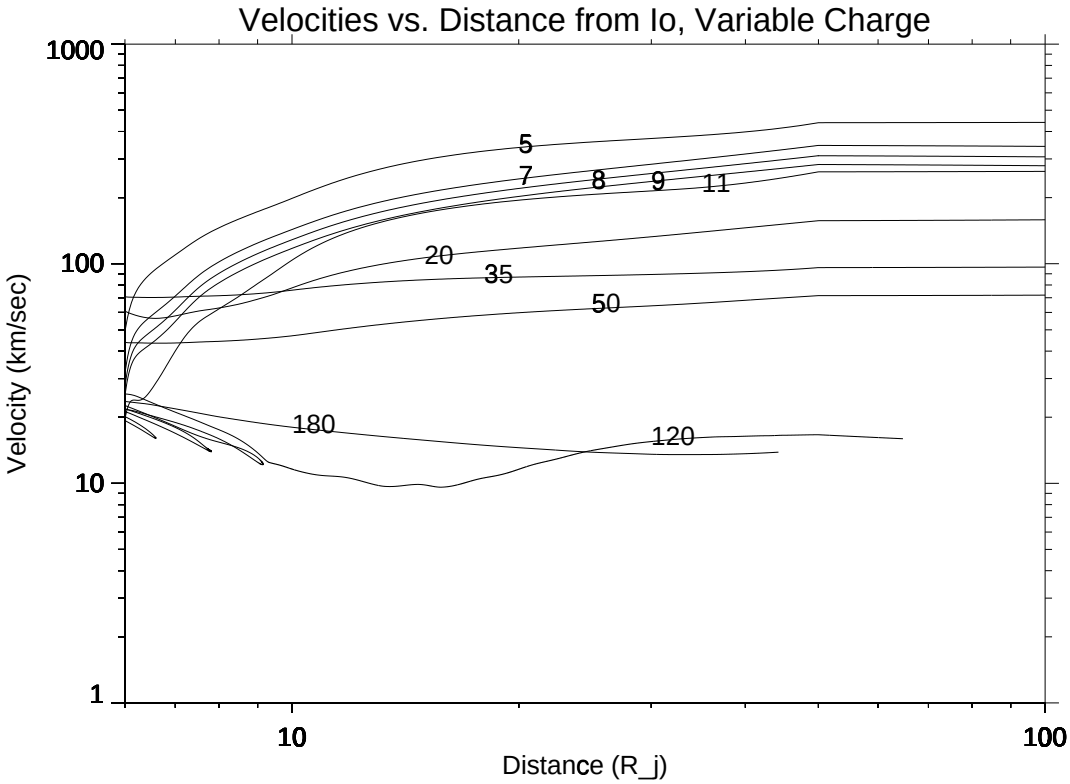

Figure 6.10 : Velocities vs. distance from Jupiter for Jovian dust stream particles of different sizes, carrying a variable charge, starting from +3 V, and using the same of material properties parameters for SO_x as described in section 6.2.1. The numbers denote particle radius in nanometers.

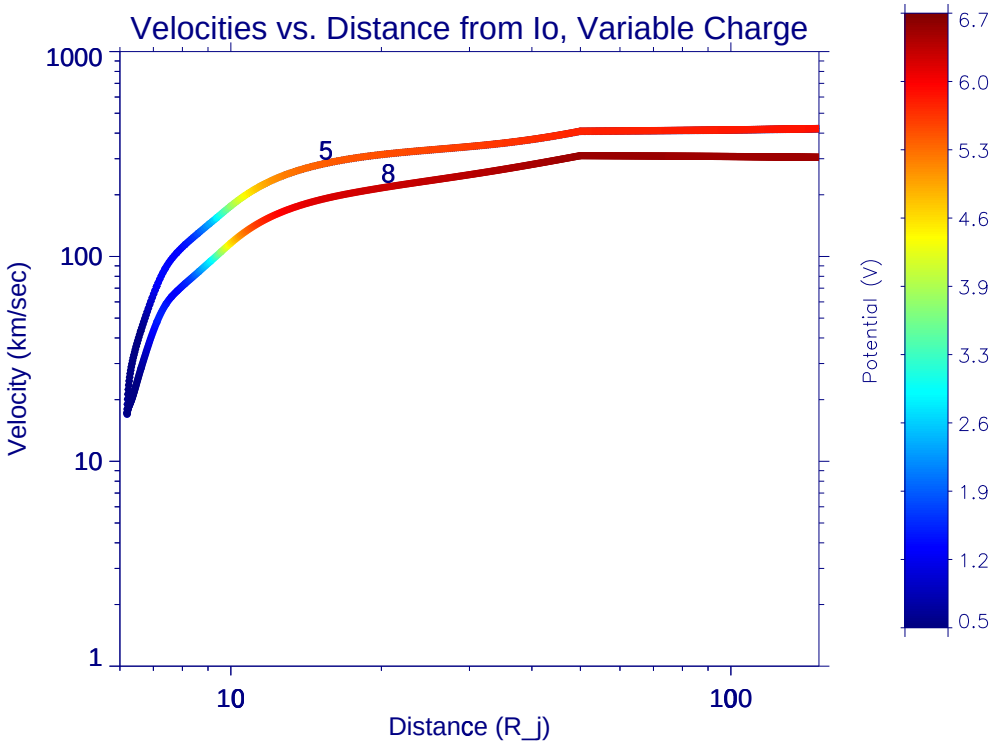

Figure 6.11 : Velocities vs. distance from Jupiter for Jovian dust stream particles of radius size 5 nm and 8 nm. The color indicates the value of the particle's charge potential. These particles started with an initial potential of +3 V, and used the same of material properties parameters for SO_x as described in section 6.2.1.

6.5 Material Property Explorations for the Cassini-Galileo Joint Measurements

Now I wish to gain some understanding of the charge and velocities of the Jovian dust stream particles which result when the particle parameters are changed. In this section, I describe one set of particle material properties which match the dust stream particles' travel time, which were measured by the two spacecraft during the Cassini-Jupiter flyby/Galileo observations on December 30, 2000, Day 364.665. Even though the speeds of the particles are still being analyzed, our (the Heidelberg dust group) initial analysis shows that the dust particles were observed to travel faster than predicted between the two spacecraft: Cassini, located *outside* of the Jovian magnetosphere at 140 R_J, and Galileo, located *inside* of the Jovian magnetosphere, at 11.6 R_J. Initial predictions from models, using a *fixed charge*, of particle trajectories gave a travel time of $\Delta t = 9$ hours for a dust particle to move between Galileo and Cassini, however data analysis now shows that the particles traveled in $\sim$7 hours between the two spacecraft (see Fig. 2.7). Therefore, my goal was to match a $\sim$7 hour travel time.

This work indicates a first effort. My steps, which I follow in Table 6.2, were as follows:

1. Find the proper geometrical *phase* for a particle released from an Io-Keplerian orbit which induces the particle to travel near the ecliptic plane (so that the two spacecraft could detect the stream).
2. Determine a reasonable particle density so that the particle won't be traveling unrealistically fast or traveling too slow for detection at the two spacecraft.
3. Start with sulfur material properties (Heck 1999), and vary the δ_m and E_m, to learn the ranges of δ_m and E_m, which cause the particle to go into a bound orbit, travel too fast, or travel too slow.
4. Change the particle size to gain a rough understanding of reasonable particle sizes for each set of material properties. Note how changing the density affects the outcome.
5. Find if the initial charge make a difference.
6. Determine the affect of changing the photoelectron emission yield.
7. Keep a record: Size, Δt, Ratio V, φ_i, χ, E_m, δ_m, φ (Gal, Cas), where Ratio V is the ratio of particle speed between Cassini to that at Galileo, φ_i is the

initial charge potential on the particle, χ is the photoelectron emission yield, E_m and δ_m are the secondary electron emission material properties parameters, and φ (Gal, Cas) is the charge potential carried by the particle at Galileo and Cassini's location.

Each line, progressively by rows, in Table 6.2, follows the above steps. The first item regarding the phase of the particle's release needs to be described in some detail, therefore I devote the next section to that. The other items: 2 through 7 can be seen in the table. When I tried a new parameter, I noted the change with that new parameter marked in boldface. For each line in this table, I use the same phase at 100°. The 'small-particle approximation' described in section 5.1.6 is already counted, e.g. δ_m=3.0 is δ_m=1.5 for a less than 0.1 micrometer-sized particle.

6.5.1 The role of the phase of particle release

To find the proper geometrical *phase* for a particle released from a near Io-Keplerian orbit at 6.2 R_J, which would induce the particle to travel near the ecliptic plane so that the two spacecraft could detect the stream, one must compute trajectories around Io's orbital location, changing only phases *for each different particle size.* From the work described in section 6.2.1, where I noted the sizes at which sulfur-like particles could be ejected near Io's orbit, outside of the plasma torus at 6.2 R_J, I assumed a 'middle-range' particle size (radius) of 6 nm, and computed 144 phases, which can be seen in Fig. 6.12. One of those trajectories brings the particle closest to the Cassini spacecraft, and that trajectory is shown colored with the value of particle's charge potential.

Figure 6.12, illustrates only *one* particle size, 6 nm-radius, therefore, if one wishes to model a 'burst-event' of different particle sizes, then one would pick the phase shown with the thick colored line and release different sized particles. Figure 6.13 shows the result of one possible burst event at a phase equal to 100°.

However, if one wishes to model a *collimated* stream of different particle sizes, then one must find appropriate phases for *each* particle size, and note that different particle sizes travel at different speeds. A collimated stream of different sized particles detected at Cassini's location would require, in space, an 'arc'-ejection of different sized particles, released at staggered times because the smaller particles travel fast and the larger particles travel slower.

Table 6.2 : Material Property Explorations for the Cassini-Galileo Joint Measurements. The columns follow item number 7 in the text, where the particle parameters are: size (nm), travel time Δt, ratio of velocities between Cassini and Galileo V, initial charge potential φ_i, photoelectron emission yield χ, secondary electron emission material properties: E_m and δ_m, the charge potential at the location of the two spacecraft φ (Gal, Cas), and density of the particle ρ. The Notes are comments regarding the dynamical behavior of the particle.

Size (nm)	Δt (hr)	Velocity Ratio	φ_i (V)	χ	E_m (eV)	δ_m	φ (V) (@Gal,Cas)	Density (g/cm^3)	**Notes**
6	7.0	2.0	1.0	1.0	300	3.0	5.4,6.3	1.5	OK
6	6.3	2.1	1.0	1.0	300	3.0	5.4,6.4	**1.25**	too short
6	6.8	2.0	1.0	1.0	300	3.0	5.4,6.3	**1.35**	OK
6	7.3	2.0	1.0	1.0	300	3.0	5.4,6.4	**1.75**	OK
6			1.0	1.0	300	**2.5**		1.5	Bound
6			1.0	1.0	300	**3.5**		1.5	Loops 1 orbit, then ejected
6			1.0	1.0	300	**4.0**		1.5	Bound
6			1.0	1.0	**200**	3.0		1.5	Bound
6			1.0	1.0	**250**	3.0		1.5	Bound
6			1.0	1.0	**350**	3.0		1.5	Bound
6	7.0	2.0	**3.0**	1.0	300	3.0	5.2,6.1	1.5	OK
6	7.0	2.0	**4.0**	1.0	300	3.0	5.1,6.1	1.5	OK
6	7.0	2.0	1.0	**0.1**	300	3.0	5.4,6.1	1.5	OK
5	6.0	2.1	1.0	1.0	300	3.0	5.4,6.3	1.5	wrong angle to Cassini
7	7.8	2.0	1.0	1.0	300	3.0	5.7,6.6	1.5	wrong angle to Cassini
8	7.9	1.8	1.0	1.0	300	3.0	5.9,6.7	1.5	wrong angle to Cassini

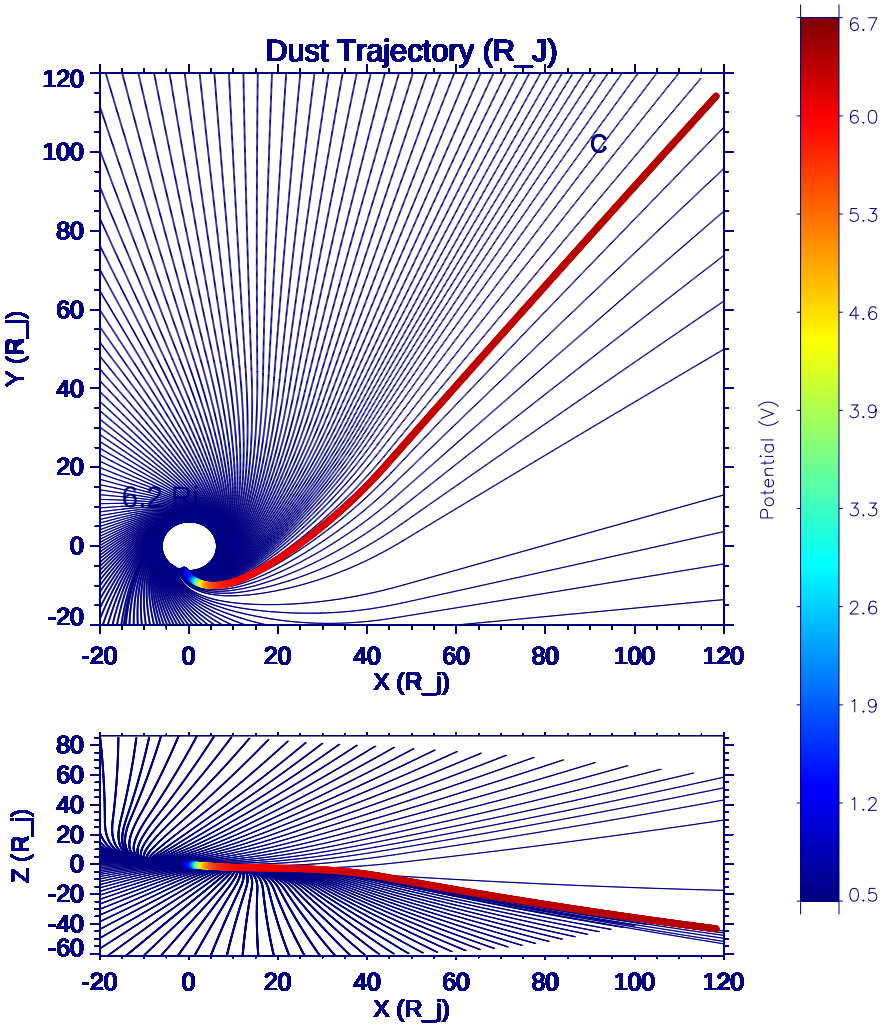

Figure 6.12 : Dust particle trajectories in x-y (top) and x-z (bottom) Jupiter-centered coordinates for a 6 nm-radius particle released from a near-Io Keplerian orbit at 6.2 R_J. The thick line with the color denoting the particle's charge potential indicates a reasonable trajectory at phase equal to 100°, which would bring the particle near to the Cassini spacecraft.

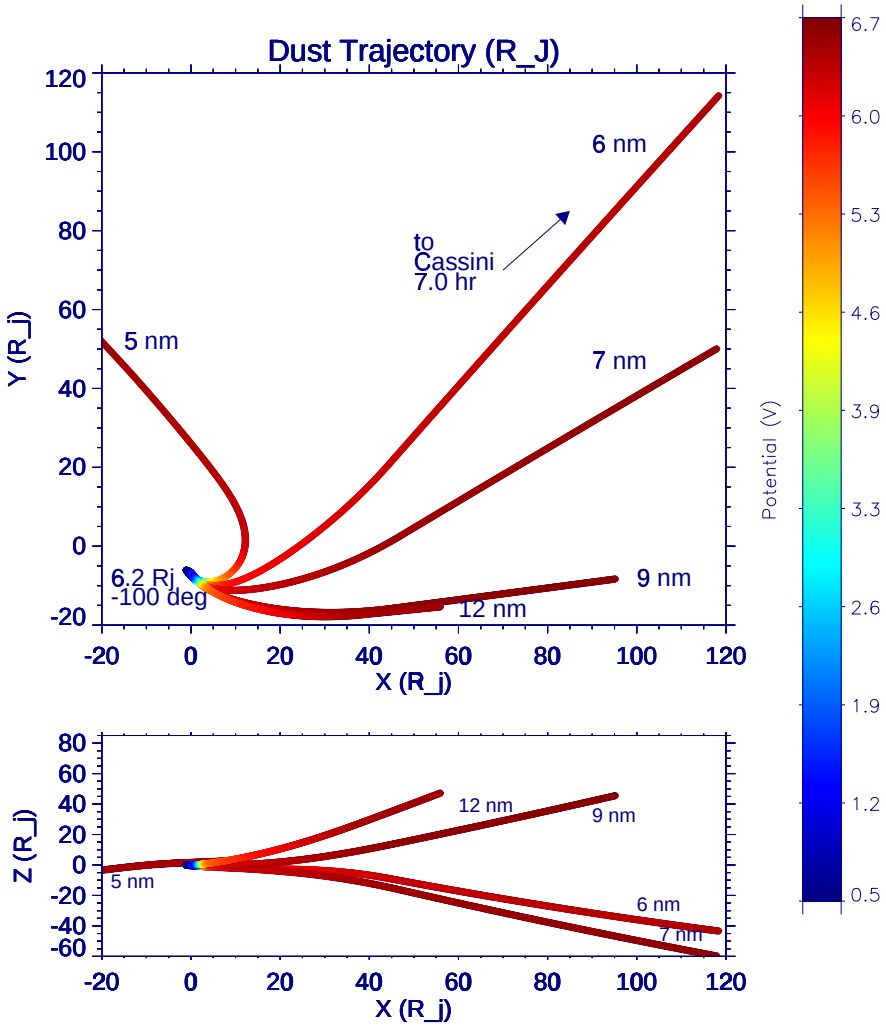

Figure 6.13 : Dust particle trajectories in x-y (top) and x-z (bottom) Jupiter-centered coordinates for different sized particles released from a near-Io Keplerian orbit at 6.2 R_J. The colors indicate the values of the particle's charge potentials. The trajectory with the arrow indicates a reasonable trajectory which would bring the particle near to the Cassini spacecraft.

6.5.2 Results

From this preliminary analysis, in order to meet the time-of-flight that the dust particles achieved during the December 2000 Galileo-Cassini dust stream measurements, the smallest dust particles could have the following range of parameters: size: 6 nanometers, density: 1.35–1.75 g/cm^3, initial charge potential: 1–4 V, secondary electron emission yield: 3.0, dependent on a maximum electron energy 300 eV, and a photoelectron emission yield: 0.1–1.0, which produce dust particle speeds: 220\450 km s^{-1} (Galileo\Cassini) and charge potentials: 5.5\6.3 V (Galileo\Cassini).

Chapter 7

SYNOPSIS OF IO REVEALED IN THE JOVIAN DUST STREAMS

The Jovian dust streams are high-speed (at least 200 $\mathrm{km\,s^{-1}}$) collimated streams of submicron-sized particles traveling in the same direction from a source in the Jovian system. They were discovered in March 1992 by the cosmic dust detector instrument onboard the Ulysses spacecraft, when the spacecraft was just past its closest approach to Jupiter. Observations of the Jovian dust stream phenomena continued in the next nine years. A second spacecraft, Galileo, now in orbit around Jupiter, is equipped with an identical dust detector instrument to Ulysses' dust instrument. Before and since the Galileo spacecraft's arrival in the Jupiter system in December 1995, investigators recorded more dust stream observations. In July and August 2000, a third spacecraft with a dust detector (combined with a chemical analyzer), Cassini, traveling on its way to Saturn, recorded more high-speed streams of submicron-sized particles from the Jovian system. The many years-long successful Jovian dust streams observations reached a pinnacle on December 30, 2000, when both the Cassini and Galileo dust detectors accomplished a coordinated set of measurements of the Jovian dust streams inside and outside of Jupiter's magnetosphere.

The work in this thesis describes an emerging electrodynamical picture of the Jovian dust streams as they appear inside and outside of the Jupiter environment. The source of the Jovian dust streams is Jupiter's moon, Io, in particular, dust from Io's volcanoes. Charged Io dust, traveling on trajectories from Io's location, is shown in this work to have some particular signatures in real space and in frequency space.

The Jovian dust stream dynamics in the frequency-transformed Galileo dust measurements show different signatures, varying, orbit-to-orbit during Galileo's last 29 orbits around Jupiter. The varying frequencies from orbit-to-orbit are dependent on the spacecraft and dust detector geometry, on Jupiter's magnetosphere/plasma conditions, but also on Io itself, most likely its volcanoes' activity. The presence of

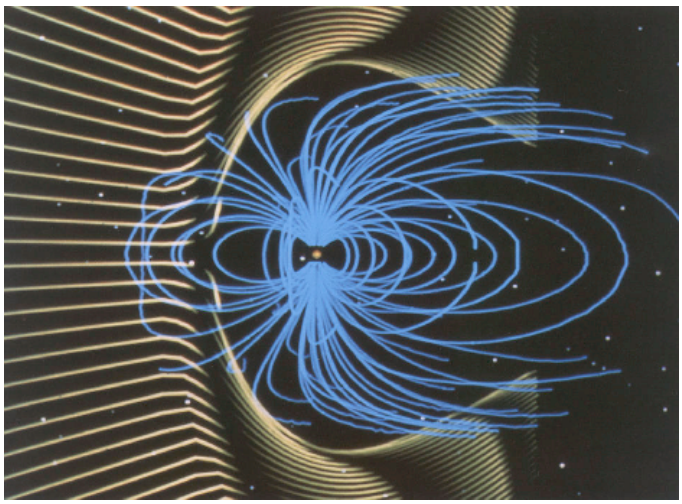

Figure 7.1 : Jupiter in the solar wind.

Io's orbital rotation frequency demonstrates that Io is a localized source of charged dust particles because charged dust from diffuse sources would couple to Jupiter's magnetic field and appear in frequency space with Jupiter's rotation frequency and its harmonics. A confirmation of Io's role as a localized charged dust source arises through the modulation effects. This time-frequency analysis is the first direct evidence that Io is the source of the Jovian dust streams. I provide additional frequency evidence of Io recorded by Cassini and Galileo during an August 2000 dust streams 'storm'.

One key to understanding the Jovian dust stream trajectories in real space is the dust particle's *variable* charging. If the dust particle is small enough (submicron-sized), then its trajectory is dominated by Lorentz forces. If the dust particle's charge varies during its travels, then its Lorentz-force-dominated dynamics vary, as well. The dust particle's charge varies via currents generated as the particle samples the plasma through which it travels.

Results from numerical charging experiments here show that the dust particle rarely reaches an equilibrium potential as it travels. The equilibrium charging times for the dust particles in Jupiter's magnetosphere are on the order of hours to days, therefore the dust particle accumulates more and more charges, which can dramatically influence its dynamical behavior. Numerical charging experiments here also

show that the secondary electron emission current, which was previously thought not to have an effect in the placid calm of the interplanetary solar wind, contributes at least +1 V potential to the particle's overall potential in the solar wind. Dynamical simulations of the dust stream particles using variable charging show several interesting effects: sensitivity of the particle's dynamics to the harmonic expansion of the magnetic field model, the velocities of variable charged particles increase over a much longer distance than fixed charge particles and the simulations show marked difference in dynamics with only slightly changing the particle size, the density, and the secondary electron emission current parameters. One effect studied is the size of ejected particles with different material properties. Here, smaller particles are ejected that have lower secondary electron emission energies/yields, and therefore the ejection of small sulfur particles are favored over the ejection of small silicate particles.

In order to meet the time-of-flight that the dust particles achieved during the December 2000 joint Galileo-Cassini dust stream measurements, the smallest dust particles could have the following range of parameters: size: 6 nanometers, density: 1.35–1.75 g/cm^3, initial charge potential: 1–4 V, secondary electron emission yield: 3.0, dependent on a maximum electron energy 300 eV, a photoelectron emission yield: 0.1–1.0, which produce dust particle speeds: 220\450 km s^{-1} (Galileo\Cassini) and charge potentials: 5.5\6.3 V (Galileo\Cassini).

Chapter 8

GOING FURTHER

In this chapter, I describe some paths for future work, in order to advance this Jovian dust streams research.

8.1 Time-Frequency Analysis of Ulysses Dust Detector Data

The Ulysses dust detector was the first instrument to detect the Jovian dust streams, however the last concentrated effort to work with this dataset for learning more about the Jovian dust streams was Zook et al.'s (1996) work. I wish to analyze the Ulysses data with some of the time-frequency tools that I developed in this thesis for the Galileo dust detector data. I expect to see the same 30-day periods seen by the previous investigators, plus I hope to see some patterns of frequency modulations and new periods, especially in the region closest to Jupiter.

8.2 Material Properties Parameters and the Particle's Trajectory

When simulating dust particle trajectories, a number of free and coupled parameters are involved. I can quantify the range, or error, on each of the parameters if I encapsulate the problem in a Bayesian framework. This section presents a rigorous mathematical approach to answering the question: "How does the range of material properties affect the particle's trajectory?" This mathematical approach gives the reliability of the estimates of the free parameters for a given dust particle trajectory.

The forces on the dust particle which determine its trajectory is the sum of the forces for planetary gravity, light pressure, Lorentz force and solar gravity. In the next diagram, I indicate which material properties are involved in that force calculation.

(The values in parentheses indicate that they are correlated.)

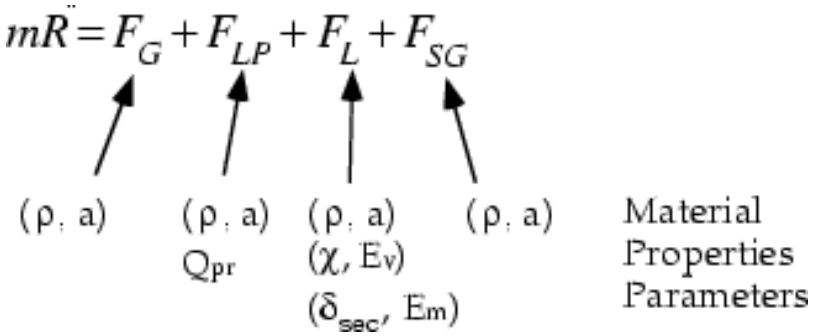

Figure 8.1 : Free and coupled parameters.

- (ρ, a) = particle density and radius.
- Q_{pr} = radiation pressure scattering coefficient, which is dependent on (ρ, a) via β, the ratio of radiation pressure force to solar gravitational force acting on the particle.
- (χ, E_ν) = photoelectric yield for the photoelectron emission current and the energy (usually Maxwellian) distribution of photoelectrons released from grain when a photon impacts onto the dust particle.
- $(\delta_{\rm sec}, E_m)$ = maximum yield of secondary electrons released at E_m by a high energy impacting electron or ion.

We want to find the probability distribution of our seven free parameters, given a computed trajectory $\vec{R}$, and given relationships between the parameters I:

$$\text{prob}\ (\rho, a, Q_{pr}, \chi, E_\nu, \delta_{\rm sec}, E_m, \mid \left\{\vec{R}\right\}, I)$$

The joint distribution of all conditions of the seven free parameters given by the dust trajectory data is proportional to the likelihood that the free parameters will produce the trajectory, times the degree of belief attributed to the parameters before the trajectory computation:

$$L \ = \ \log_{\rm e}[\text{prob}\ (\rho, a, Q_{pr}, \chi, E_\nu, \delta_m, E_m \mid \left\{\vec{R}\right\}, I)]$$

$$\propto \log_{\rm e}[prob\ (\left\{\vec{R}\right\}\ \mid \rho, a, Q_{pr}, \chi, E_\nu, \delta_m, E_m, I) \times \text{prob}\ (\rho, a, Q_{pr}, \chi, E_\nu, \delta_{\rm sec}, E_m \mid I)\ ]$$

$$L \ = \ \log_{\rm e}[\text{prob}\ (\rho, a, Q_{pr}, \chi, E_\nu, \delta_{\rm sec}, E_m \mid \left\{\vec{R}\right\}, I)]$$

Let $\{x_j\}$ = our free parameters. Then the best estimate of our free parameters is given by a solution to the simultaneous set of equations:

$$\frac{\partial}{\partial x_i} L|_{\{x_{0j}\}} = 0$$

The reliability of the estimate can be given by the "spread" of the above distribution by applying a Taylor expansion around the best estimate point, with the quadratic term most influencing the spread.

$$L = L(x_0) + \frac{1}{2}\sum_{i=1}^{7}\sum_{j=1}^{7} \frac{\partial^2 L}{\partial x_i \partial x_j}|_{x_0}(x_i - x_0)(x_j - x_0) + ...$$

Then the exponent of the L yields the approximation for the multidimensional probability distribution function describing the range of the seven free parameters.

$$prob\ (\{x_j\} \mid \left\{\vec{R}\right\}, I) \propto \exp\left[\frac{1}{2}(x_i - x_0)^T \nabla\nabla L(x_0)(x_i - x_0)\right]$$

where the double nabla $\nabla\nabla L$ is the symmetric 7x7 matrix of second partial derivatives of L and I show the transpose of the difference vector.

This is essentially a multidimensional least-squares fitting problem, where the reliability of the estimates of the free parameters falls out in a natural way.

If we wish to know the reliability of only one of the seven free parameters, then we would "marginalize" (in Bayesian terminology) by isolating one free parameter and integrating out the others. This would help us gain understanding for how one of the parameters influences the others in a dust particle trajectory calculation.

8.3 A More Appropriate Magnetic Field

This thesis follows trajectories of particles from the inner magnetosphere to the outside of the magnetosphere, and it was shown in this work, that the particle's trajectories are sensitive to the magnetic field model employed. Therefore, it is important to apply a suitable magnetic field model that is appropriate to Jupiter's magnetosphere as a whole.

I have, so far, treated the magnetic field as a *static* magnetic model. In order to continue treating the dust trajectories with a static magnetic field, two possibilities to improve the static model are:

1. Look to the Galileo magnetic field instrument data to compare measurements with the output of Connerney's models (O_4 and O_6), in order to determine which model is more accurate. Our Heidelberg dust group recently received some magnetic field data from the Galileo magnetometer team, therefore, we have the means to answer this question.

2. Supplement Connerney's models or implement another magnetic field model, which is more suitable to Jupiter's outer magnetic field. Connerney lists several possibilities in (Connerney 1981, pg. 7681) that would be more suitable to the outer magnetic field.

If one wishes to go further to simulate the dust particle trajectories, in as realistic a way as possible, then one should use real-time magnetic field data for all dust particle trajectories. The model then becomes a *dynamic* model.

BIBLIOGRAPHY

Bagenal, F. (1989), Torus-magnetosphere coupling, *in* M. Belton, R. A. West & J. Rahe, eds, 'Time-Variable phenomena in the Jovian system', SP-494.

Bagenal, F. (1992), 'Giant planet magnetospheres.', *Ann. Rev. Earth Sp. Sci.* **20**, 289–328.

Baguhl, M., Grün, E., Linkert, G., Linkert, D. & Siddique, N. (1993), 'Identification of "small" dust impacts in the Ulysses dust detector data', *Planet. Space Sci.* **41**(11/12), 1085–1093.

Beatty, J. K., Petersen, C. & Chaikin, A., eds (1999), *The New Solar System*, Sky Publishing.

Bretthorst, G. (1988), *Bayesian Spectrum Analysis and Parameter Estimation*, Springer-Verlag.

Burns, J. A., Hamilton, D. P. & Showalter, M. R. (2001), Dusty Rings and Circumplanetary Dust, *in* E. Grün, B. A. S. Gustafson, S. Dermott, H. Fechtig, eds, 'Interplanetary Dust', Springer Verlag, Heidelberg, Germany, pp. 275–332.

Burns, J. A., Lamy, P. L. & Soter, S. (1979), 'Radiation forces on small particles in the solar system', *Icarus* **40**, 1–48.

Chapman, S. & Ferraro., V. C. A. (1931), 'A new theory of magnetic storms , parts 1&2', *J. Geophys. Res.* **36**, 131.

Chow, V. W., Mendis, D. A. & Rosenberg, M. (1993), 'Role of grain size and particle velocity distribution in secondary electron emission in space plasmas', *J. Geophys. Res.* **98**, 19065–19076.

Connerney, J. E. P. (1981), 'The magnetic field of Jupiter: a generalized inverse approach.', *J. Geophys. Res.* **86**, 7679–7693.

Connerney, J. E. P. (1993), 'The magnetic fields of the outer planets', *J. Geophys. Res.* **98**, 18,659–18,679.

Connerney, J. E. P., Acuna, M. H. & Ness, N. F. (1981), 'Modeling the Jovian current sheet and inner magnetosphere', *J. Geophys. Res.* **86**, 8360–8384.

Cravens, T. E. (1997), *Physics of Solar System Plasmas*, Cambridge University Press.

Dessler, A. J. (1983), *Physics of the Jovian Magnetosphere*, Cambridge University Press.

Divine, N., Fechtig, H., Gombosi, T. I., S., H. M., Keller, H. U., Larson, S. M., Mendis, D. A., Newburn Jr., R. L., Reinhard, R., Sekanina, Z. & Yeomans, D. K. (1986), 'The comet Halley dust and gas environment', *SpSci Rev.* **43**, 1–104.

Draine, B. T. & Salpeter, E. E. (1979), 'On the physics of dust grains in hot gas', *Ap. J.* **231**, 77–94.

Evans, A. (1994), *The Dusty Universe*, John Wiley.

Feuerbacher, B., Willis, R. F. & Fitton, B. (1973), 'Electrostatic potential of interstellar grains', *Ap. J.* **181**, 101–114.

Goertz, C. (1989), 'Dusty plasmas in the solar system', *Rev Geophys.* **27**, 271–292.

Graps, A. L. (1995), 'An introduction to wavelets', *IEEE Computational Science and Engineering* **2**(2), 50–61.

Graps, A. L. & Grün, E. (2000), Properties, charging, and dynamics of interplanetary dust particles in Earth's magnetosphere, Technical report, European Space Agency.

Graps, A. L., Grün, E., Svedhem, H., Krüger, H., Horányi, M., Heck, A. & Lammers, S. (2000), 'Io as a source of the Jovian dust streams', *Nature* **405**, 48–50.

Grün, E., Morfill, G. E., Schwehm, G. & Johnson, T. V. (1980), 'A model of the origin of the Jovian ring', *Icarus* **44**, 326–338.

Grün, E., Fechtig, H., Hanner, M. S., Kissel, J., Lindblad, B., Linkert, D., Linkert, G., Morfill, G. E. & Zook, H. A. (1992), 'The Galileo dust detector', *Space Sci. Rev.* **60**, 317–340.

Grün, E., Fechtig, H., Giese, R. H., Kissel, J., Linkert, D., Maas, D., McDonnell, J. A. M., Morfill, G. E., Schwehm, G. & Zook, H. A. (1992), 'The Ulysses dust experiment', *Astron. Astrophys. Suppl. Ser.* **92**, 411–423.

Grün, E., Zook, H. A., Baguhl, M., Fechtig, H., Hanner, M. S., Kissel, J., Lindblad, B.-A., Linkert, D., Linkert, G., Mann, I., McDonnell, J. A. M., Morfill, G. E., Polanskey, C., Riemann, R., Schwehm, G. & Siddique, N. (1993*a*), 'Ulysses dust measurements near Jupiter', *Science* **257**, 1550–1552.

Grün, E., Zook, H. A., Baguhl, M., Balogh, A., Bame, S. J., Fechtig, H., Forsyth, R., Hanner, M. S., Horányi, M., Kissel, J., Lindblad, B.-A., Linkert, D., Linkert, G., Mann, I., McDonnell, J. A. M., Morfill, G. E., Phillips, J. L., Polanskey, C., Schwehm, G., Siddique, N., Staubach, P., Svestka, J. & Taylor, A. (1993*b*), 'Discovery of Jovian dust streams and interstellar grains by the Ulysses spacecraft', *Nature* **362**, 428–430.

Grün, E., Hamilton, D., Baguhl, M., Riemann, R., Horányi, M. & Polanskey, C. (1994), 'Dust streams from comet Shoemaker-Levy 9?', *Geophys. Res. Letters* **21**, 1035–1038.

Grün, E., Hamilton, D. P, Riemann, R., Dermott, S., Fechtig, H., Gustafson, B. A., Hanner, M. S., Heck, A., Horányi, M., Kissel, J., Krüger, H., Lindblad, B.-A., Linkert, D., Linkert, G., Mann, I., McDonnell, J. A. M., Morfill, G., Polanskey, C., Schwehm, G., Srama, R., & Zook, H. (1996*a*), 'Dust measurements during the initial Galileo Jupiter approach and Io encounter', *Science* **274**, 399–401.

Grün, E., Baguhl, M., Hamilton, D. P., Riemann, R., Zook, H. A., Dermott, S., Fechtig, H., Gustafson, B. A., Hanner, M. S., Horányi, M., Khurana, K. K., Kissel, J., Kivelson, M., Lindblad, B.-A., Linkert, D., Linkert, G., Mann, I., McDonnell, J. A. M., Morfill, G. E., Polanskey, C., Schwehm, G. & Srama, R. (1996*b*), 'Constraints from Galileo observations on the origin of the Jovian dust streams', *Nature* **381**, 395–398.

Grün, E., Krüger, H., Graps, A. L., Hamilton, D. P., Heck, A., Dermott, S., Fechtig, H., Zook, H. A., Gustafson, B. A., Hanner, M. S., Horányi, M., Kissel, J., Lindblad, B.-A., Linkert, D., Linkert, G., Mann, I., McDonnell, J. A. M., Morfill, G. E., Polanskey, C., Schwehm, G. & Srama, R. (1997), 'Dust measurements in the Jovian magnetosphere', *Geophys. Res. Letters* **24**, 2171–2174.

Gustafson, B. A. S. (1993), 'Physics of zodiacal dust', *Ann. Rev. Earth Sp. Sci.* **22**, 553–595.

Hamilton, D. P. (2000), personal communication.

Hamilton, D. P. & Burns, J. A. (1993), 'Ejection of dust from Jupiter's gossamer ring', *Nature* **364**, 695–699.

Heck, A. (1999), Modellierung and Analyse der von der Raumsonde Galileo im Jupitersystem vorgefundenen Mikrometeoroiden-Populationen, PhD thesis, Ruprecht-Karls-Universität Heidelberg.

Horányi, M., Houpis, H. L. F. & Mendis, D. A. (1988), 'Charged dust in the Earth's magnetosphere', *Ap. Space Sci.* **144**, 215–229.

Horányi, M. (1990), 'The spatial distribution of submicron-sized debris in the terrestrial magnetosphere', *Adv. Space Res.* **10**, 403–407.

Horányi, M., Morfill, G. E. & Grün, E. (1993*a*), 'The dusty ballerina skirt of Jupiter', *J. Geophys. Res.* **98**, 21,245–21,251.

Horányi, M., Morfill, G. E. & Grün, E. (1993*b*), 'Mechanism for the acceleration and ejection of dust grains from Jupiter's magnetosphere', *Nature* **363**, 144–146.

Horányi, M. (1996*a*), 'Charged dust dynamics in the solar system', *Ann. Rev. Astr. Ap.* **34**, 383–418.

Horányi, M. (1996*b*), Unusual dynamics of circumplanetary dust, *in* T. W. Rettig & J. M. Hahn, eds, 'Completing the Inventory of the Solar System', ASP Conference Series, Astronomical Society of the Pacific, pp. 129–136.

Horányi, M., Grün, E. & Heck, A. (1997), 'Modeling the Galileo dust measurements at Jupiter', *Geophys. Res. Letters* **24**, 2175–2178.

Horányi, M., Walch, B., Robertson, S. & Alexander, D. (1998), 'Electrostatic charging properties of Apollo 17 lunar dust', *J. Geophys. Res.* **103**, 8575–8580.

Johnson, T. V., Morfill, G. & Grün, E. (1980), 'Dust in Jupiter's magnetosphere - an Io source', *Geophys. Res. Letters* **7**, 305–308.

Juhász, A. & Horányi, M. (1997), 'Dynamics of charged space debris in the Earth's plasma environment', *J. Geophys. Res.* **102**, 7237–7246.

Juhász, A. & Horányi, M. (1999), 'Magnetospheric screening of cosmic dust', *J. Geophys. Res.* **104**, 12577–12583.

Kharkevich, A. A. (1960), *Spectra and Analysis*, Consultants Bureau.

Kimura, H. & Mann, I. (1998), 'The electric charging of interstellar dust in the solar system and consequences for its dynamics', *Ap. J.* **499**, 454–462.

Kivelson, M. G. & Russell, C. T. (1995), *Introduction to Space Physics*, Cambridge University Press.

Krivov, A. V., Krüger, H., Grün, E., Thiessenhusen, K.-U. & Hamilton, D. P. (2001), 'A tenuous dust ring of Jupiter formed by escaping ejecta from the Galilean satellites', *J. Geophys. Res.* p. submitted.

Krüger, H., Grün, E., Heck, A. & Lammers, S. (1999), 'Analysis of the sensor characteristics of the Galileo dust detector with collimated Jovian dust stream particles', *Planet. Sp. Sci.* **47**, 1015–1028.

Lide, D., ed. (1998), *CRC Handbook of Chemistry and Physics, 79th Edition, 1998-1999*, CRC Press.

Maravilla, D., Flammer, K. R. & Mendis, D. A. (1995), 'On the injection of fine dust from the Jovian magnetosphere', *Ap. J.* **438**, 968–974.

McEwen, A. S., Keszthelyi, L., Geissler, P., Simonelli, D. P., Carr, M. H., Johnson, T. V., Klaasen, K. P., Breneman, H. H., Jones, T. J., Kaufman, J. M., Magee, K. P., Senske, D. A., Belton, M. J. S. & Schubert, G. (1998), 'Active volcanism on Io as seen by Galileo SSI', *Icarus* **135**, 181–219.

McGrath, M. (1997), 'Io and the plasma torus', *Science* **278**, 237–238.

Meyer-Vernet, M. (1982), ''Flip-flop' of electric potential of dust grains in space', *Astr. Ap.* **105**, 98–106.

Morfill, G. E., Grün, E. & Johnson, T. V. (1980*a*), 'Dust in Jupiter's magnetosphere: Effect on magnetospheric electrons and ions', *Planet. Space Sci.* **28**, 1115–1123.

Morfill, G. E., Grün, E. & Johnson, T. V. (1980*b*), 'Dust in Jupiter's magnetosphere: physical processes', *Planet. Space Sci.* **28**, 1087–1100.

Morfill, G. E., Grün, E. & Johnson, T. V. (1980*c*), 'Dust in Jupiter's magnetosphere: Time variations', *Planet. Space Sci.* **28**, 1111–1114.

Naidu, P. S. (1996), *Modern Spectrum Analysis of Time Series*, CRC Press.

Press, W. H. & Rybicki, G. B. (1989), 'Fast algorithm for spectral analysis of unevenly sampled data', *Ap. J.* **338**, 277–280.

Russell, C., Khurana, K. K., Huddleston, D. E. & Kivelson, M. G. (1998), 'Localized reconnection in the near Jovian magnetotail', *Science* **280**, 1061–1064.

Russell, C. T. & Luhmann, J. G. (1997), Jupiter: Magnetic field and magnetosphere, pp. 372–373.

Russell, C. T., Yu, Z. J., Khurana, K. K. & Kivelson, M. G. (submitted), 'Magnetic field changes in the inner magnetosphere of Jupiter', *Adv. Space Res.* .

Scargle, J. D. (1982), 'Studies in astronomical time series II: Statistical aspects of spectral analysis of unevenly spaced data', *Ap. J.* **263**, 835–853.

Scott, B. (1994), An introduction to MHD. Unpublished at http://www.ipp.mpg.de/ bds/lectures/mhd-lecture.html.

Spencer, J. R. & Schneider, N. M. (1996), 'Io on the eve of the Galileo mission', *Ann. Rev. Earth Sp. Sci.* **24**, 125–190.

Spitzer, L. (1962), *Physics of Fully Ionised Gases*, Wiley Interscience.

Srama, R. & Grün, E. (1997), 'The dust sensor for CASSINI', *Adv. Sp. Res.* **20**, 1467–1470.

Stern, D. (1976), 'Representation of magnetic fields in space', *Rev. Geophys. Sp. Phys.* **14**, 199–214.

Sternglass, E. J. (1954), Sci. pap. 1772, Westinghouse Res. Lab.

Suszcynsky, D. M., Borovsky, J. & Goertz, C. K. (1993), 'Secondary-electron yields of solar system ices', *Ap. Space Sci.* **13**, (10)–183–(10)187.

Van Allen, J. & Bagenal, F. (1999), *Planetary magnetospheres and the interplanetary medium*, in Beatty et al. (1999), pp. 39–58.

Whipple, E. C. (1981), 'Potentials of surfaces in space', *Rep. Prog. Phys.* **44**, 1197–1250.

Yeates, C. M., Johnson, T. V., Colin, L., Fanale, F. P., Frank, L. & Hunten, D. M. (1985), Galileo: Exploration of Jupiter's system, Technical Report SP-479, NASA.

Zook, H. A., Grün, E., Hamilton, D. P., Linkert, G., Liou, J.-C., Forsyth, R. & Phillips, J. L. (1996), 'Solar wind magnetic field bending of Jovian dust trajectories', *Science* **274**, 1501–1503.

Appendix A

LOMB-SCARGLE PERIODOGRAM DERIVATION

In this appendix, I derive the Lomb-Scargle periodogram.

Here, I fill in the steps of the Lomb-Scargle periodogram derivation given in (Naidu 1996). We are looking looking for a harmonic component:

$$h(t) = a\cos(w(t-\tau)) + b\sin(w(t-\tau))$$

of frequency ω, where a, b and τ are constants. The a and b are determined by minimization, and τ is a delay parameter that enables us to select any origin of time, which is defined as:

$$\tau_j = \frac{1}{2\omega_j}\tan^{-1}\left[\frac{\sum\limits_i \sin 2\omega_j t}{\sum\limits_i \cos 2\omega_j t}\right]$$

To estimate a, b, we minimize the square difference of the above with respects to the unknowns (a, b):

$$M = \sum_{i=0}^{T-1}\{x(t_i) - a\cos(w(t-\tau)) - b\sin(w(t-\tau))\}^2$$

$$\frac{\partial M}{\partial a} = 0, \quad \frac{\partial M}{\partial b} = 0$$

After solving the normal equations for a, b, we find:

$$a = \frac{\sum\limits_{i=0}^{T-1} x(t_i)\cos(\omega(t_i-\tau))}{\sum\limits_{i=0}^{T-1}\cos^2(\omega(t_i-\tau))}$$

$$b = \frac{\sum\limits_{i=0}^{T-1} x(t_i)\sin(\omega(t_i-\tau))}{\sum\limits_{i=0}^{T-1}\sin^2(\omega(t_i-\tau))}$$

The power in the harmonic component at frequency ω is

$$P(\omega) = \sum_{i=0}^{T-1} h^2 x(t_i)$$

$$= \frac{1}{2} \sum_{i=0}^{T-1} (a^2 \cos^2(\omega(t-\tau)) + b^2 \sin^2(\omega(t-\tau)))$$

$$P(\omega) = \frac{\frac{1}{2}\left[\sum_{i=0}^{T-1} x(t_i)\cos(\omega(t_i-\tau))\right]^2}{\sum_{i=0}^{T-1} \cos^2(\omega(t_i-\tau))} + \frac{\frac{1}{2}\left[\sum_{i=0}^{T-1} x(t_i)\sin(\omega(t_i-\tau))\right]^2}{\sum_{i=0}^{T-1} \sin^2(\omega(t_i-\tau))}$$

The factor $\frac{1}{2}$ is included to account for the fact that power is equally distributed between positive and negative frequencies.

The straight-forward implementation of this algorithm requires about 100*t^2 operations. W. Press has implemented a faster version in (Press & Rybicki 1989).

The above form for power has a simple statistical behavior. This periodogram has the same exponential probability distribution as for even spacing. The amplitudes

$$a \approx b \approx \left(\frac{2}{N_0}\right)^{\frac{1}{2}}$$

for the relevant values of ω.

Appendix B

GALILEO DUST DETECTOR DATA, ORBIT-BY-ORBIT, FREQUENCY-TRANSFORMED

In this appendix, I display the Galileo dust detector data, orbit-by-orbit: In real-space of dust impact rates onto the detector (Note for some orbits: I applied a natural log to the rate data before calculating the periodogram to induce a less noisy periodogram result), and in frequency-space via periodograms. The middle plot for each orbit indicates the locations in space where the spacecraft received dust impacts.

Orbit G1, 1996: 80 -- 214

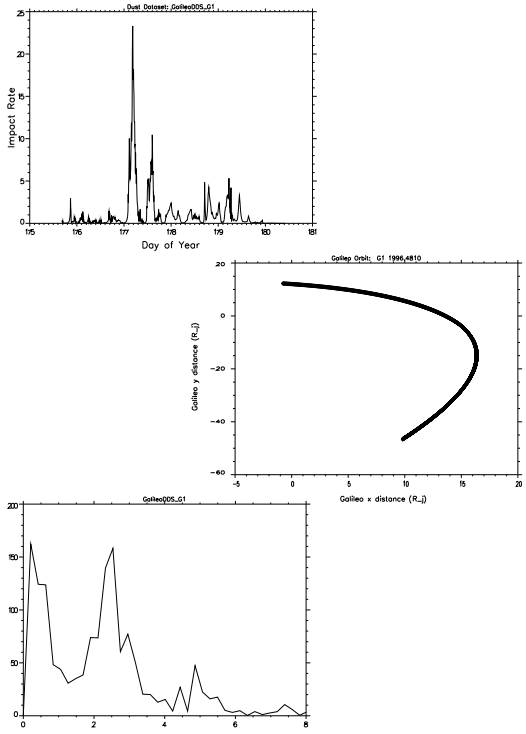

Orbit G2, 1996: 214 -- 281.6

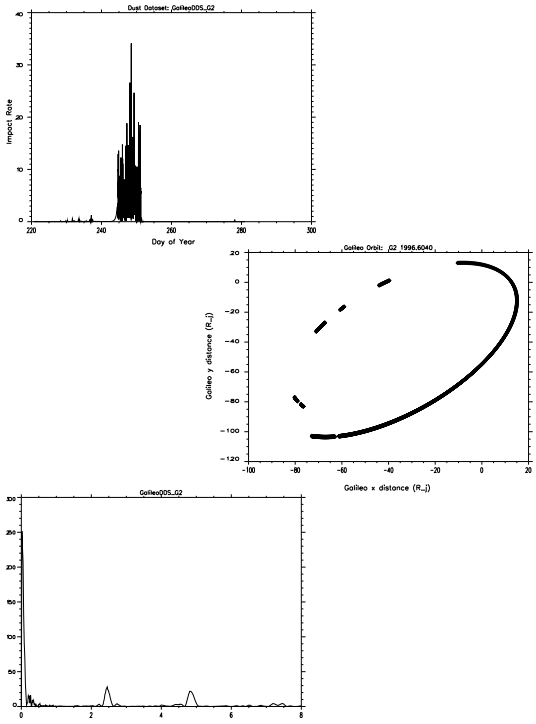

Orbit C3, 1996: 281.6 -- 332.9

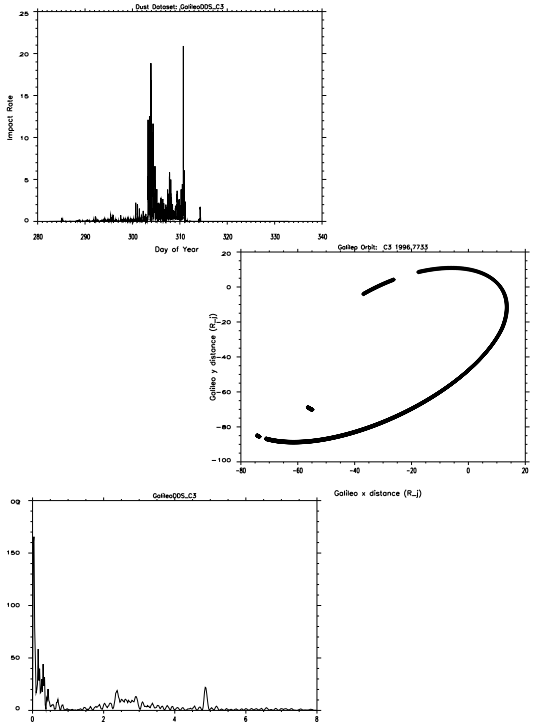

Orbit E4, 1996: 332.9 -- 1997:5.1

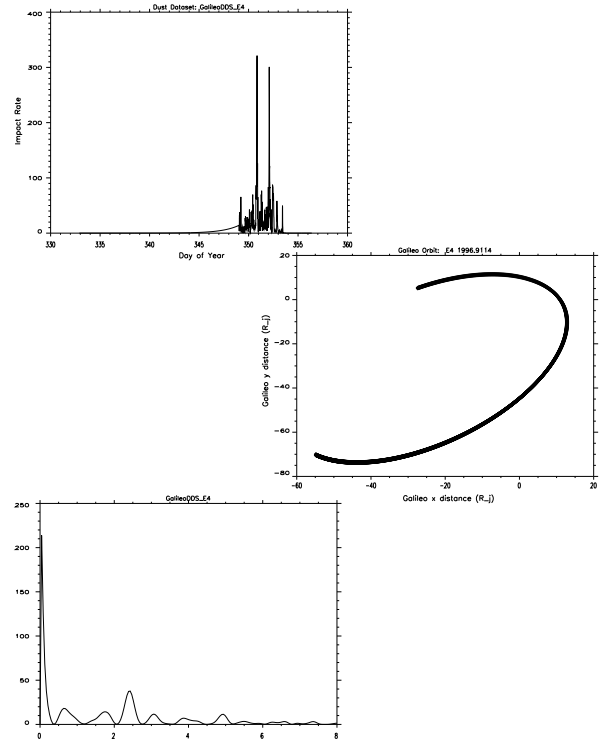

Orbit E6, 1997: 36.0 -- 73.2

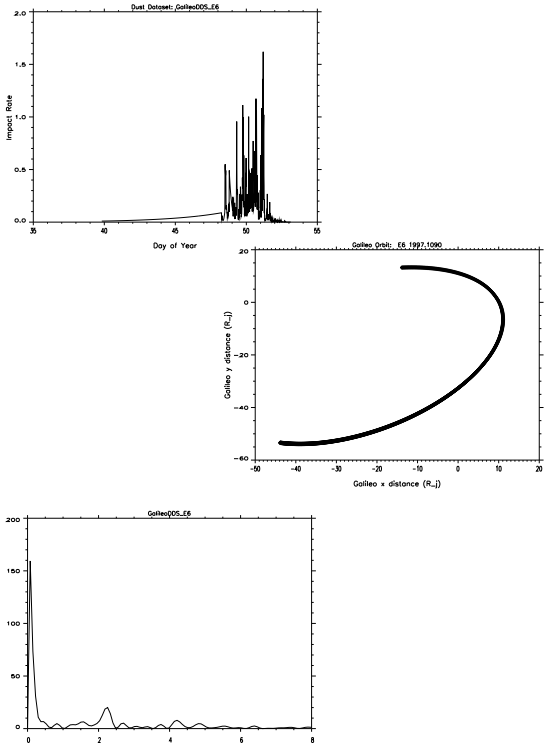

Orbit G7, 1997: 73.2 -- 111.5

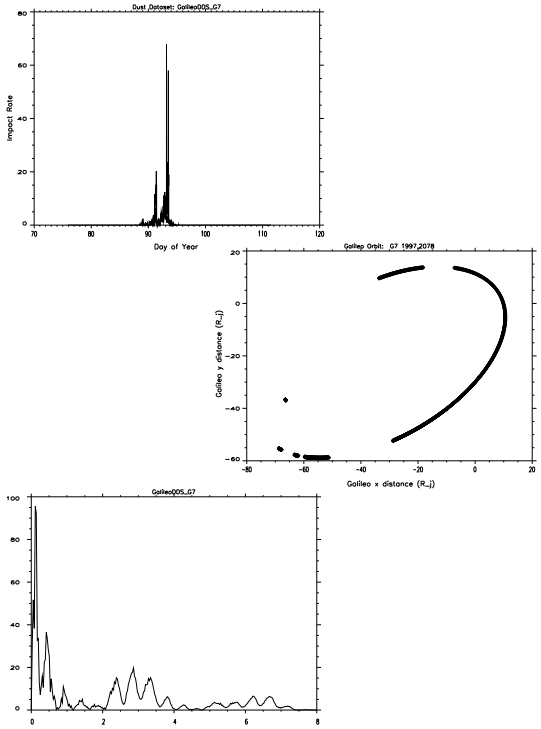

Orbit G8, 1997: 111.5 -- 153.5

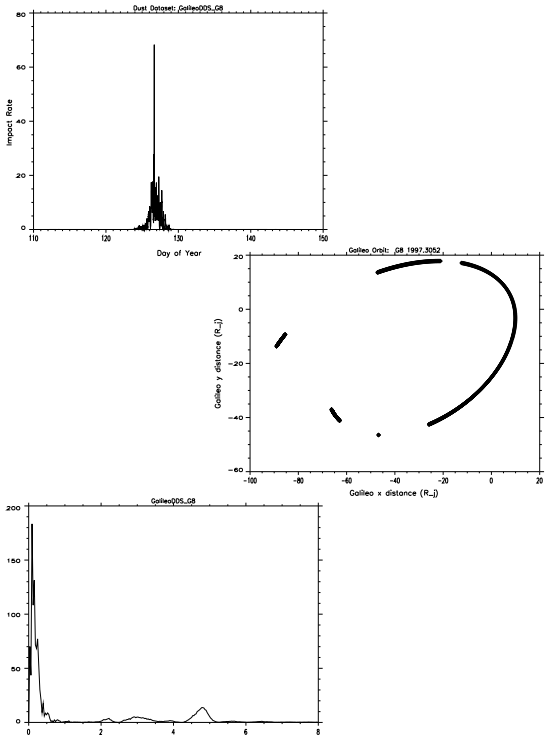

Orbit C9, 1997: 153.5 -- 220.2

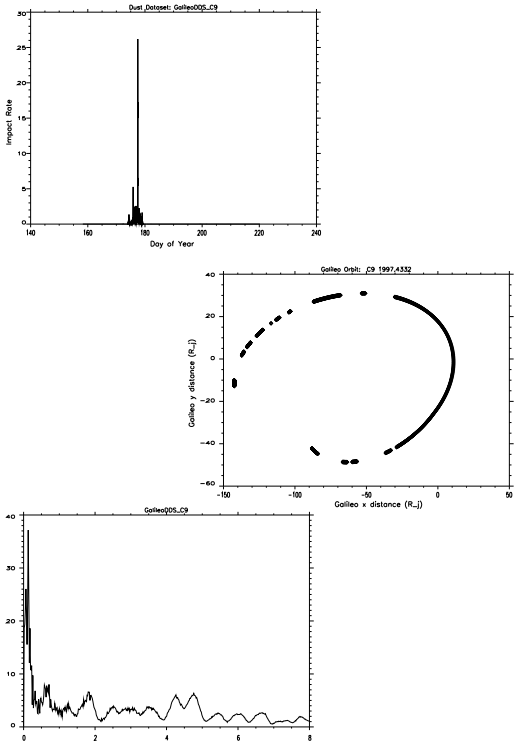

Orbit C10, 1997: 220.2 -- 286.5

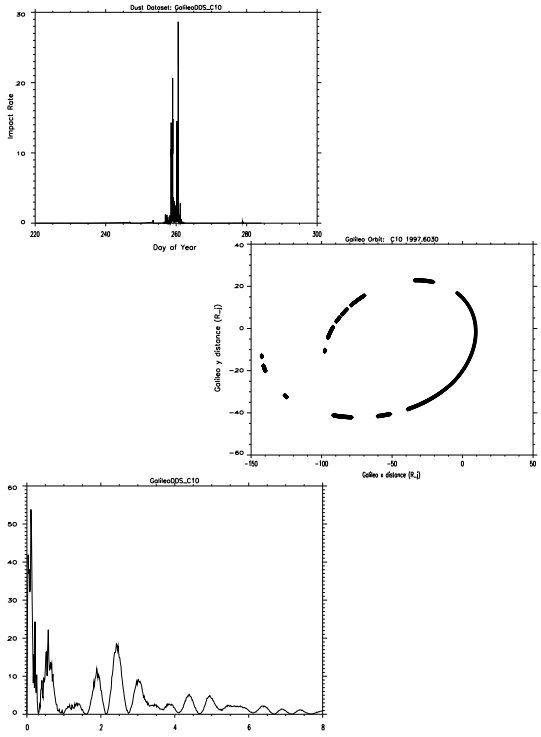

Orbit E11, 1997: 286.5 -- 336.0

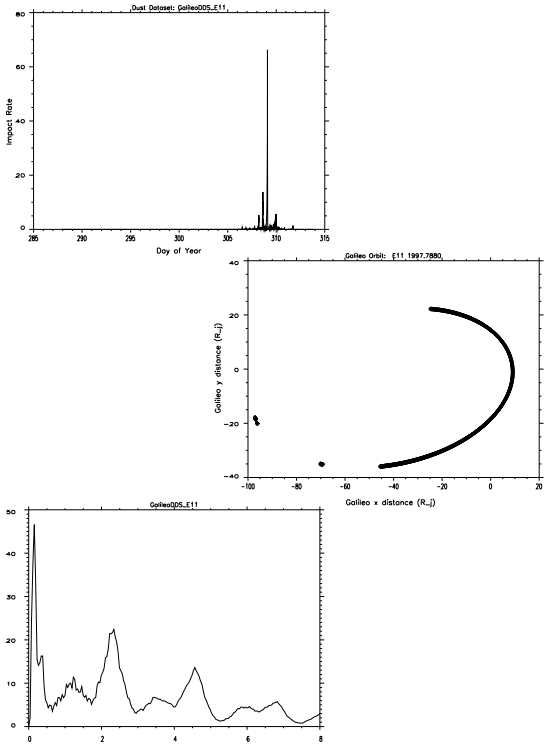

Orbit E14, 1998: 65.0 -- 1998:122.0

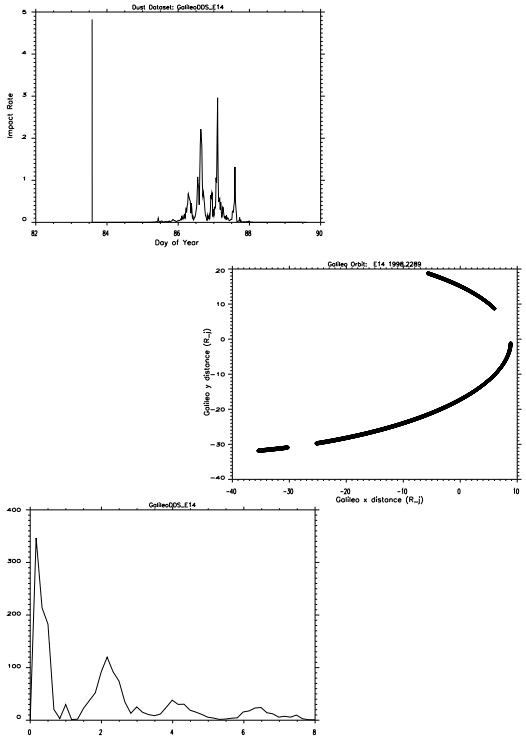

Orbit E15, 1998: 122.0 -- 178.0

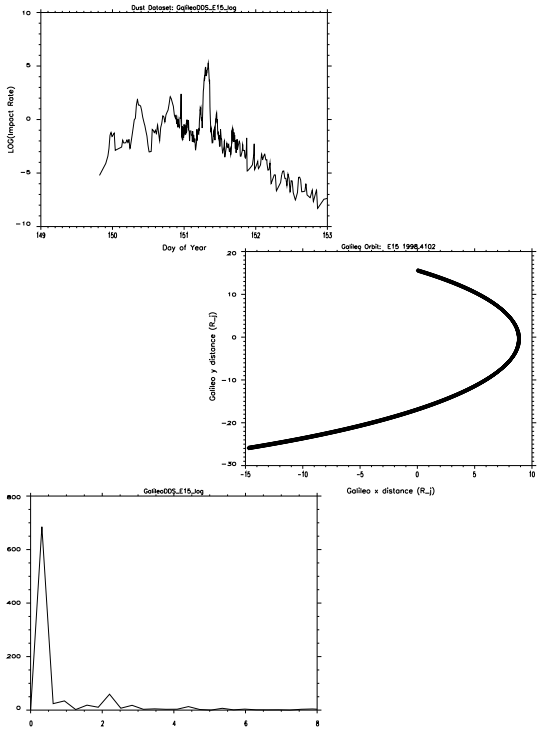

Orbit E16, 1998: 178.0 -- 236.0

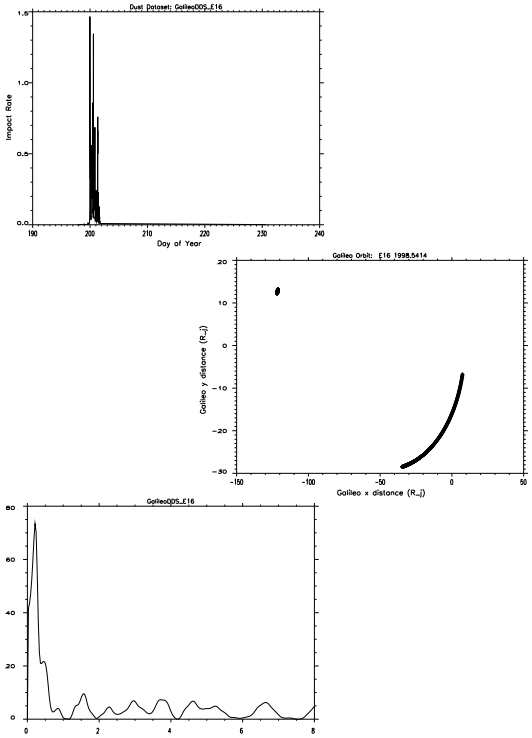

Orbit E17, 1998: 236.0 -- 299.0

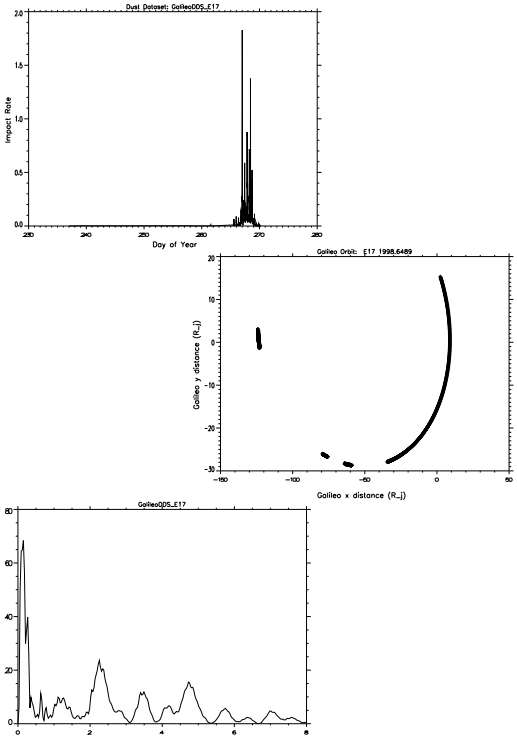

Orbit E18, 1998: 299.0 -- 1998:363.0

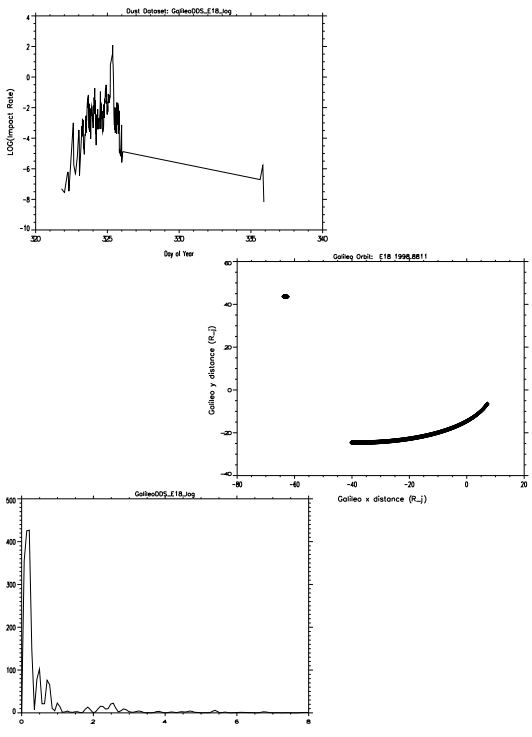

Orbit E19, 1998: 363.0 -- 1999:78.0

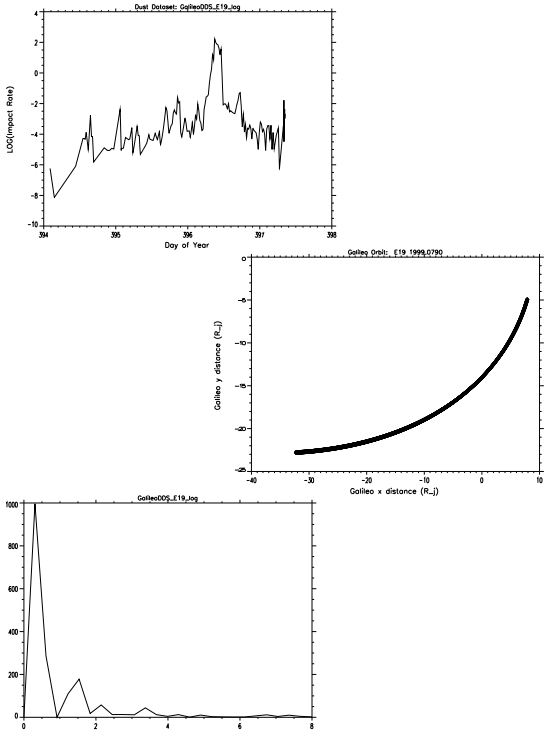

Orbit C20, 1999: 78.0 -- 155.0

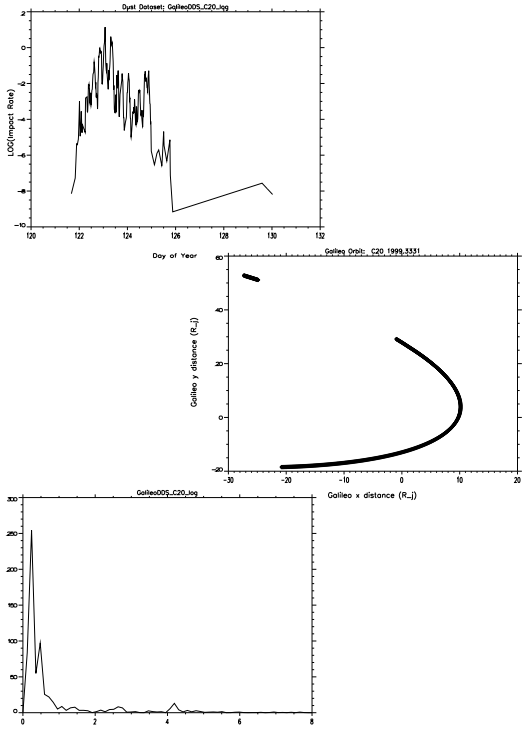

Orbit C21, 1999: 155.0 -- 204.0

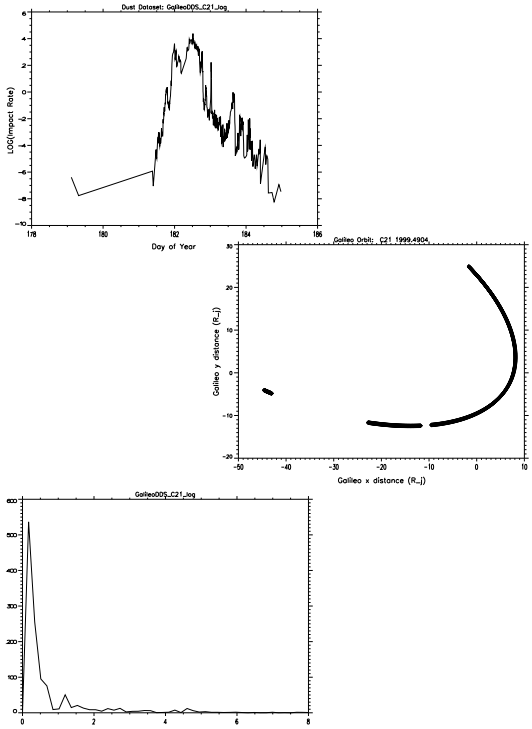

Orbit C22, 1999: 204.0 -- 242.0

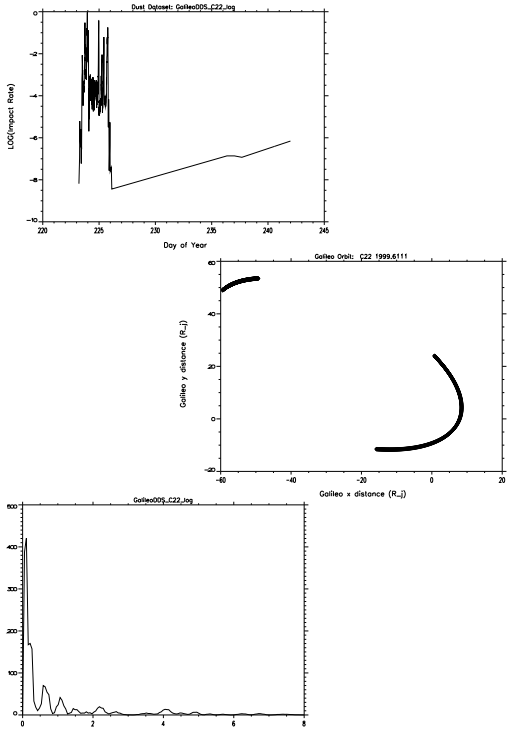

Orbit C23, 1999: 242.0 -- 271.0

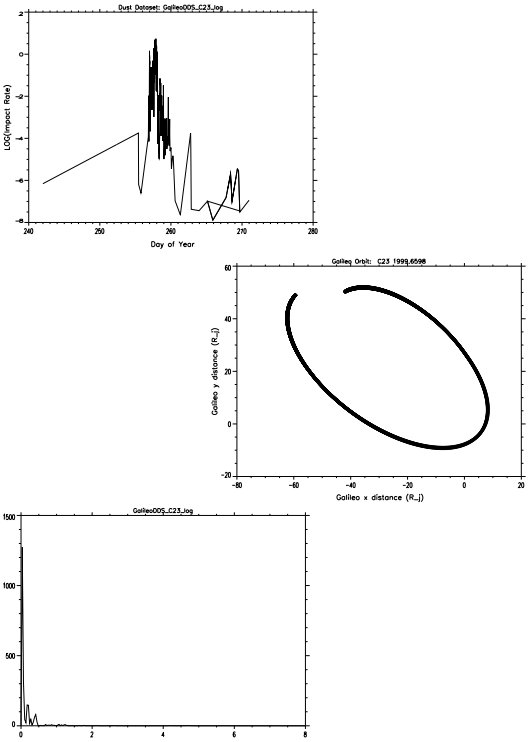

Orbit I24, 1999: 271.0 -- 307.0

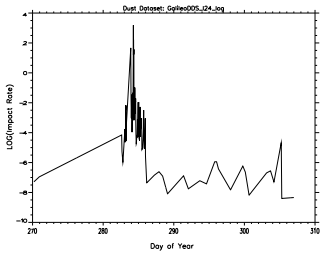

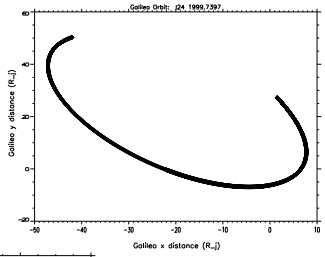

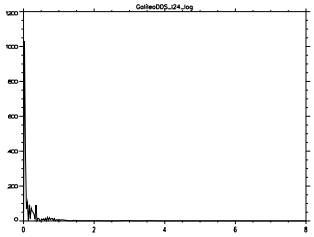

Orbit I25, 1999: 307.0 -- 341.1

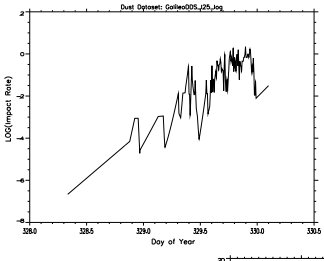

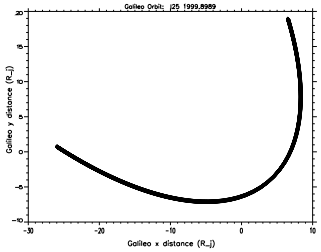

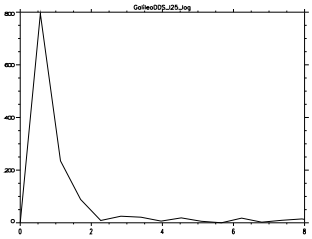

Orbit E26, 1999: 349.1 -- 2000: 4.1

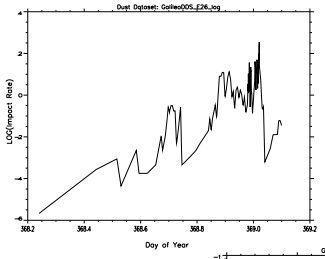

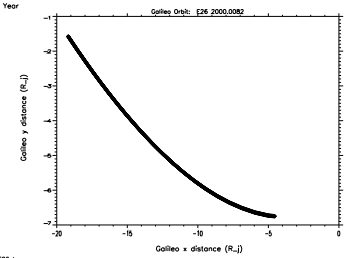

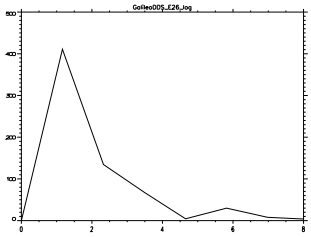

Orbit I27, 2000: 28.2 -- 53.5

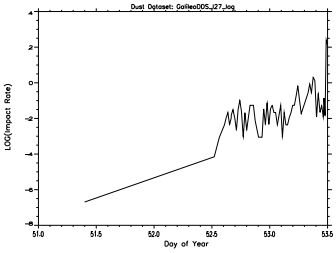

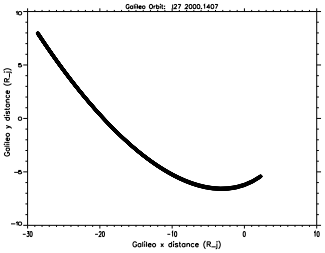

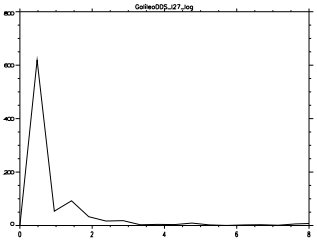

Orbit G28, 2000: 97.2 -- 142.2

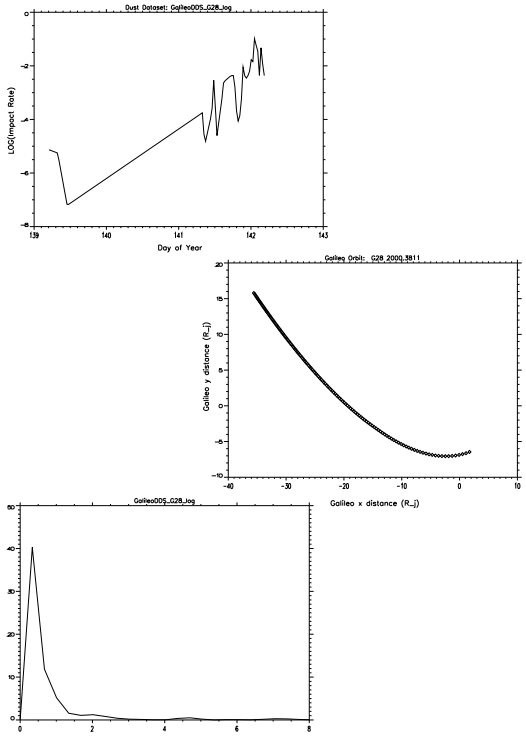

Orbit G29, 2000: 363.0 -- 2001: 71.6

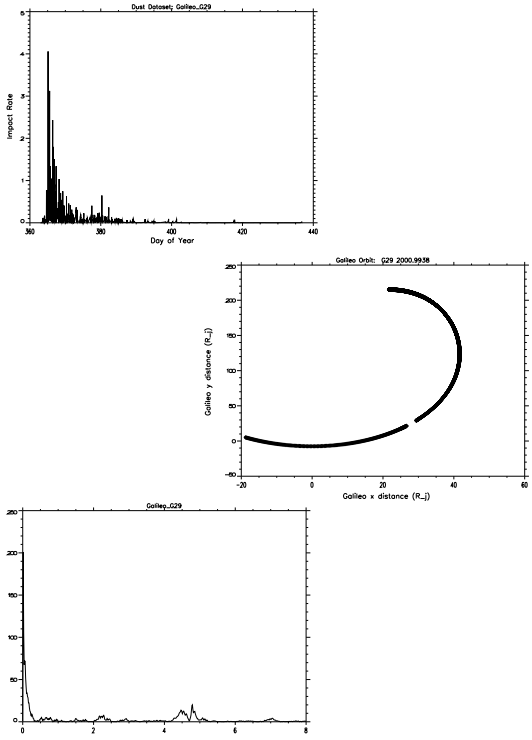

Appendix C

COROTATION

In this appendix, I provide the physical background for the concept of corotation in a planetary magnetosphere and I give the implicit assumptions involved in deriving a magnetosphere boundary, following the work of Cravens (1997), and R. A. Wolff in (Kivelson & Russell 1995).

C.1 Derivation of the Corotation Electric Field

Magnetospheric conditions are generally described by magnetohydrodynamics (MHD) with the assumption that the field is frozen into the flow (Bagenal 1992, pg. 296), therefore, the electric field doesn't appear explicitly. However, the plasma flow velocity and the electric field are related via the generalized Ohm's law, therefore, one can use MHD to derive the electric field in Jupiter's magnetosphere. Following Cravens' work (Cravens 1997, pgs. 390-392), I derive an expression for the electric field, which is necessary to know for the Lorentz force in the dynamics portion of this dissertation.

If we begin with a single-fluid MHD momentum equation:

$$\rho\frac{\partial u}{\partial t} + \rho\vec{u}\bullet\vec{\nabla}\vec{u} = -\vec{\nabla}p + \vec{J}\times\vec{B} + \rho\vec{g} - \rho\upsilon\left(\vec{u}-\vec{u}_n\right) - P_i m_i\left(\vec{u}-\vec{u}_n\right)$$

and neglect gravity and mass-loading, then the momentum equation becomes:

$$\rho\frac{D\vec{u}}{Dt} = -\vec{\nabla}p + \vec{J}\times\vec{B} - \rho\upsilon\left(\vec{u}-\vec{u}_n\right)$$

where the velocity $\vec{u}_n$ is the neutral plasma velocity in the friction term: $\rho\upsilon\left(\vec{u}-\vec{u}_n\right)$. For low flow speeds and steady-state conditions, the left-hand side is zero. We can also neglect the pressure gradient term, $\vec{\nabla}p$, because it is a minor effect (Cravens 1997, pg. 390). Therefore,

$$\vec{J}_\perp\times\vec{B} = \rho\upsilon\left(\vec{u}-\vec{u}_n\right)$$

where $\vec{J}_\perp$ is called the *Pederson current* in the ionosphere. This current must connect to the current in the magnetosphere. It may be helpful to think of plasma in the magnetosphere as coupled by means of the magnetic field lines to a giant flywheel (the planet) with the ionosphere acting as the clutch (Bagenal 1992, pg. 296).

If there is no stress on the plasma in the magnetosphere, then $\vec{J}_\perp \approx 0$, and the ionospheric plasma moves with the neutral gas:

$$\vec{J}_{\perp ion} \approx 0 \Rightarrow \vec{u} = \vec{u}_n$$

The electric field and the current density are related via the *Generalized Ohm's Law* for the ionosphere (Cravens 1997, pg. 306). Since $\vec{J}_\perp \approx 0$, then the electric field, $\vec{E}'$, which is in the frame-of-reference of the flowing neutral gas $\vec{u}_n$, is also ≈ 0.

$$\vec{E}' = \vec{E} + \vec{u}_n \times \vec{B} \approx 0$$

$$\vec{E} = -\vec{u}_n \times \vec{B}$$

For the magnetospheric plasma to rotate with the planet, the upper region of the neutral atmosphere must corotate with the planet, and must be closely coupled to the ionosphere by collisions (Bagenal 1992, pg. 296). Then:

$$\vec{u}_n = \vec{\Omega}_J \times \vec{r}$$

where Ω_J is the angular frequency of Jupiter, and the radial position vector is $\vec{r}$. Combining the above two expressions, we arrive at an expression of the corotation electric field:

$$\vec{E}_{\text{cor}} = -\left(\vec{\Omega}_J \times \vec{r}\right) \times \vec{B}$$

To check that the plasma in the magnetosphere corotates with Jupiter, start with the ideal MHD version of the generalized Ohm's Law: $\vec{E} = \vec{u} \times \vec{B}$. The plasma flow velocity perpendicular to $\vec{B}$ is:

$$\vec{u}_\perp = \frac{\vec{E} \times \vec{B}}{B^2}$$

$$\vec{u}_\perp = \frac{\vec{E}_{\text{cor}} \times \vec{B}}{B^2}$$

$$\vec{u}_\perp = -\frac{\left(\left(\vec{\Omega}_J \times \vec{r}\right) \times \vec{B}\right) \times \vec{B}}{B^2}$$

$$\vec{u}_\perp = \vec{\Omega}_J \times \vec{r}$$

showing that plasma in the magnetosphere corotates with Jupiter. An implicit assumption is that the plasma is a *cold* plasma; more energetic plasma particles also experience gradient and curvature drifts, therefore, more terms than $(\vec{E} \times \vec{B})$ are necessary for deriving the electric field.

C.2 Derivation of the Magnetosphere Boundary

At a small radial distance, the electric field is driven by corotation. Further away from the planet, the electric field is driven by the solar wind. The magnetosphere boundary between these two circulation motions can be calculated by balancing these two fields in order to find where the plasma flow velocity is zero. Starting with the convection electric field:

$$\vec{E}_{\rm cv} = -\eta v_{SW} \times \frac{\vec{B}_0}{R_m}$$

where η is the efficiency of the reconnection process in harnessing the solar wind momentum, and R_m is the magnetopause distance (Bagenal 1992, pg. 297). In the simplest magnetospheric models, $E_{\rm cv}$ is assumed constant throughout the magnetosphere, so then the corresponding plasma velocity is given by the $\vec{E} \times \vec{B}$ drift:

$$v_{\rm cv} = \eta\, v_{SW} \left(\frac{R}{R_m}\right)^3$$

Since $E_{\rm cv}$ is proportional to r^3, and $E_{\rm cor}$ is proportional to r^{-2}, then corotation must dominate close to the planet, and solar wind driven convection must dominate outside a critical distance (Bagenal 1992, pg. 298).

To relate the two fields, map the electric potential from the ionosphere out into the magnetosphere following the equipotential lines (see Fig. 8.27 in (Cravens 1997,

pg. 393)). To derive the magnetosphere boundary, sum the two equipotentials: the corotation potential and the magnetospheric convection potential:

$$\varphi = E_0 r \sin\theta - \frac{\Omega_J B_0 R_J^3}{r}$$

and set $\partial\varphi/\partial r = 0$, and $\partial\varphi/\partial\theta = 0$. Then the point where the flow velocity is zero is:

$$r_{zero}^2 = \frac{\Omega_J B_0 R_J^3}{E_0}$$

r_{zero} is our magnetosphere boundary.

Appendix D

FIELD EMISSION AND ELECTROSTATIC DISRUPTION

In this appendix, I provide numbers that may be useful for situations when the dust particle is highly-charged.

Charging on a particle is limited for cases of high negative and high positive dust charges. *Electron field emission* begins when a compact solid particle has an electric surface field strength (Graps & Grün 2000):

$$E_d = \frac{\phi_s}{a} = -10^9 \mathrm{V/m}$$

where ϕ_s is the particle's surface potential, and a is the particle's radius.

Ion field emission begins at about 10 times higher particle electric field strength values:

$$E_d = \frac{\phi_s}{a} = +2 \times 10^{10} \mathrm{V/m}$$

For noncompact particles, we need to consider the tensile strength of the material:

$$F_t = \frac{\varepsilon_0 \phi_s^2}{a^2} = 8.859 \times 10^{-8}\, \phi_s^2(\mathrm{V})/a^2(\mathrm{cm}) \quad (\mathrm{N/m^2})$$

Table D.1 : Typical tensile and corresponding field strengths.

Fluffy aggregates:	$10^3 N/\mathrm{m}^2 \quad (10^5 \mathrm{V/m})$
Icy materials:	$10^3 - 10^7 N/\mathrm{m}^2 \quad (10^5 - 10^7 \mathrm{V/m})$
Stony materials:	$10^6 - 10^8 N/\mathrm{m}^2 \quad (3 \times 10^6 - 3 \times 10^7 \mathrm{V/m})$
Glassy Materials:	$7 \times 10^8 N/\mathrm{m}^2 \quad (3 \times 10^7 \mathrm{V/m})$
Metals:	$2 \times 10^9 N/\mathrm{m}^2 \quad (1.5 \times 10^8 \mathrm{V/m})$

LIST OF FIGURES

2.1 Schematic of the Galileo dust detector 10
2.2 Ulysses measurements of the Jovian dust streams. 11
2.3 Galileo measurements of the Jovian dust streams in interplanetary space. 12
2.4 Sketch of one of Galileo's orbital trajectories. 13
2.5 Galileo fluxes for all 29 orbits. 15
2.6 Galileo measurements for the G17 flyby. 16
2.7 Dust impact rates from the Cassini-Galileo dual dust stream measurements performed on December 30, 2000. 16

3.1 Lomb-Scargle periodogram of some 1996-1997 Galileo rate data. . . . 22
3.2 Lomb-Scargle periodogram of 1998 Galileo rate data. 23
3.3 Lomb-Scargle periodogram of some 1999-2000 Galileo rate data. . . . 24
3.4 Lomb-Scargle periodogram of Galileo G28 rate data. 26
3.5 Lomb-Scargle periodogram of Cassini data from 2000: Days 248–274. 27
3.6 A continuous wavelet transform (CWT) of the Galileo dust impact rate data during 2000: Days 217–247. 28
3.7 Lomb-Scargle periodogram of Galileo 1996-1997 rate data, noting frequency signatures. 29
3.8 A synthetic dataset. 34
3.9 An FFT of the previous synthetic dataset. 35

4.1 A sketch of Jupiter's magnetosphere. 38
4.2 A sketch of the middle and outer Jovian magnetosphere. 42
4.3 Model plasma electron and ion temperatures. 47
4.4 Model plasma densities. 48
4.5 The coupling between the torus, magnetosphere and ionosphere. . . . 52
4.6 Ratio β for some cosmically significant materials. 55

5.1 Empirical method of calculating charging times. 66
5.2 Equilibrium potentials for a 10 nm-sized dust particle. 68
5.3 Charging currents for a 0.01 μm-sized dust particle from 5 to 20 R_J. . 69
5.4 Charging currents for a 0.01 μm-sized dust particle from 20 to 70 R_J. 70

6.1 Trajectories for Jovian dust stream particles of different sizes, with a fixed charge. 76
6.2 Trajectories for Jovian dust stream particles of different sizes, with a variable charge. 77
6.3 Trajectories of SiO_2 Jovian dust stream particles of different sizes. . . 79
6.4 Trajectories of SO_x Jovian dust stream particles of different sizes. . . 80
6.5 Lorentz force over the gravitational force for SiO_2 particles. 85
6.6 Lorentz force over the gravitational force for SO_x particles. 86
6.7 Forces calculated for a 4 nm-sized dust particle from 5 to 20 R_J. . . . 88
6.8 Forces calculated for a 4 nm-sized dust particle from 20 to 70 R_J. . . 89
6.9 Velocities vs. distance from Jupiter for particles with a fixed charge. . 90
6.10 Velocities vs. distance from Jupiter for SO_x different-sized particles with a variable charge. 91
6.11 Velocities vs. distance from Jupiter for SO_x 5, 8 nm sized particles with a variable charge. 92
6.12 Dust particle trajectories for a 6 nm-radius particle released at 6.2 R_J. 96
6.13 Dust particle trajectories for different sized particles released at 6.2 R_J. 97

7.1 Jupiter in the solar wind. 100

8.1 Free and coupled parameters. 104

LIST OF TABLES

Frequencies Related to Charged Dust 18
3.1 Time-evolution of Frequencies, Galileo Orbit-by-Orbit 21

4.1 Jupiter's Magnetic Field 39
4.2 Magnetic Field O_4 Model Gauss Coefficients 43
4.3 Magnetic Field O_6 Model Gauss Coefficients 44
4.4 Jupiter Plasma Representative Numbers 49
4.5 Dust Particle Sizes and Densities from Divine et al., 1986 53

5.1 Grain Material Secondary Electron Emission Parameters 63
5.2 Currents at Galileo's December 30, 2000 Location. 71
5.3 Currents at Cassini's December 30, 2000 Location 72

6.1 Sensitivity to Magnetic Field Expansion 87
6.2 Dust Material Explorations for the Cassini-Galileo Joint Measurements 95

D.1 Typical tensile and corresponding field strengths. 127

ACKNOWLEDGMENTS

This manuscript is dedicated to my father, Alexander Graps, whose boundless sense-of-life never fails to fill me with light, love, and laughter.

To my PhD committee: Prof. Drs. Dietrich Lemke, Franz Wegner, Bernd Jähne, and, especially, to Eberhard Grün, who is the primary reason that I moved 7000 miles, towing my faithful library behind me.

To my dust charging mentor, Mihály Horányi, whose valuable guidance is too high to estimate. To my colleagues/friends/teachers: Antal Juhász, Håkan Svedhem, Gerhard Drolshagen, Eduard Igenbergs, and Tony McDonnell, who each played an important part in my thesis learning process.

I am grateful for the warmth and wonderful support of other people, and I wish to acknowledge them here, as well. To the loving mothers in my life: Nina and Carolyn. To my special woman friends: Maureen, Brooke, Angelika, Dina, Angela, Natasha, Sibylle, and Tanya. To my caring friends across the sea and over the years: David, Wayne, Spike, Jesper, and Nick. To Marco and his inspiring photographs. To my worldwide network of engaging minds, the extropians.

And last, but certainly not least, to the Heidelberg Dust Group, which is, without a doubt, the nicest and most supportive work environment that I've ever had. Thank you.